Beam dynamics in a dispersionless ion storage ring

Masahiro Ikegami

Beam dynamics in a dispersionless ion storage ring

Masahiro Ikegami

A dissertation

Department of physics, Faculty of science,

Kyoto University

January 5, 2005

Abstract

A compact ion storage and cooler ring S-LSR has been designed with the circumference and radius of curvature of 22.557 m and 1.05 m, respectively and now under construction at ICR Kyoto University. One of the research subjects at S-LSR is laser cooling of a $^{24}Mg^{+}$ ion beam with the kinetic energy of 35 keV. Study of the dynamics of ion beams which is three-dimensionally cooled by a strong cooling force using rf cavities is the subject of the present thesis. The ultimate aim is the generation of a crystal beam which is extremely low emittance (low temperature) beam. The lattice structure of S-LSR is designed so as to be suitable for generation of a crystal beam. The main elements of S-LSR; namely, bending magnets and quadrupole magnets are designed by using a three-dimensional magnetic field calculation code TOSCA with high precision. In the design of the bending magnet, its pole shape has been carefully investigated in order to suppress the unwanted higher order components of the magnetic field. The adjustment of the effective length has also been tried. The real characteristics of the fabricated magnets have been investigated through the magnetic field measurements, which are reflected on the assignment of each magnet to the position in S-LSR at the magnet alignment.

In order to realize a high intensity three-dimensional crystal beam, it has been known that the effect of the bending shear due to the linear dispersion has to be avoided. For this purpose, a method which utilizes the deflection element superposing an electric field with the magnetic field has been proposed. This deflection element can eliminate the effect of the linear dispersion, and the electrostatic potential included in the deflector gives the ions necessary acceleration and deceleration for the stabilization of the 3D crystal structure. Thus the bending shear is expected to be moved away. Such dispersion-free deflection element is to be realized by inserting a cylindrical electrostatic deflector in the gap of the bending magnet. Due to severe size limitation to be installed in the magnet gap of 70 mm, the aspect ratio of the electrodes for the electrostatic deflector is not so good as 30/26 (gap/height), which has been managed with a special structure of the electrode having shims at both sides and intermediate electrodes. The effective length and the structure of the fringing field were designed, considering the consistency with the magnetic field obtained from the field measurement. Assuming the above mentioned dispersion-free deflection elements for the lattice of S-LSR, the beam dynamics becomes equivalent to the linear ion trap in which the crystallization of ions has already been observed. Although, in the case of S-LSR, the electric field realized by two coaxial cylindrical electrodes with the dependence of 1/r, does not make an operation point which satisfies so called "maintenance condition" of a crystal beam. The radially uniform electric field is found to give such an operation point as satisfies the "maintenance condition". Realization of the radially uniform electric field in the central region of the deflector is considered to be possible by the adjustment of the potentials of the intermediate electrodes of the present electrostatic deflector.

Contents

Chapter 1. Introduction

In recent years, considerable experimental effort has been devoted in various fields to realize a low temperature state of a multi-particle system. *Laser cooling* is one of the most powerful means for this purpose. It is often applied to charged particles confined in an ion trap where *Coulomb crystallization*, an ultimate low temperature state has already been achieved [1-1, 1-2, 1-3]. In the field of beam physics, other cooling techniques, such as *electron cooling* and *stochastic cooling*, have also been employed to control the rest-frame temperature of ion beams. By using the electron cooling technique, one-dimensional *ordering* of an ultra-low-density ion beam has been established at ESR and CRYRING [1-4, 1-5] (although it is physically different from a crystalline state [1-6]). The laser cooling experiment at PALLAS, a circular RFQ trap [1-7], has shown the observation of 2D and 3D crystalline beams at the very low beam energy around 1 eV. Furthermore, the realization of a bunched crystal beam has been reported [1-8]. However, the 3D crystallization of "fast ion beams" has not been accomplished in storage rings yet.

Noting the similarity between ion traps and storage rings, we naturally expect that Coulomb crystallization may be achievable even for a fast stored beam. Molecular dynamics (MD) studies have actually demonstrated the possibility of a phase transition to a *crystalline beam* [1-9, 1-10]. According to advanced MD simulations where the realistic lattice structure of a storage ring is incorporated, it has been shown that the crystal beam is not necessarily formed in any storage ring. It has been found that so-called maintenance conditions exist for realization of a crystal beam in a storage ring. First condition is that the beam energy must be below the transition energy; $\gamma < \gamma_t$. The second condition is $N > 2\sqrt{2}\nu_T$, where N is the number of the super period of the ring, and ν_T is the transverse tune [1-11]. In addition to the maintenance condition, a strong three-dimensional cooling force is also essential. Under the situation satisfying these maintenance conditions, MD simulation shows that a variety of crystalline configurations can be formed in a properly designed ring when a sufficiently strong three-dimensional (3D) cooling force is available [1-10, 1-11, 1-12, 1-13].

As the storage ring equipping strong laser cooling device, TSR (MPI in Germany) and ASTRID (Aarhus, in Denmark) exist. However, the storage ring that can operate under satisfying the second maintenance condition do not exist. The storage ring satisfying the maintenance condition, Crystal Storage Ring (CSR), is planned at LNL in Italy. Furthermore, a small laser-equipped storage ring (S-LSR) is now under construction at the ICR Kyoto University in collaboration with the National Institute of Radiological Sciences [1-14]. S-LSR has the super period 6 and, can operate under satisfying the maintenance conditions. Laser and electron cooling techniques are to be applied, at S-LSR, to ion beams that have relatively low kinetic energies. (Chapter. 2)

In actual storage ring, each element constructing the storage ring has a bit of structural error. Therefore, the number of the super period of actual storage rings is one, strictly. In order to realize the ideal number of super period, the construction error of each element has to be suppressed as far as possible. As explained later, the stop bands induced by structural error of the ring element may influence on the realization of the ultimate low temperature beam, thus they also should be suppressed. The bending magnets and quadrupole magnets for S-LSR were designed precisely by using a 3D magnetic field simulation code TOSCA. Then, the precise performance assessments by a field measurement were performed. And, optimum alignment to suppress the effect of each error has been considered. (Chapter. 3)

On the other hand, it has also been pointed out that the stability of a three-dimensional large particle

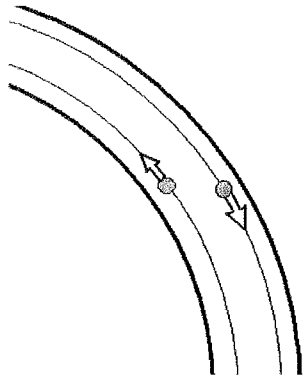

Fig. 1-1. The conceptual illustration of the shearing force. If all stored particles in a crystalline ground state have the same longitudinal velocity, the revolution frequency of a radially outer particle becomes longer than that of an inner particle. Consequently, the two particles are more and more distanced longitudinally every turn, which eventually leads to the melting of the crystalline state. The strength of the shearing force is closely related to the momentum dispersion, as shown in Section. 4.

number crystalline beam can be seriously affected by a dynamic effect peculiar to storage rings even if the maintenance conditions are satisfied. The most essential difference between ion traps and storage rings is whether the effect of *momentum dispersion* exists. In circular machines such as a synchrotron, or a storage ring, the closed orbit of a stored charged particle depends on its energy deviation from the design value. The existence of this dispersion inevitably yields dynamic coupling between the horizontal coordinate and longitudinal momentum of the particle, thus making the beam behavior more complicated compared with the ion trap. If the dispersive effect is negligible, then ion traps and storage rings become almost equivalent [1-15], which means that we encounter no substantial obstacle toward Coulomb crystallization. In general, however, strong momentum dispersion is inevitable as far as regular storage rings are concerned. This is one primary reason why the crystallization of fast stored beams is so difficult and has not been accomplished yet.

The cooling force provided by a usual cooling device is designed so as to equalize the longitudinal velocities of all stored ions, but such a force is not suitable for a 3D crystalline state with finite horizontal extent. When the 3D crystal beam enters into the bending section, the particles constructing outer and inner parts of the crystal structure are *sheared* due to the momentum dispersion, as illustrated in Fig. 1-1. Such effect is called as *shearing force*. In order to maintain the crystalline structure, stored particles must have an identical "angular" velocity rather than an identical "linear" velocity; in other words, we must compensate the difference in the revolution frequencies. As a solution of such a problem, *tapered cooling* has been proposed [1-12]. In tapered cooling, particles at different radial positions are cooled towards different velocities in order to realize the same "angular" momentum. However, no practical method to generate a tapered light has been known.

In this thesis, I propose an alternative scheme to stabilize 3D crystals; namely, a storage ring that has deflection elements using magnetic field and electric field simultaneously. The deflection elements using magnetic field and electric field simultaneously can suppress the dispersion. In this thesis such a deflection element is called as *dispersion-suppresser* or *dispersion-free deflector*.

As I prove later, the scalar potential of the dispersion-suppressor causes the longitudinal acceleration (or deceleration) of particles, automatically equalizing their angular velocities in the bending region. This means that, in a storage ring constructed by such deflectors, it is likely that 3D crystalline beams can be produced. The beam dynamics in such dispersion-free ring has interesting properties as proved in Chapter 4. The dispersion-suppressor described above is applied to S-LSR in order to demonstrate the practicability and potential of a dispersionless system. As a possible application of the dispersion-free operating mode of S-LSR, the laser cooling of a $^{24}Mg^{+}$ beam is planned. The storage ring, which is free-from shearing force, in addition to satisfying maintenance condition, is only the S-LSR in the world.

1.1 Single particle dynamics

The motion of a charged particle in accelerators is governed by Lorentz force [1-16]

$$\frac{d\vec{p}}{dt} = q(\vec{E} + \vec{v} \times \vec{B}) \tag{1-1}$$

where $\vec{p}$ is the mechanical momentum, q is the charge state of the particle. The electric field and magnetic field in accelerators is given by

$$\vec{E} = -\nabla\phi - \frac{\partial \vec{A}}{\partial t}, \qquad \vec{B} = \nabla \times \vec{A}, \tag{1-2}$$

In accelerator physics, it is useful to use a curvilinear coordinate system which has the design orbit of the synchrotron or beam line, as the reference orbit (Frenet-Serret coordinate system) (Fig 1-2). In the following, Hamiltonian formalism in the Frenet-Serret coordinate system is derived. We suppose that the coordinate of the reference orbit of the beam line is defined by $\vec{r}_0$. The tangent unit vector to the reference orbit is given by

$$\hat{\vec{s}} = \frac{1}{v_0(t)} \frac{d\vec{r}(t)}{dt} = \frac{d\vec{r}(s)}{ds}, \tag{1-3}$$

where $v_0(t)$ is the velocity of the reference particle, s is the length of reference orbit. And, the main normal vector (unit vector perpendicular to the tangential vector on the tangential plane) is given by

$$\hat{\vec{n}} = -\rho(t) \frac{1}{v_0(t)} \frac{d\hat{\vec{s}}(t)}{dt} = -\rho(s) \frac{d\hat{\vec{s}}(s)}{ds}, \tag{1-4}$$

where ρ is the radius of the curvature. The unit vector orthogonal to the tangential plane is given by

$$\hat{\vec{b}} = \hat{\vec{n}} \times \hat{\vec{s}}. \tag{1-5}$$

Then, as shown in Fig 1-2, we can express the coordinate of a discretionary particle passing the beam line by

$$\vec{r} = \vec{r}_0 + x\hat{\vec{n}} + y\hat{\vec{b}} \tag{1-6}$$

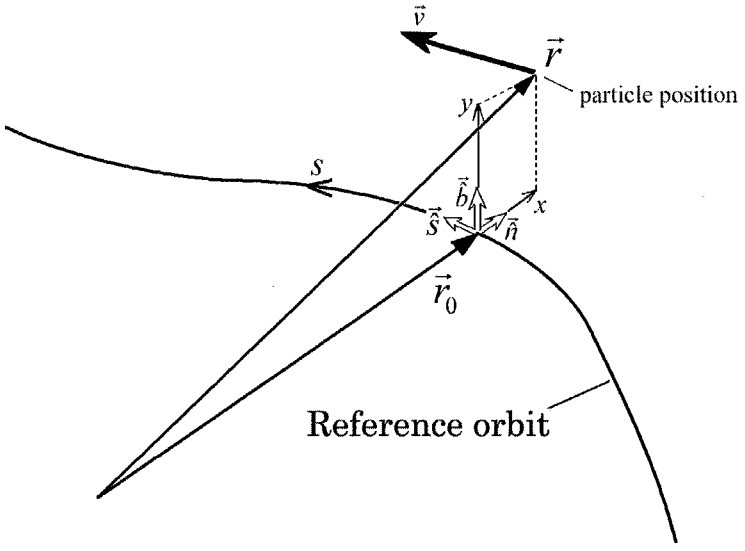

Fig.1-2. Curvilinear coordinate system for particle motion in beam line

From least action principle [1-17]

$$\delta\int\left(-mc^2\sqrt{1-(d\vec{r}/cdt)^2}+q\left[\vec{A}\cdot(d\vec{r}/dt)-\phi\right]\right)dt=0 \tag{1-7}$$

Here, we select the orbit length s, as the independent variable, instead of the time t. Then, Eq. (1-7) is rewritten to

$$\delta\int\left(-mc\sqrt{(cdt/ds)^2-(d\vec{r}/ds)^2}+q\left[\vec{A}\cdot(d\vec{r}/ds)-\phi(dt/ds)\right]\right)ds=0. \tag{1-8}$$

Therefore, the Lagrangian in this coordinate system becomes to

$$L=-mc\sqrt{(cdt/ds)^2-(d\vec{r}/ds)^2}+q\left[\vec{A}\cdot(d\vec{r}/ds)-\phi(dt/ds)\right] \tag{1-9}$$

In this case, t becomes one of the coordinates describing the particle motion.
Next, we rewrite this Lagrangian by the coordinates x, y, t. The differentiation of the basis $\vec{n}, \vec{b}, \vec{s}$ by s becomes as follows

$$\frac{d\vec{n}(s)}{ds}=\frac{1}{\rho(s)}\vec{s}(s)+\tau(s)\vec{b}(s),\quad \frac{d\vec{b}(s)}{ds}=-\tau(s)\vec{n}(s),\quad \frac{d\vec{s}(s)}{ds}=-\frac{1}{\rho(s)}\vec{n}(s), \tag{1-10}$$

where $\tau(s)$ is the torsion of the curve. When the relations (1-10) are used, the differentiation of the position Eq. (1-6) is expressed as

$$\frac{d\vec{r}}{ds}=\left(1+\frac{x}{\rho}\right)\vec{s}+\left(\frac{dx}{ds}-\tau y\right)\vec{n}+\left(\frac{dy}{ds}+\tau x\right)\vec{b} \tag{1-11}$$

Substituting this relation to Eq. (1-9), the Lagrangian in Frenet-Serret coordinate system is obtained.

$$\begin{aligned}L=&-mc\sqrt{(cdt/ds)^2-(1+x/\rho)^2-(dx/ds-y\tau)^2-(dy/ds+x\tau)^2}\\&+q\left[(1+x/\rho)A_s+(dx/ds-y\tau)A_x+(dy/ds+x\tau)A_y-\phi(dt/ds)\right]\end{aligned} \tag{1-12}$$

From Lagrangian (1-12), the canonical momenta are defined

$$p_x=\frac{\partial L}{\partial x'},\quad p_y=\frac{\partial L}{\partial y'},\quad p_t=\frac{\partial L}{\partial t'} \tag{1-13}$$

where x' means differentiation with respect to s. The Hamiltonian can be derived, from this Lagrangian, as

$$\begin{aligned}H&=x'p_x+y'p_y+t'p_t-L\\&=-(1+x/\rho)\sqrt{(p_t+q\phi)^2/c^2-m^2c^2-(p_x-qA_x)^2-(p_y-qA_y)^2}+q(1+x/\rho)A_s-(xp_y-yp_x)\tau\end{aligned} \tag{1-14}$$

The charged particle motion is governed by canonical equations derived from the Hamiltonian (1-14).

$$\begin{aligned}&\frac{\partial x}{\partial s}=\frac{\partial H}{\partial p_x},\quad \frac{\partial p_x}{\partial s}=-\frac{\partial H}{\partial x}\\&\frac{\partial y}{\partial s}=\frac{\partial H}{\partial p_y},\quad \frac{\partial p_y}{\partial s}=-\frac{\partial H}{\partial y}\\&\frac{\partial t}{\partial s}=\frac{\partial H}{\partial p_t},\quad \frac{\partial p_t}{\partial s}=-\frac{\partial H}{\partial t}\end{aligned} \tag{1-15}$$

Usual beam line of accelerators is designed in the horizontal plane. Therefore, $\tau(s)$ is usually zero.

1.2 Major elements of a storage ring

1.2.1 Bending magnet

In this section, a charged particle motion in a flat pole bending magnet is shown. Such a bending magnet is used for *separated-function* lattice storage ring as S-LSR. As shown in section 3, the magnetic field in such bending magnet is uniform. The reference particle is bent with the constant bending radius ρ_0 in the bending magnet. Therefore, the reference orbit is a circle with the radius of ρ_0, and the vector potential of the bending magnet is given by

$$(0,\,0,\,A_s)=\left(0,\,0,\,-\frac{B_y}{2}(\rho_0+x)\right), \tag{1-16}$$

where B_y denotes the strength of the magnetic field in the banding magnet. The relation between the bending radius and the magnetic field is given by

$$p_0 = qB_y\rho_0 \tag{1-17}$$

When the vector potential is substituted to the Hamiltonian, it becomes to

$$H=-(1+x/\rho)\sqrt{p_t^2/c^2-m^2c^2-p_x^2-p_y^2}+q(1+x/\rho)A_s \tag{1-18}$$

Substituting this Hamiltonian to the canonical equation, the equation of motion of the charged particle is obtained. However, it is difficult to solve this equation directly. So, we usually use an approximated form of Hamiltonian [1-18].

$$H\approx-\left(1+\frac{x}{\rho_0}\right)\left(qA_s+p-\frac{p_x^2+p_y^2}{2p}\right) \tag{1-19}$$

where p is the total kinetic momentum written as

$$p=m\beta\gamma c=\sqrt{p_t^2/c^2-m^2c^2}\,, \tag{1-20}$$

(β and γ are Lorentz factor). We have supposed that the transverse momentum p_x, p_y is much small compared with the total kinetic momentum and the position deviation from the reference orbit x is far small compared with the bending radius ρ_0. Therefore, higher order term of $p_{x(y)}/p$ and x/ρ_0 are neglected. This approximation is usually good approximation for actual accelerators. The momentum deviation from the design value $p_0=m\beta_0\gamma_0 c=\sqrt{E_0^2/c^2-m^2c^2}$ can be approximately given by

$$\Delta p=p-p_0\approx\frac{\Delta E}{\beta_0 c}-\frac{1}{2p_0}\left(\frac{\Delta E}{\beta_0 c\gamma_0}\right)^2 \tag{1-21}$$

where β_0 and γ_0 are Lorentz factor of the reference particle, and ΔE is the energy difference from the reference particle defined by $\Delta E\equiv(-p_t)-m\gamma_0 c^2$ (from Eq. 1-13, we can find that the $-p_t$ stands for the energy of the particle.) Substitution of Eq. (1-21) together with Eq. (1-17) into Eq. (1-19) yields the approximate normalized Hamiltonian

$$\tilde{H}=\frac{H}{p_0}\approx-\frac{\Delta E}{\beta_0^2E_0}+\frac{1}{2\gamma_0^2}\left(\frac{\Delta E}{\beta_0^2E_0}\right)^2+\frac{p_x^2+p_y^2}{2p_0^2}+\frac{x^2}{2\rho_0^2}-\frac{\Delta E}{\beta_0^2E_0}\frac{x}{\rho_0} \tag{1-22}$$

From this Hamiltonian, we obtain the horizontal equation of motion in the bending region

$$\frac{d^2x}{ds^2} \approx -\frac{x}{\rho_0^2} + \frac{1}{\rho_0}\frac{\Delta E}{\beta_0^2 E_0}. \tag{1-23}$$

When the energy deviation ΔE from the reference particle is small, in Eq. (1-21), the second order term of ΔE can be neglected and the following relation is obtained.

$$\Delta p \approx \frac{\Delta E}{\beta_0 c} \tag{1-24}$$

Then Eq. (1-23) becomes to

$$\frac{d^2x}{ds^2} \approx -\frac{x}{\rho_0^2} + \frac{1}{\rho_0}\frac{\Delta p}{p_0}. \tag{1-25}$$

The second term of the right hand side induces the orbit deviation due to the difference of the momentum. This effect called as *momentum dispersion* or *dispersion*. The effect of the dispersion to the beam dynamics is one of the most important themes in this thesis.

1.2.2 Quadrupole magnet

A charged particle motion in a quadrupole magnet is described from the Hamiltonian by the similar way. The quadrupole magnet has a function focusing a beam, but does not have bending effect. Thus, the reference orbit in the quadrupole magnet becomes the straight line passing through the center of the quadrupole. The vector potential of the quadrupole magnet is given by

$$(0, 0, A_s) = \left(0, 0, \frac{B_1}{2}(x^2 - y^2)\right) \tag{1-26}$$

where B_1 is the field gradient of the quadrupole magnet. By the same way with the previous section, the approximated normalized Hamiltonian is obtained.

$$\tilde{H} = \frac{H}{p_0} \approx -\frac{\Delta E}{\beta_0^2 E_0} + \frac{1}{2\gamma_0^2}\left(\frac{\Delta E}{\beta_0^2 E_0}\right)^2 + \frac{p_x^2 + p_y^2}{2p_0^2} - \frac{qB_1}{2p_0}(x^2 - y^2) \tag{1-27}$$

The equations of motion are

$$\frac{d^2x}{ds^2} \approx \frac{qB_1}{p_0} \cdot x \qquad \frac{d^2x}{ds^2} \approx -\frac{qB_1}{p_0} \cdot y. \tag{1-28}$$

1.3 Storage ring

A separated function type storage ring is constructed with bending magnets and quadrupole magnets. In addition to these elements, in usual case, an rf cavity is introduced for the purpose of beam bunching. Then, the vector potential of the whole ring can be described as

$$A_s = -\frac{B_y}{2}(\rho_0 + x) + \frac{1}{2}B_1(x^2 - y^2) + \delta_p(s)\frac{V_{RF}}{\omega}\cos(\omega t + \phi_0) \tag{1-29}$$

where B_y and B_1 is the function of position s, B_y is constant in the bending section and B_y=0 in the straight section, B_1 is constant in the quadrupole magnet and B_1=0 in the other region, ρ_0 is the bending radius of

the bending section. The vector potential is periodic function with the period of the storage ring. The last term of the right hand side means the vector potential of the rf cavity. By the same way with the previous section, the Hamiltonian of the storage ring is obtained

$$\tilde{H} = -\frac{\Delta E}{\beta_0^2 E_0}\frac{x}{\rho} - \frac{\Delta E}{\beta_0^2 E_0} + \frac{1}{2\gamma_0^2}\left(\frac{\Delta E}{\beta_0^2 E_0}\right)^2 + \frac{\tilde{p}_x^2 + \tilde{p}_y^2}{2} + \frac{1}{2}\left(K_x x^2 + K_y y^2\right) - \delta_p(s)\frac{qV_{RF}}{p_0\omega}\cos(\omega t + \phi_0) \qquad (1\text{-}30)$$

where

$$K_x = \frac{1}{\rho^2} - \frac{qB_1}{p_0}, \qquad K_y = \frac{qK_1}{p_0}.$$

ρ becomes to the function of s; $\rho = \rho_0$, in the bending region, and $\rho = \infty$ in the other region.
The periodic delta function in the last term of the right hand side can be written as [1-19]

$$\delta_p(s)\cos(\omega t + \phi_0) \approx \frac{1}{C}\cos(\omega t - \frac{2\pi hs}{C} + \phi_0) \qquad (1\text{-}31)$$

where C is the length of reference orbit in the ring. Here, we introduce a relative time $\Delta t = t - s/\beta_0 c$. This quantity means the deviation of the circulation time of the particle from the reference particle. Since the bunching rf cavity is synchronized to the beam circulation, the relation $\beta_0 c = \omega_0 C/2\pi$ stands up. When this relation is used, the phase of Eq. (1-31) can be expressed as

$$\omega t - \frac{2\pi hs}{C} + \phi_0 = \omega\Delta t + \phi_0 \qquad (1\text{-}32)$$

When the initial phase of the rf cavity is chosen to zero in order to maximize the bunching effect, the last term of Eq. (1-30) becomes to

$$\delta_p(s)\frac{qV_{rf}}{p_0\omega}\cos(\omega t + \phi_0) \approx \frac{qV_{rf}}{Cp_0\omega}\cos\omega\Delta t \qquad (1\text{-}33)$$

For a particle near the bottom of the rf bucket ($\omega\Delta t << 1$) the cosine of the Eq. (1-33) can be expanded. When the relative time is introduced and the cosine of the Eq. (1-33) is expanded, Hamiltonian (1-30) becomes to

$$\tilde{H} = \frac{\tilde{p}_x^2}{2} + \frac{1}{2}K_x x^2 + \frac{\tilde{p}_y^2}{2} + \frac{1}{2}K_y y^2 + \frac{1}{2\gamma_0^2}\left(\frac{\Delta E}{\beta_0^2 E_0}\right)^2 + \frac{qV_{rf}}{Cp_0\omega}\psi^2 - \frac{\Delta E}{\beta_0^2 E_0}\frac{x}{\rho} \qquad (1\text{-}34)$$

where ψ is the phase of the synchrotron motion, and constant terms are neglected. If we put

$$\tilde{p}_\psi = \frac{1}{\gamma_0}\frac{\Delta E}{\beta_0^2 E_0}, \qquad K_s = \frac{2qV_{rf}}{Cp_0\omega} \qquad (1\text{-}35)$$

Hamiltonian (1-34) becomes to

$$\tilde{H} = \frac{\tilde{p}_x^2}{2} + \frac{1}{2}K_x x^2 + \frac{\tilde{p}_y^2}{2} + \frac{1}{2}K_y y^2 + \frac{\tilde{p}_\psi^2}{2} + \frac{1}{2}K_s\psi^2 - \frac{\gamma_0}{\rho}\tilde{p}_\psi \cdot x \qquad (1\text{-}36)$$

Therefore, the Hamiltonian of a charged particle motion in a storage ring is almost equivalent to the Hamiltonian of three harmonic oscillators, except for the last term. The last term is called *shear* [1-10] or *shear term*. For a hot beam, this term causes the effect of the linear dispersion (see section 1.2.1). The influence of this term to crystal beams is discussed in detail, later.

1.4 3D Laser cooling of a fast ion beam

1.4.1 Laser cooling of a fast ion beam

Laser cooling is a method to cool a mass of atoms and ions confined in a finite system. In the laser cooling, the momentum change of the particles induced by the absorption or emission of photons are utilized. A beam circulating in a storage ring is a group of ions confined in a finite system. Now, we pay attention to the state of an ion in the laser cooled beam. When the ion encounters a laser photon which has energy corresponding to the excitation level of the ion, resonance absorption of the photon occurs. Then, the ion gains a momentum which has been brought by the laser photon (Fig. 1-3-(b)). Later, the spontaneous emission of a photon occurs for the ion, and then the momentum of the ion changed by the emitted photon (Fig. 1-3-(c)). The direction of the momentum of the spontaneously emitted photon is random and canceled out statistically, by contrast with the absorbed momentum being same direction. During the cooling, the ion repeats this cycle. After N cycle, the momentum of the ion becomes to

$$\vec{p} = \vec{p}_0 + N\vec{p}_a + \sum_{n=1}^{N} \vec{p}_{En} \tag{1-37}$$

Since the direction of the emitted photon is random, the last term of the right hand side becomes to zero.

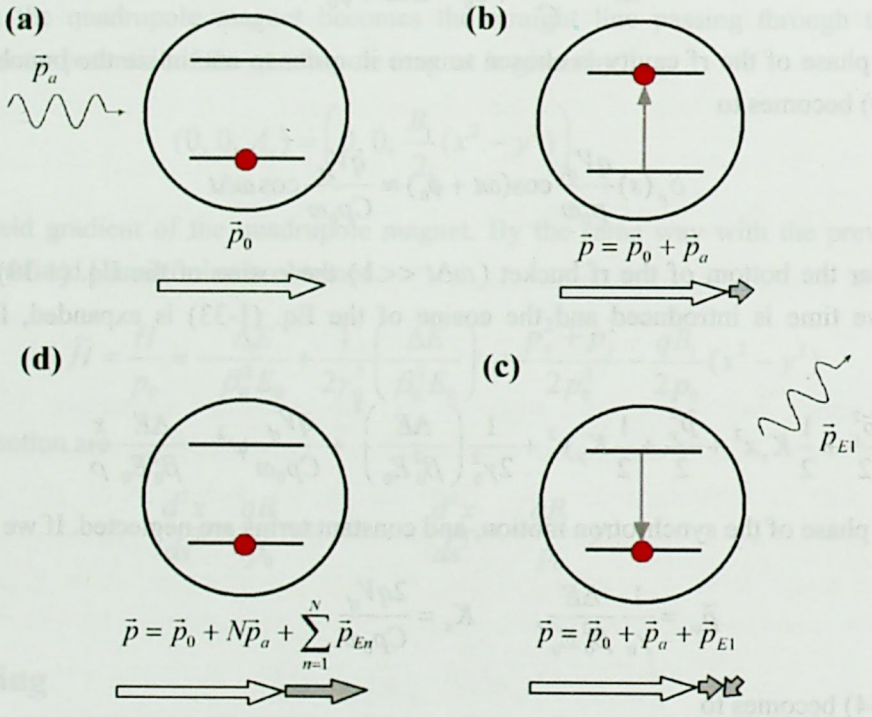

Fig. 1-3. Cycle of the resonant absorption of photon and spontaneous emission of a photon.

As the result, the ion gains a momentum to the direction in which the cooling laser irradiated. Therefore, the wavelength of the laser sensed and absorbed by the ion gradually shifts from the resonance wavelength. Thus, frequency of the absorption and emission decreases gradually. The excitation probability (photon absorption probability) P can be described by the well known Lorenzian line shape.

$$P = \frac{S/2}{(2\Delta/\Gamma)^2 + 1 + S} \tag{1-38}$$

where Δ is the frequency detuning

$$\Delta = 2\pi\nu(1-\beta)\gamma - 2\pi\nu_0 \tag{1-39}$$

γ, β are the relativistic factor of the target ion ν_0 is the resonance frequency in the ion rest frame and S is the saturation parameter defined by the ratio of the laser intensity and saturation density ($S=I/I_{sat}$). Therefore, the cooling laser gives the force depending on the velocity of the target ion v (Fig 1-4).

$$F(v) = \hbar k\Gamma P = \hbar k\Gamma \frac{S/2}{(2\Delta/\Gamma)^2 + 1 + S} \tag{1-40}$$

where k is the wave number of the laser photon Γ is the inverse life time of the upper excitation state of the ion ($\Gamma = 1/T$).

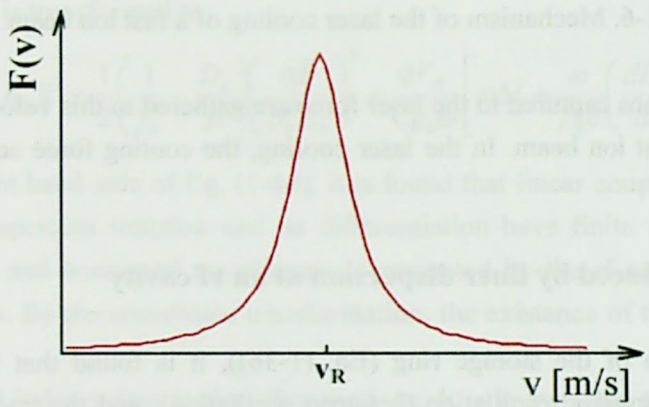

Fig 1-4. Shape of the laser force in velocity space.

When the cooling laser is superposed to the ion beam, the laser force acts so as to gather the ions in tail of the velocity distribution of the beam (Fig 1-5). If counter-propagating lasers are introduced, the shape of the laser force in the velocity space becomes as shown in Fig 1-6. In this case, a stable point is created in the

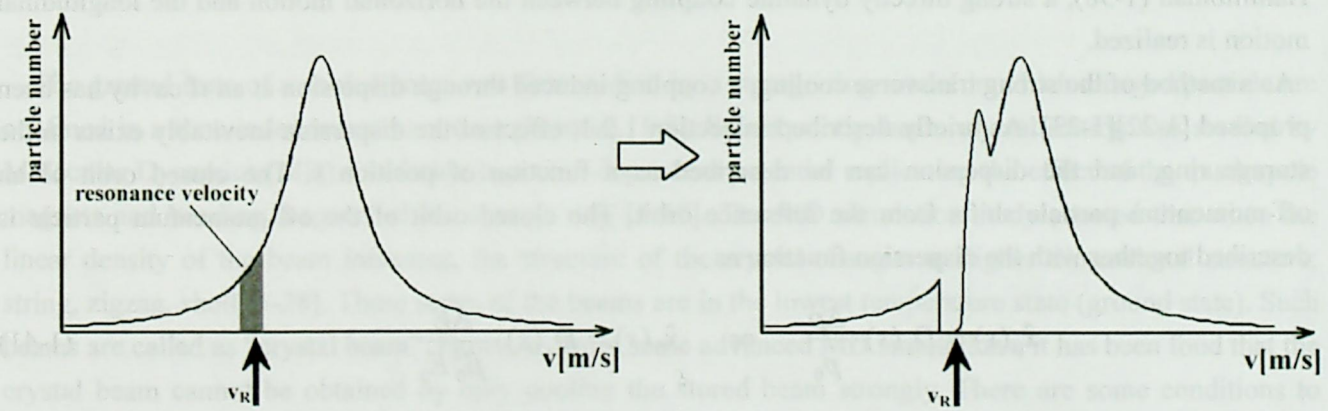

Fig 1-5. Change of the particle distribution in the velocity space by the laser force.

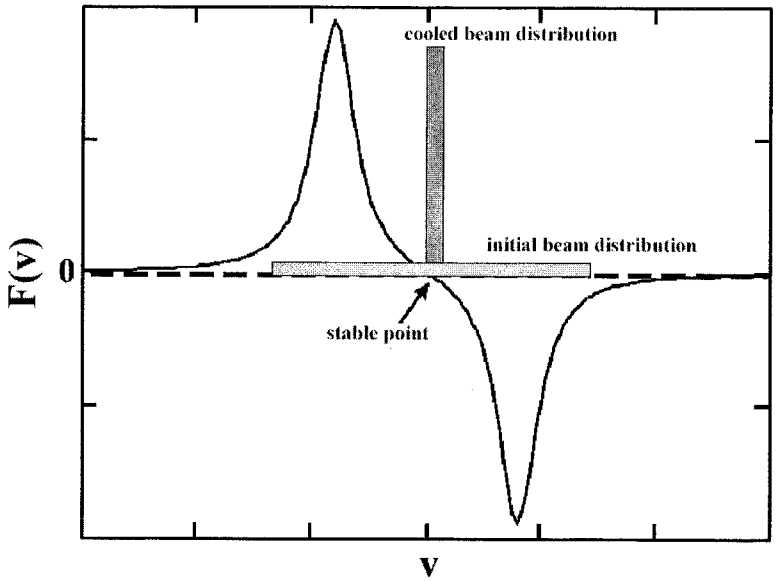

Fig 1-6. Mechanism of the laser cooling of a fast ion beam.

velocity space, and the ions captured to the laser force are gathered to this velocity. This is the mechanism of the laser-cooling of a fast ion beam. In the laser cooling, the cooling force acts on the longitudinal motion only.

1.4.2 3D cooling induced by liner dispersion at an rf cavity

From the Hamiltonian of the storage ring (Eq. (1-36)), it is found that the transverse motion of the reference particle is a harmonic oscillation (betatron oscillation), and the trace of the motion in the phase space becomes to an elliptical orbit. The area of this elliptical indicates the degree of the vertical motion and the vertical beam temperature and beam emittance.

The cooling force acts on the longitudinal motion only. By the effect of the intra-beam scattering, the transverse motion is also cooled slightly. However, the transverse cooling by the intra-beam scattering is insufficient for the achievement of the ultimate low temperature, low emittance beam. If the longitudinal motion and the transverse motion are strongly coupled, the betatron oscillation may damp accompanying the damping of the synchrotron oscillation due to the laser cooling. If such a term as $\Gamma\psi x$ exists in the Hamiltonian (1-36), a strong directly dynamic coupling between the horizontal motion and the longitudinal motion is realized.

As a method of the strong transverse cooling, a coupling induced through dispersion at an rf cavity has been proposed [1-22][1-23]. As briefly described in section 1.2.1, effect of the dispersion inevitably exists in the storage ring, and the dispersion can be described as a function of position s. The closed orbit of an off-momentum particle shifts from the reference orbit. The closed orbit of the off-momentum particle is described together with the dispersion function as

$$\hat{x}_0(s) = D_x(s)\cdot\frac{\Delta p}{p_0} \quad \text{or} \quad \hat{x}_0(s) = D_x(s)\cdot\frac{\Delta E}{\beta_0^2 E_0}. \tag{1-41}$$

These formulae are equivalent, but the second notation is used in this thesis. The momentum spread is constant of the motion, in a conventional magnetic storage ring. However, when the element of the storage ring includes electrostatic potential, the momentum-spread does not become the constant of motion. On the

other hand, the energy spread ΔE is the constant of the motion, even if the storage ring includes electrostatic potential (see chapter 4). Later, we establish the Hamiltonian formalism of a storage ring including not only magnetic field, but also electrostatic field. Thus, it is useful to use the second form of Eq. (1-41).

Next, we describe the motion of a particle, on the rest frame of the off-momentum particle. Then, the coordinate system is transformed. For example, the horizontal coordinate is rewritten by

$$\bar{x} = x - \hat{x}_0(s) = x - D_x(s) \cdot \frac{\Delta E}{\beta_0^2 E_0}, \tag{1-42}$$

and the other coordinates are also rewritten. This coordinate transformation from $(x, \tilde{p}_x, y, \tilde{p}_y, t, -\Delta E)$ to $(\bar{x}, \bar{p}_x, \bar{y}, \bar{p}_y, \bar{t}, -\Delta\bar{E})$ is summarized by the following generation function [1-24] [1-18]

$$F(x, \bar{p}_x, y, \bar{p}_y, t, -\Delta\bar{E}) = \left(x - \frac{\Delta\bar{E}}{\beta_0^2 E_0} D_x \right) \bar{p}_x + y\bar{p}_y - t\Delta\bar{E} + p_0 \frac{\Delta\bar{E}}{\beta_0^2 E_0} \frac{dD_x}{ds} x - \frac{p_0}{2} \left(\frac{\Delta\bar{E}}{\beta_0^2 E_0} \right)^2 D_x \frac{dD_x}{ds}. \tag{1-43}$$

Then the Hamiltonian (1-34) is transformed to

$$\tilde{H} = \frac{\bar{p}_x^2}{2} + \frac{1}{2} K_x \bar{x}^2 + \frac{\bar{p}_y^2}{2} + \frac{1}{2} K_y \bar{y}^2 + \frac{1}{2} \left(\frac{1}{\gamma_0^2} - \frac{D_x}{\rho} \right) \left(\frac{\Delta\bar{E}}{\beta_0^2 E_0} \right)^2 + \frac{qV_{rf}}{Cp_0\omega} \left[\omega\Delta\bar{t} + \frac{\omega}{\beta_0 c} \left(\frac{dD_x}{ds} x - D_x \bar{p}_x \right) \right]^2 + \ldots \tag{1-44}$$

From the 6th term of the right hand side of Eq. (1-44), it is found that linear coupling terms such as $\Gamma\overline{\psi x}$ arises ($\overline{\psi} = \omega\Delta\bar{t}$), if the dispersion function and its differentiation have finite value. Namely, the linear coupling of the longitudinal and horizontal coordinates is generated by the rf cavity existing in the place where finite dispersion exists. By the coordinate transformation, the existence of the linear coupling term is found out.

The vertical motion is still independent to the other motions. It is known that the vertical and horizontal motion is coupled by skew quadrupole magnet. By this way the motion of three directions is coupled. In order to maximize these coupling effect, the frequencies of the betatron oscillation (betatron tune ν_x, ν_z) and synchrotron oscillation (synchrotron tune ν_s) have to satisfy the resonance condition.

$$\nu_x - \nu_y = \text{integer}, \qquad \nu_x - \nu_s = \text{integer} \tag{1-45}$$

1.5 Crystal beam

The ground state of a cooled beam was first studied by a storage ring model in which charged particle are confined in a time independent harmonic potential [1-9]. Subsequently, beam crystallization was studied by Molecular Dynamics (MD) simulation in a time-dependent potential replicating the effect of the quadrupole magnets and bending magnets of the storage ring [1-27]. The MD simulation study showed that when the linear density of the beam increases, the structure of the crystal changes to higher dimensional structure; string, zigzag, shell [1-28]. These states of the beams are in the lowest temperature state (ground state). Such beams are called as "crystal beam". However, from some advanced MD simulations, it has been fond that the crystal beam cannot be obtained by only cooling the stored beam strongly. There are some conditions to achieve the crystal beam in a storage ring. The structure of various types of crystal beam are shown in Fig 1-7.

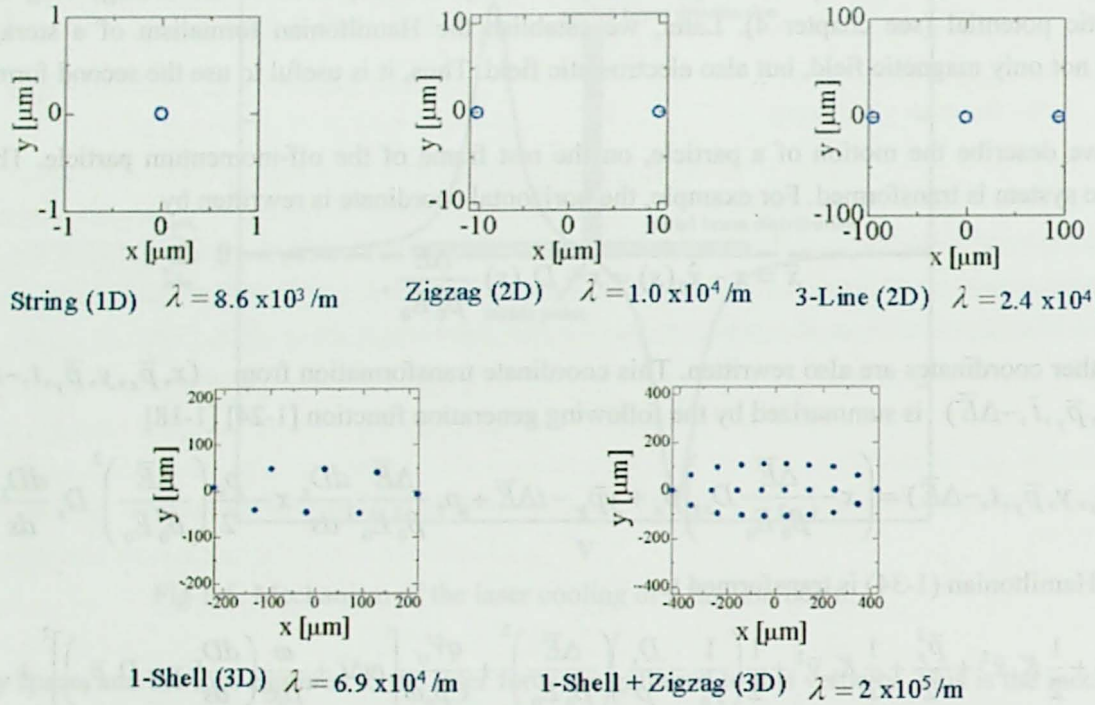

Fig 1-7. Cross-sectional view of the crystal beams. The λ means the line density of the beam. The crystal structure changes to higher dimensional structure, as the line density of the beam is enhanced. The 2D crystal structure extends in the weaker focusing direction of the ring. In this simulation, an ideal tapered cooling force is supposed. These structures were obtained by the MD simulation performed by Mr. Y. Yuri.

1.5.1 Hamiltonian of a space-charge dominated beam

When a beam temperature becomes low by the cooling, the space-charge effect becomes remarkably. In this section, the Hamiltonian of such space-charge dominated state is considered. When the space charge effect exists, the vector potential of the storage ring Eq. 1-29 becomes [1-25]

$$A_s = -\frac{B_y}{2}(\rho + x) + \frac{1}{2}B_1(x^2 - y^2) + A_{sc}, \tag{1-46}$$

where the rf cavity is switched off for simplicity, A_{sc} is the vector potential due to the space-charge force. A coasting beam is considered for simplicity, and it is assumed that the particles of beam have equilibrium distribution. Then, we can put $A_{sc} = \beta_0 V_{sc}/c$ [1-18]. V_{sc} is the scalar potential of the space-charge force. The mean field Coulomb potential V_{sc} can be written as [1-25]

$$V_{sc} = V_{sc,0} + \frac{1}{2}V_{sc,xx}x^2 + V_{sc,xy}xy + \frac{1}{2}V_{sc,yy}y^2 + \ldots\ldots \tag{1-47}$$

where $V_{sc,0}$ is a constant term, and

$$V_{sc,xx} = \frac{\partial^2 V_{sc}}{\partial x^2},\quad V_{sc,yy} = \frac{\partial^2 V_{sc}}{\partial y^2},\quad V_{sc,xy} = \frac{\partial^2 V_{sc}}{\partial x \partial y} \tag{1-48}$$

are partial derivatives of space-charge potential evaluated at the reference orbit. The scalar potential ϕ is

expressed as $\phi = V_{sc}$. The potential set to be zero at the reference orbit, that is $V_{sc,0} = 0$. Since the scalar potential exists, the Hamiltonian form of Eq. (1-14) is used. Substituting Eq. (1-46) for Eq. (1-14) and neglecting the higher-order terms, the following Hamiltonian is obtained.

$$\widetilde{H} = -\frac{\Delta E}{\beta_0^2 E_0} + \frac{1}{2\gamma_0^2}\left(\frac{\Delta E}{\beta_0^2 E_0}\right)^2 + \frac{\widetilde{p}_x^2 + \widetilde{p}_y^2}{2} + \frac{1}{2}\left(K_x x^2 + K_y y^2\right) + \frac{qV_{sc}}{p_0\beta_0 c\gamma_0^2} - \frac{\Delta E}{\beta_0^2 E_0}\frac{x}{\rho}. \tag{1-49}$$

When the explicit formula of the space-charge is substituted to Eq. (1-49), it becomes to

$$\widetilde{H} = \frac{1}{2}\left[\widetilde{p}_x^2 + \left(K_x + \frac{qV_{sc,xx}}{p_0\beta_0 c\gamma_0^2}\right)x^2\right] + \frac{1}{2}\left[\widetilde{p}_y^2 + \left(K_y + \frac{qV_{sc,yy}}{p_0\beta_0 c\gamma_0^2}\right)y^2\right] + \frac{qV_{sc,xy}}{p_0\beta_0 c\gamma_0^2}xy + \frac{1}{2\gamma_0^2}\left(\frac{\Delta E}{\beta_0^2 E_0}\right)^2 - \frac{\Delta E}{\beta_0^2 E_0}\frac{x}{\rho}, \tag{1-50}$$

where the relative time Δt has been introduced.

1.5.2 Maintenance condition

As shown in refs [1-18][1-25], the linear coupling term due to the space charge force is negligible; i.e. $V_{sc,xy} \approx 0$, when the particle distribution is assumed to be symmetric with respect to the reference orbit. Then, the equation of the betatron motion is given by

$$\frac{d^2x}{ds^2} \approx -\left(K_x + \frac{qV_{sc,xx}}{p_0\beta_0^2 c\gamma_0^2}\right)x + \frac{1}{\rho_0}\frac{\Delta E}{\beta_0^2 E_0} \tag{1-51-a}$$

$$\frac{d^2y}{ds^2} \approx -\left(K_y + \frac{qV_{sc,yy}}{p_0\beta_0^2 c\gamma_0^2}\right)y \tag{1-51-b}$$

For a cooled beam, we can put $\Delta E \approx 0$. $K_{x(y)}$ are functions of s and, they denote the beam focusing or defocusing effect of the lattice element of the storage ring. These equations are a kind of Hill's equation [1-29]. For a particle being confined in the storage ring, $K_{x(y)}$ have focusing effect i.e. $K_{x(y)}$ have positive sign on average. On the other hand $V_{sc,xx(yy)}$ denote the space charge repulsion, thus, they always have negative sign. Equations (1-51) have the form of the equation of motion of oscillators, in broad meaning. Therefore, the coefficients of x, y indicate the frequency of the betatron oscillation (betatron tune). If the beam is strongly cooled three-dimensionally, the amplitudes of the betatron oscillations damp accompanying the damping of the synchrotron oscillation. This means the beam size is reduced by the cooling. Then, the space-charge repulsion increases. Therefore, the focusing effect in Eq. (1-51) becomes weak, as the cooling progresses. And the tune value decreases. Therefore, the beam experiences various tune value in the cooling process. According to ref. [1-25][1-26], for a synchrotron made of N super periods, systematic half-integer stop-bands occur at the betatron tune $N/2\sqrt{2}$, $3N/2\sqrt{2}$ .... When the beam encounters this stop band in the cooling process, the beam temperature no longer decreases. If the betatron tune values of the initial beam are below $N/2\sqrt{2}$, the beam is cooled without experiencing such instability. And an ultimately low temperature beam is achieved. Therefore, in order to achieve the crystal beam, the betatron tune of the initial beam has to satisfy the condition

$$\nu < N/2\sqrt{2}. \tag{1-52}$$

This condition is called as *maintenance condition* together with the condition

$$\gamma < \gamma_t \tag{1-53}$$

where γ_t is the transition energy of the ring, γ is the Lorentz factor of the beam. The condition (1-53) is usually satisfied in the case of low energy beams.

1.5.3 Shearing force

Even if all conditions for generation of crystal beam are satisfied, there is an obstacle to reach a high intensity 3D crystal beam. The existence of the dispersion of the storage ring greatly affects to the stability of the 3D crystal structure. For a coasting beam the longitudinal equation of motion is obtained from Hamiltonian (1-50).

$$\frac{d(\Delta t)}{ds} = \frac{1}{\beta_0 c}\left[\frac{x}{\rho} - \frac{1}{\gamma_0^2}\left(\frac{\Delta E}{\beta_0^2 E_0}\right)\right] \tag{1-54-a}$$

$$\frac{d}{ds}\left(\frac{-\Delta E}{p_0}\right) = 0, \tag{1-54-b}$$

The first term of the right hand side of Eq. (1-54-a) arises from the shear term; $\Delta E/\beta_0^2 E_0 \cdot x/\rho$. (Note that the shear term gives the dispersion (section 1.3)).
For a crystalline state, ΔE is almost zero. Therefore the longitudinal equation of motion becomes to

$$\frac{d(\Delta t)}{ds} = \frac{1}{\beta_0 c}\frac{x}{\rho}. \tag{1-55}$$

Here Δt describe the difference of the time that a particle reaches to the same longitudinal position s as the reference particle. In a crystalline state, particles of the crystal beam stop the betatron oscillation, and behave as if *breathing* around the reference orbit [1-10] [1-25]. Therefore, in Eq. (1-55), the horizontal position of the particle x has always same sign. The coefficient of x has finite value in the bending section. Therefore, time difference Δt is increased whenever the particle passes through the bending section. Eventually this effect leads to the melting of the crystalline state (Fig 1-1). Since this effect behaves as if shearing the crystalline structure, we call this effect as *shear* or *shearing force*. For a bunched crystal beam, the time difference Δt is recovered at the rf cavity. However, the synchrotron oscillation is never damped, even if a strong cooling force is provided, and this limits the reachable temperature of the 3D crystal (see section 4.3).

For crystal beams, the shear term of the Hamiltonian of the storage ring gives the effect of "shear" and this effect obstructs the stable formation of a 3D crystal. We have found that if a bending electric field is introduced to a storage ring, in addition to the bending magnetic field, the shear term of the Hamiltonian of the storage ring is eliminated. Then, for a hot beam, the linear dispersion in the storage ring is canceled. For a crystal beam, the shearing force is canceled. In that case, the instability of the 3D crystal beam structure due to the shearing force is removed (see section 4.5).

1.6 Strategy of the present theses

The above mentioned 3D laser cooling method is to be performed in an actual storage ring S-LSR. S-LSR can operate satisfying the maintenance condition of a crystal beam. The parameters of laser cooling

experiment at S-LSR are shown in chapter 2.

As mentioned in previous sections, in order to generate a crystal beam in a storage ring, the maintenance condition has to be satisfied ideally. This means the number of super period of the ring should be the ideal number. Thus, the individual difference of the fabricated deflection element has to be suppressed as small as possible. Since the strongly cooled beam experience various betatron tune in the cooling process, the beam may encounter various resonance lines; for example, higher order resonances due to the multi-pole components, non-structural resonances due to the breakdown of the lattice symmetry. Therefore, the unwanted higher-order component field of the magnet has to be suppressed. From this point of view, the design of the bending magnet has one of the most important roles for the realization of a crystal beam at S-LSR. The detailed design process of the bending magnet aiming at realization of the ideal condition, described above, for crystal beam at S-LSR is shown in chapter 3, and the details of the evaluation of the fabricated magnets are also shown in chapter 3. The ideal state for the crystal beam is also preferable for the conventional storage and cooling of beams.

Even if the above described ideal condition for crystal beam is satisfied, the generation of a beam which has a stable 3D crystal structure is difficult due to the problem of the bending shear, as described in section 1.5.3. The problem of bending shear is solved by the introduction of a dispersion-free deflector which includes a bending electric field, in addition to the bending magnetic field. For the case of S-LSR, the dispersion-free deflector is realized by inserting a cylindrical electrostatic deflector in the gap of the banding magnet. The electrostatic deflector for S-LSR has intermediate electrodes in order to maintain the field strength and distribution in a limited gap area of the bending magnet. A storage ring constructed with the dispersion-free deflectors has interesting properties, not only the solution of the problem of the bending shear. These are descried in chapter 4.

In order to realize the ideal dispersion-free state in the deflector, the bending magnetic field and the electric field have to be superposed completely in the same region. However, it is difficult to superpose the both field completely in the fringing region due to the difference of the gap size and the end structure of each bending element. If at least the effective lengths of the both fields become identical, the beam can be circulated stably, although it is different from the ideal state. Thus the effective length and the structure of the fringing field were designed, considering the consistency with the magnetic field distribution obtained from the field measurement. In chapter 4, the structure of the electric field of the dispersion-free deflector of S-LSR has cylindrical electric field, which is the simplest solution of Maxwell equation. However, in this case of S-LSR, it cannot be operated satisfying the maintenance condition of crystal beams. Therefore, in chapter 5, different type of electric field for dispersion compensation is investigated. Finally, it is found that radially uniform electric field, which is attained by semi-hyperbolic electrodes, is suitable. It is also found that this type of electric field can be realized, only changing the applied voltage of the intermediate electrodes of the fabricated cylindrical electrostatic deflector of S-LSR.

The three-dimensional cooling method by a normal rf cavity becomes not to be applicable in exchange for the dispersion-free condition. Therefore, in the case of dispersion-free storage ring, so-called coupling rf cavity has to be used for the 3D cooling. The coupling rf cavity can generate a direct coupling between the longitudinal motion and the horizontal notion without dispersion (section 5.7).

References

[1-1] J. J. Bollinger and D. J. Wineland, Phys. Rev. Lett. **53**, 348 (1984).

[1-2] F. Diedrich, E. Peik, J. M. Chen, W. Quint, and H. Walther, Phys Rev Lett. **59**, 2931 (1987).

[1-3] M. Drewsen, C. Brondersen, L. Hornkær, J. S Hangst and J. P. Schiffer, Phys. Rev. Lett. **81** (1988) 2878

[1-4] M. Steck, K. Beckert, H. Eickhoff, B. Franzke, F. Nolden, H. Reich, B. Schlitt, and T. Winkler, Phys. Rev. Lett. **77**, 3803 (1996).

[1-5] H. Danared, A. Källberg, K.-G. Rensfelt, and A. Simonsson, Phys. Rev. Lett. **88**, 174801 (2002)

[1-6] H. Okamoto, K. Okabe, Y. Yuri, D. Möhl and A. M. Sessler, Phys. Rev. E **69**, 066504 (2004).

[1-7] T. schätz, U. Schramm, D. Habs, Nature (London) **412**, 717 (2001);
U. Schramm, T. Schätz, and D. Habs, Phys. Rev. E **66**, 036501 (2002)

[1-8] U. Schramm, T. Schätz, and D. Habs, Phys. Rev. Lett. **87**, 184801 (2001)

[1-9] A. Rahman, and J. P. Schiffer, Phys, Rev. Lett. **57**, 1133 (1986)

[1-10] J. Wei, X.-P. Li, and A. M. Sessler, Phys. Rev. Lett. **73**, 3089 (1994).

[1-11] J. Wei, H. Okamoto, and A. M. Sessler, Phys. Rev. Lett. **80**, 2606 (1998).

[1-12] H. Okamoto, J. Wei, Phys. Rev. E. **58**, 3817 (1998)

[1-13] T. Kihara, H. Okamoto, Y. Iwashita, K. Oide, G. Lamanna, J. Wei, Phys. Rev. E, **59**, 3594 (1999)

[1-14] A. Noda, Nucl. Instrum. Methods. A **532**, 150 (2004);
A. Noda, H. Fadil, S. Fujimoto, M. Ikegami, Y. Iwashita, S. Nakamura, T. Shirai, M. Tanabe, H. Tongu, K. Matsukado, K. Noda, S. Shibuya, T. Takeuchi, S. Yamada, H, Daido, Y. Kato, T. Tajima, M. Beutelspacher, M. Grieser, E. Syresin, in Proceedings of EPAC 2004, (2004);
A. Noda, Proceedings of the workshop on ion beam cooling toward the crystalline beam, Kyoto, 12-14 November 2001, p3 (2001)

[1-15] H. Okamoto, Nucl. Instrum. Methods. A **532**, 32 (2004).

[1-16] S. Y. Lee, *Accelerator Physics*, (World Scientific (Singapore)) p30 (1999);

[1-17] K. Oide、"*Introduction of Beam dynamics*" *Proc. First workshop.* JLC-FFIR92 12/16-18, 1992, KEK Proceedings 93-6, [in Japanese]
http://www-jlc.kek.jp/subg/ir/lib/DOC/japanese/Lecture.beam.dynamics.ps

[1-18] H. Okamoto, S. Machida, Nucl. Instrum. Methods. A **482** (2002) 65.

[1-19] T. Suzuki, Part. Accel. **12**, 237 (1982)

[1-20] J. Javanainen, M. Kaivolan, U. Nielsen, O. Poulsen, and E. Riis, Journal of the Optical Society of America B **2** (1985), 1768

[1-21] N. Madsen, "Dynamics of laser cooled ion beams" Dissertation; Institute of Physics and Astronomy, University of Aarhus, Denmark (1998)

[1-22] H. Okamoto, Phys. Rev. E. **50**, 4982 (1994)

[1-23] H. Okamoto, A. M. Sessler, D. Möhl, Phys. Rev. Lett. **72**, 3977 (1994)

[1-24] "*The front line of the present-day physics 1*" edited by Y. Otsuki (Kyouritsu Syuttupan, Tokyo) [in Japanese]

[1-25] S. Y. Lee, H. Okamoto Phys. Rev. Lett. **80**, 5133 (1998).

[1-26] J. Wei, A. Draeseke, A. M. Sessler, and X. P. Li, "*The Crystalline Beams and Related Issues*" (World Scientific (Singapore) 1996) p. 229

[1-27] J. P. Schiffer and A. Rahman, Z. Phys. A. **331**, 71 (1988)

[1-28] p15 of ref. [1-21]

[1-29] A. Morita, "performance assessment of a combined function type synchrotron based on an extremely precise field measurement" Dissertation; Department of Physics, Faculty of Science, Kyoto-University (2002) p98

Chapter 2. Ion storage ring S-LSR

2.1 Outline of S-LSR project

A heavy ion storage ring S-LSR is now under construction by collaboration between National Institute of Radiological Science and ICR, Kyoto University. The circumference of S-LSR is 22.557 m. This is compact compared with the other storage rings [2-3]. An electron cooler and a laser cooling system are equipped to S-LSR. The major purposes of the S-LSR project are the feasibility study of application of laser produced carbon ions as the injection for cancer-dedicated pulse-synchrotron, and approach to the ultra-cold beam with use of laser cooling for low energy $^{24}Mg^{+}$ beam. The electron cooling is applied to the hot carbon ion beam after phase rotation of the laser produced carbon ions [2-1]. In S-LSR, the fast extraction of electron cooled short-bunch beams is also studied. In Fig. 2-1, the layout of S-LSR is illustrated and its main parameters are listed in Table 2-1.

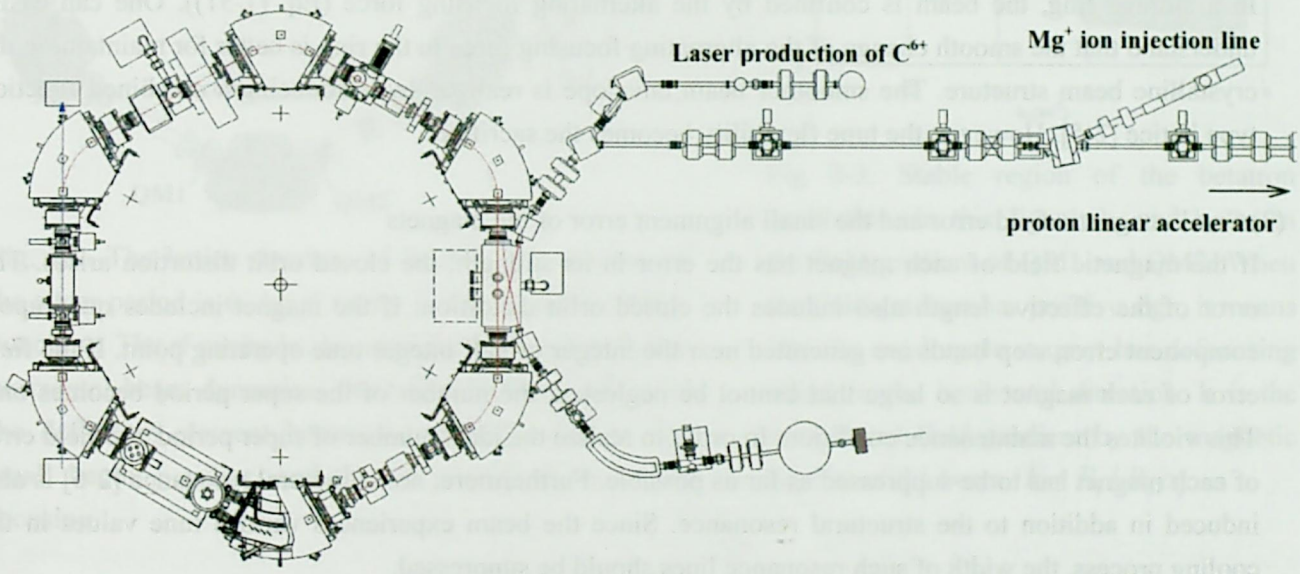

Fig. 2-1. Layout of S-LSR ring

Table 2-1 Main parameters of S-LSR

Parameters	Value
Kinetic energy of C^{6+}	24 MeV (2 Mev/u)
Kinetic energy of Mg^{+}	35 keV
Kinetic energy of p	7 MeV
Circumference	22.557 m
Average radius	3.590 m
Radius of the bending section	1.05 m
Number of the super period	6
Deflection angle of each bending magnets	60°

2.2 Lattice design of S-LSR

2.2.1 Design principle

The conditions for maintaining crystal beam gives the strongest restriction to the lattice design among the research subjects of S-LSR. Therefore, the lattice design principle was almost dominated by the conditions for the crystal beam [2-4]. The following conditions were considered.

(1) Small betatron phase advance.

In order to create a crystalline state beam, the horizontal and the vertical betatron tune have to be below $N/2\sqrt{2}$ (N is the number of the super period). Namely, a small phase advance per one super period is required.

(2) Smooth beam envelope

In a storage ring, the beam is confined by the alternating focusing force (Eq. (1-51)). One can easily understand that the smooth change of the alternating focusing force in the ring is better for maintaining the crystalline beam structure. The smoother beam envelope is realized by introducing a combined function type lattice [2-5]. However, the tune flexibility becomes the sacrifice.

(3) Small magnetic field error and the small alignment error of the magnets

If the magnetic field of each magnet has the error in its strength, the closed orbit distortion arises. The error of the effective length also induces the closed orbit distortion. If the magnet includes quadrupole component error, stop bands are generated near the integer or half integer tune operating point. If the field error of each magnet is so large that cannot be neglected, the number of the super period becomes one. This violates the maintenance condition. In order to realize the ideal number of super period, the field error of each magnet has to be suppressed as far as possible. Furthermore, non-structural resonance [2-6] is also induced in addition to the structural resonance. Since the beam experiences various tune values in the cooling process, the width of such resonance lines should be suppressed.

(4) Small magnetic non-linear components of the magnetic field

The beam experiences various tune values until the beam becomes to ground state. If the elements of the storage ring including the non-linear field components, higher-order stop band is generated. The cooled beam has a possibility to encounter this stop band during the cooling process. If the width of the stop band is very wide, the beam may not be able to overcome the stop band.

(5) Long straight section for the electron cooling and the laser cooling

The laser cooling efficiency is proportional to the length in which the beam and laser light are superposed. Similarly the efficiency of the electron cooling is proportional to the length in which the ion beam and electron beam are superposed. Since the attachments of the electron cooler occupy considerable area, it is needed to ensure enough long straight section.

2.2.2 Lattice structure of S-LSR

In order to realize the situation that the condition (1) consists with (5) by the small circumference, the number of the super period was selected to 6. Then, the length of the straight section and the bending radius were decided to 1.86 m and 1.05 m, respectively. The arrangement of the magnets was decided as shown in Fig 2-2.

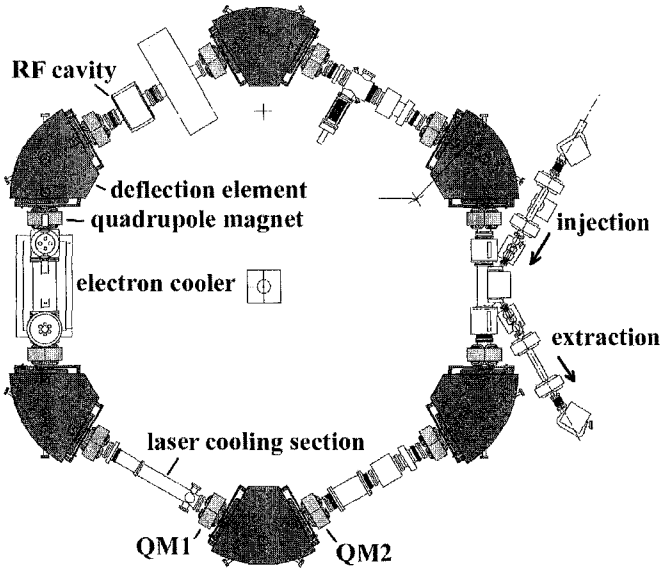

Fig. 2-2. The lattice structure of S-LSR. The number of the super-period is 6. An rf cavity is introduced for beam bunching. The rf cavity is also used for 3D cooling. In the horizontal beam dynamics, the radial focusing effect of the deflection element becomes remarkable due to the small bending radius, and thus it is utilized for beam focusing.

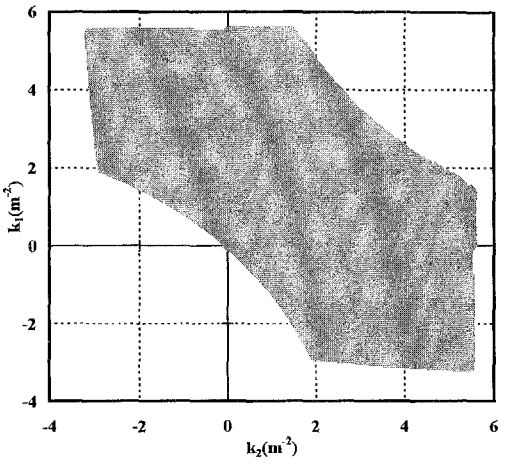

Fig 2-3. Stable region of the betatron oscillation. In this figure, k_1 and k_2 mean the field gradient of QM1 and QM2. When the field gradient has positive sign, it means that the quadrupole magnet has defocusing effect in the horizontal direction. k is the normalized field gradient by the magnetic rigidity of the beam $k = B_1 / B_0 \rho_0$

The one super period is composed of lattice elements as drifr/2-QM1-BM-QM2-drift/2. The stable region of the betatron oscillation is shown in Fig 2-3. The stable operation is possible in the state that the both quadrupole magnets have defocusing horizontally (1) or, one quadrupole magnet has horizontal focus, the other quadrupole magnet has horizontal defocus (2), (3) (Fig 2-4).

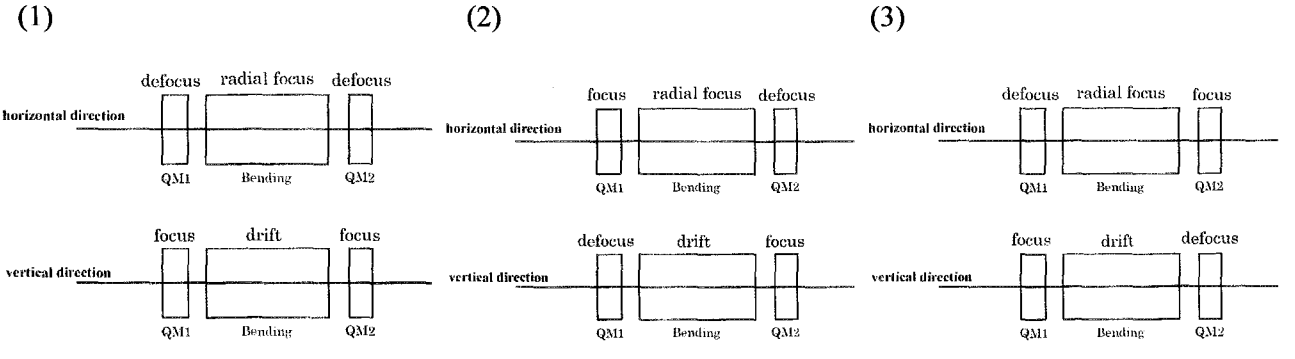

Fig 2-4. Possible polarity of the QM1 and QM2

As the operating point of Mg^+, the point in which the field gradient of the quadrupole magnet $k_1=k_2=1.27\ m^{-2}$ and betatron tune (1.446, 1.436) has been supposed. At this operating point, the needed synchrotron tune for the 3D cooling becomes 0.44. The parameters at the operating point (1.446, 1.436) are shown in Table 2-2. It is found that in this operating point, the needed values of the harmonic number become very large. Therefore the 3D cooling will be performed at the operating point (2.067, 1.073), rather than this operating point. The beta-functions and dispersion function of the operating points (1.446, 1.436) and (2.067, 1.073) are shown in Fig. 2-5, respectively. The both operating points satisfy the maintenance condition $\nu_T < N/2\sqrt{2}$.

Table 2-2-a. Main parameters of the rf cavity for 3D cooling Operation point (1.446, 1.436).

Quantity	Value
Ions to be laser cooled	$^{24}Mg^+$
Total kinetic energy	35 keV
Betatron tune	(1.446, 1.436)
Synchrotron tune	0.44
rf voltage	125 V
rf frequency	46.4 MHz
rf harmonics	2000
Momentum compaction factor	0.664

Table 2-2-b. Main parameters of the rf cavity for 3D cooling. Operation point (2.067, 1.073).

Quantity	Value
Ions to be laser cooled	$^{24}Mg^+$
Total kinetic energy	35 keV
Betatron tune	(2.067, 1.073)
Synchrotron tune	0.07
rf voltage	127 V
rf frequency	2.32 MHz
rf harmonics	100
Momentum compaction factor	0.325

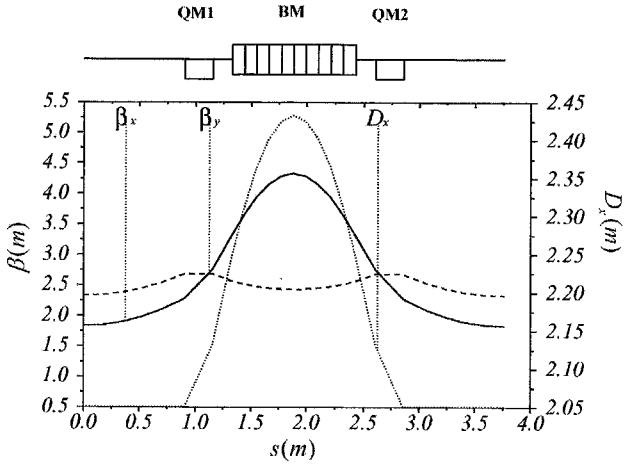

Fig 2-5-a. The lattice functions at the operating point (1.446, 1.436). Beta-functions and dispersion function are drawn as a function of the position s. In this operating point, 3D cooling may be difficult because a high efficiency rf cavity is required to induce the synchro-betatron coupling. This operating point will be used for cooling experiments of costing beams. The transition energy of this operating point is $\gamma_t = 1.231$.

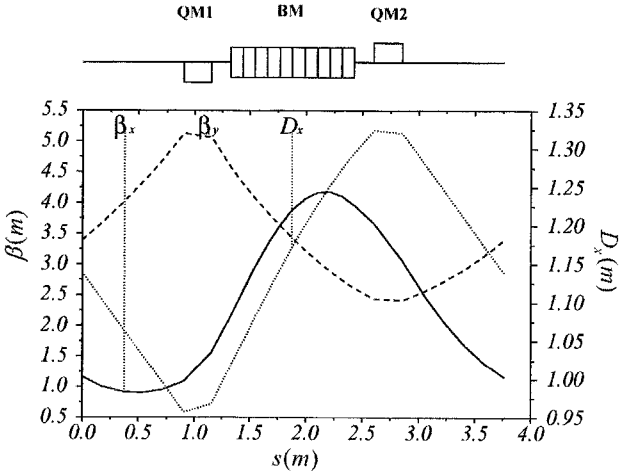

Fig 2-5-b. The lattice functions at the operating point (2.067, 1.073). In this case the field gradient of QM1 and QM2 selected to $k_1=2.05\ m^{-2}$ and, $k_1=-1.12\ m^{-2}$ respectively. the minus sign means the magnet has focusing effect in the horizontal direction. The transition energy of this operating point is $\gamma_t = 1.754$.

2.3 Laser cooling

The ion species possible to be cooled by laser are Li^+, Be^+, Mg^+ and Ca^+, etc. Most of the ion species requires two kinds of lasers because of the level splitting. Only Mg^+ is possible to be cooled by a single wavelength of 280 nm. Therefore, we decided to use Mg^+ beam as the beam to be laser cooled. The circulation life time of the Mg^+ beam in the ring becomes longer in the lower energy region [2-5]. In the present plan, the kinetic energy of Mg^+ ion is planned to be 35 keV. The expected life time is longer than 20 seconds, when the vacuum pressure better than a few times of 10^{-11} Torr is attained. And, in this energy region, the Lorentz factor γ is almost 1. Thus the maintenance condition $\gamma_t > \gamma$ is enough satisfied. The ion is injected to the ring directly from the ion source, therefore the kinetic energy is decided by the extraction high voltage of the ion source. For the cooling of 35 keV Mg^+, counter propagating lasers of the wavelength 280 nm are to be used. First, the laser photons are generated by a green laser of the wavelength 532 mm. Next, a dye is excited by the green laser and then wavelength of 560 mm laser is emitted. Finally, the dye laser is modulated to the wavelength of 280 nm by a sub harmonic generator [2-1].

2.4 Required performance of the bending magnet

As shown in Fig 2-5, the horizontal beta function in the bending section becomes larger compared to the one in the straight section. Therefore, useful horizontal aperture of the bending magnet has to be extended compared to the straight section. From the consideration of the injection and extraction of the beams, the horizontal usable aperture of the bending magnet was decided to 200 mm. Since the major use purposes of S-LSR are not synchrotron acceleration of the beams, but the storage and the cooling of ion beams, the main magnets (the bending magnets and the quadrupole magnets) are made by not lamination iron plates, but solid iron. In this case, the fabrication error of the magnet can be suppressed well. This is desirable to satisfy the condition (3) listed in section 2.2.1. Furthermore, the magnets of S-LSR were designed with the use of high precision 3D field calculation code. Various structures of magnets were tested in the field simulation, and the most suitable structure to suppress the multi-pole field was decided.

Even though the condition to attain a crystal beam is satisfied by the present method, the realization of a stable large 3D crystal beam structure is thought to be difficult due to the effect of the bending shear. Thus the introduction of the dispersion-free system mentioned in chapter 1 was decided.

References

[2-1] A. Noda, Nucl. Instrum. Methods. A **532**, 150 (2004);

[2-2]A. Noda, H. Fadil, S. Fujimoto, M. Ikegami, Y. Iwashita, S. Nakamura, T. Shirai, M. Tanabe, H. Tongu, K. Matsukado, K. Noda, S. Shibuya, T. Takeuchi, S. Yamada, H, Daido, Y. Kato, T. Tajima, M. Beutelspacher, M. Grieser, E. Syresin, in Proceedings of EPAC 2004, (2004);

[2-3] A. Noda, *in Proceedings of the workshop on ion beam cooling toward the crystalline beam, Kyoto, 12-14 November 2001*, edited by A. Noda and T. Shirai (World Scientific, Singapore, 2001) p3-14

[2-4] T. Shirai, H. Fadil, M. Ikegami, A. Morita, H. Tongu, A. Yamazaki, Y. Iwashita, A. Noda, K. Okabe, Y. Yuri, H. Okamoto, M. Grieser, in Proceedings of EPAC 2002, Paris, France (2002)

[2-5] T. Shirai, H. Fadil, Y. Iwashita, A. Morita, A. Noda, H. Tongu, A. Yamazaki, *in Proceedings of the*

workshop on ion beam cooling toward the crystalline beam, Kyoto, 12-14 November 2001, edited by A. Noda and T. Shirai (World Scientific, Singapore, 2001) p29-40

[2-6] A. Morita, "performance assessment of a combined function type synchrotron based on an extremely precise field measurement" Dissertation; Department of Physics, Faculty of Science, Kyoto-University (2002) p105-106

Chapter 3. Design and field measurement of dipole magnets for S-LSR

3.1 Introduction

As mentioned in the previous sections, in order to realize the ideal condition for a crystal beam, the unwanted higher-order component of the bending magnet has to be suppressed, in the stage of the design. The fabricated magnets have to be evaluated precisely, because the arrangement of the magnets is decided based on the actual field distribution so that the closed orbit distortion is suppressed. Furthermore, the precise evaluation of the effective length is needed to consider the consistency with the effective length of the electrostatic deflector for dispersion compensation.

3.1.1 Outline of electromagnet

A ferromagnetic metal and a coil shown in Fig. 3-1 are considered. We suppose that the magnetic flux density is B and B_1 in the air gap and the metal, respectively. When Ampére's law

$$\oint \vec{H} \cdot d\vec{s} = NI \tag{3-1}$$

is applied to the pass shown in Fig. 3-1, the following relation is obtained

$$\frac{Bg}{\mu_0} + \frac{B_1 l}{\mu_0 k_\mu} = NI \tag{3-2}$$

where μ_0 is permeability of air, and k_μ is relative permeability of the metal. In ferromagnetic metals, the value of k_μ is about 10^2 to 10^4. Therefore, the second term of the left hand side is negligible. Then, the magnetic flux density in the gap is approximately obtained as

$$B = \frac{\mu_0 NI}{g} \tag{3-3}$$

where $\mu_0 = 4\pi \times 10^{-4} H/m$. From this relation, we can estimate the needed current I and the turn number of the coil N to generate the magnetic flux density B, with the gap height g.

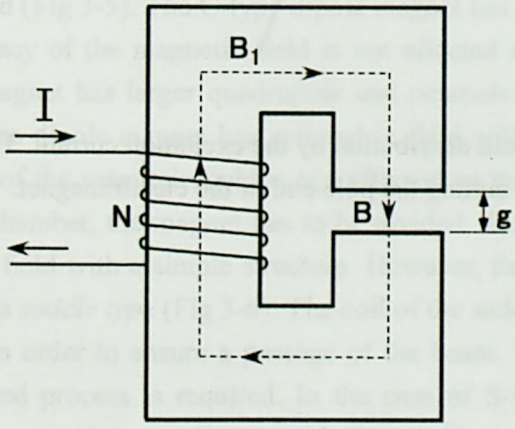

Fig 3-1. An example of electromagnet.

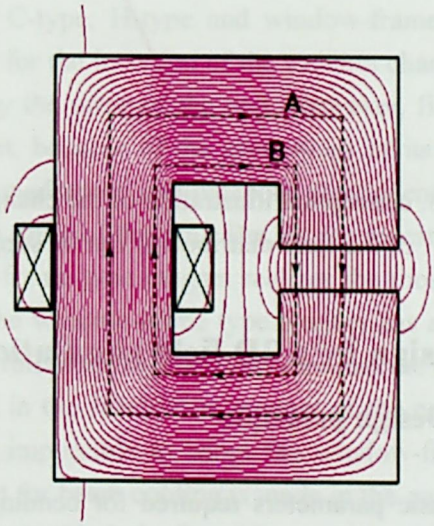

Fig 3-2. Flux in the electromagnet

3.1.2 Saturation of the magnetization

The magnetic flux density is given by the relation

$$\vec{B} = \mu\vec{H}, \tag{3-4}$$

although, the permeability is not constant in ferromagnetic metals. The relation between B and H is given by B-H curve in ferromagnetic metals (for example, see Fig. 3-4). The value of $\mu = k_\mu \mu_0$ decreases as H becomes large. The magnetic field H in the electromagnet is decided by the excitation current I from Ampére's law. Therefore, for a high excitation current the second term of the left hand side of Eq. (3-2) cannot be neglected and, the efficiency of the excitation of the field becomes worse. This situation is called as *saturation* of magnetization. The effect of the saturation restricts the upper limit of the efficient magnetic flux density.

In general, at the both ends of the pole, the magnetic field H in the iron becomes higher than that of the center of the pole. As the excitation level becomes high, the iron of the pole end saturates earlier than the center of the pole. Then, we consider that Ampére's law is applied for the pass A and B in Fig (3-2). For the pass B, the second term in the right hand side of Eq. (3-2) can not neglect at the pole end because the permeability reduces in this area. And the magnetic flux density in the air gap reduces in exchange for the increase of the second term in the right hand side of Eq. (3-2). Thus, for a high excitation current, the magnetic flux density around the end of the gap becomes lower than that of the center of the gap. Namely, the field distribution in the gap changes by the excitation current (Fig. 3-3). This is one of the matters, which has to be conquered in the design of the magnet for synchrotron. The measures to solve this matter are to cut beforehand the both ends of the pole, which are the parts easy to be saturated. By this method, a field distribution without depending on the excitation current is realized. The ideal shape of the pole end cut is given by Rogowski's curve. [3-1]

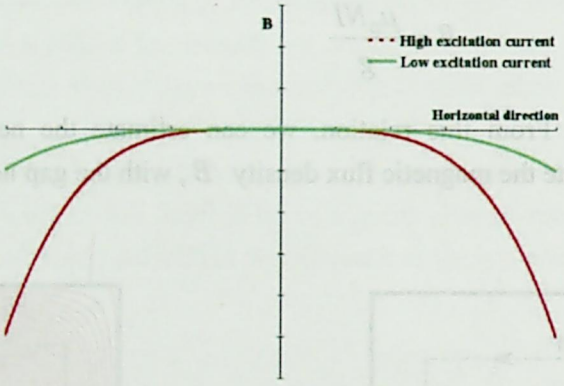

Fig 3-3. conceptual illustration of the change of the field distribution by the excitation current. The change of the field distribution can be suppressed by cutting the pole end of the electromagnet.

3.2 Design by a 2D field simulation

3.2.1 Design principle

The basic parameters required for bending magnet are listed in Table 3-1. Although the required field strength for the present experiment is about 0.4 T, the maximum magnetic field has been set to 0.95 T in consideration of the possible future ramp up of energy.

Table 3-1. Required parameters

Parameters	Value
Bending angle	60°
Edge angle	0°
Bending radius	1050 mm
Horizontal useful aperture	200 mm
Field strength for 7 MeV p	0.363 T
24 Mev C^{6+}	0.387 T
35 keV Mg^{+}	0.125 T
Mass upper limit	5.0 tons
Gap height	70 mm

The gap height is determined to be 70 mm, compromising the usable vertical aperture and the needed excitation current. Then, the needed excitation current to generate 0.95T is about 54000 AT. All parts of the pole and yoke are constructed with pure soft iron which has a good magnetic property. The B-H curve of the pure soft iron is shown in Fig. 3-4.

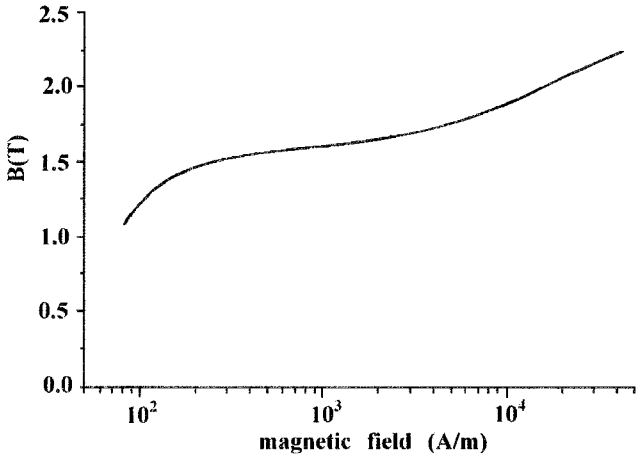

Fig. 3-4. B-H curve of iron used for S-LSR magnet

There are several types of dipole magnets. For example, C-type, H-type and window-frame type are considered (Fig 3-5). The C-type dipole magnet has advantage for the insertion of the vacuum chamber. And the accuracy of the magnetic field is not affected so much by the error of the coil. However, field of the C-type magnet has larger quadrupole and octapole component, because of the asymmetry of its structure. The H-type dipole magnet has symmetric field with a small quadrupole and octapole component. And the accuracy of the magnetic field is not affected so much by the error of the coil. But, in the insertion of the vacuum chamber, the magnet has to be divided. The window-frame type magnet realizes the most uniform magnetic field with a simple structure. However, the coil of the window-frame type magnet has a structure so-called a *saddle type* (Fig 3-6). The coil of the saddle type is raised at the beam entrance and the exit of the magnet, in order to ensure a passage of the beam. Therefore, in the fabrication process of the coil, a little complicated process is required. In the case of S-LSR, it is impossible to adopt the window-frame type magnet, because it is required that a hole to guide the laser light for beam cooling is made in the outer side of the magnet. The coil of the window-frame type magnet obstructs this hole. For this reason, window-frame type cannot be adopted. Therefore, the choice is restricted to the C-type or the H-type. Since the H-type has

larger advantage in compactness and the quality of the field compared with C-type, the H-type magnet is adopted for S-LSR.

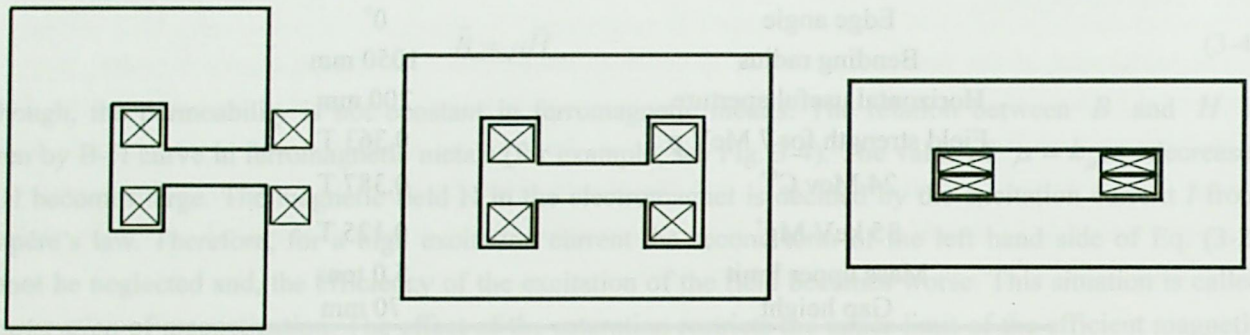

Fig 3-5 (a) C-type magnet (b) H-type magnet (c) window frame type magnet

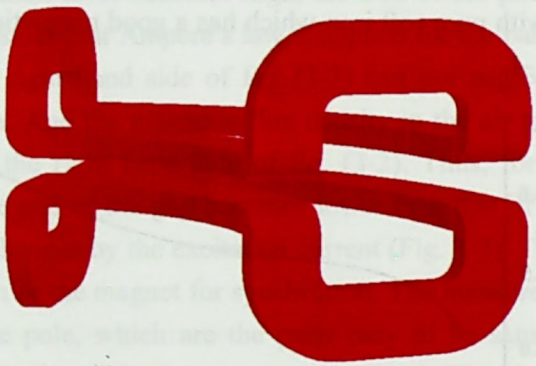

Fig 3-6. Structure of the saddle type coil

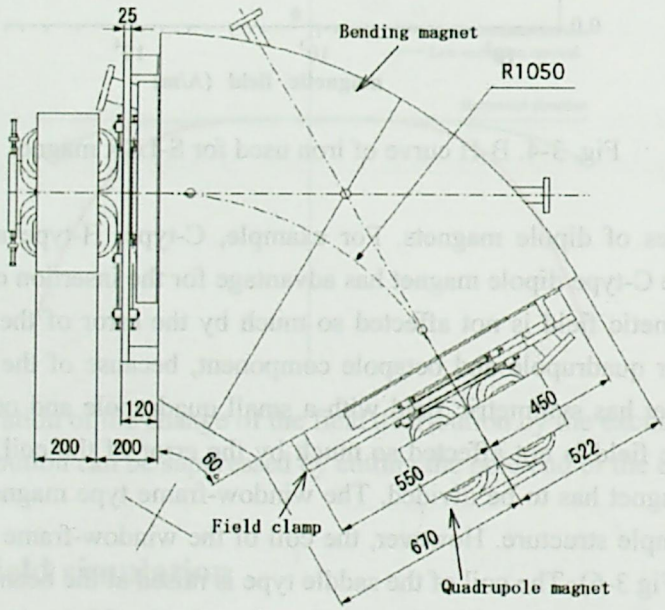

Fig 3-7. The overview of the magnet series for S-LSR

The layout around the bending magnet is shown in Fig. 3-7. The shape of the magnet is determined to be fan-shape to reduce the *sagitta*. At the entrance and the exit of the bending magnet, *field clamp* plates are set

to cut the tail of the fringing field. The field clamp plate also has an advantage suppressing the sextupole component in the fringing field region [3-2](see Section 3.3.3.4).

3.2.2 Design of the radial cross section structure

The required horizontal usable aperture is 200 mm, this value was determined from the beam parameters of the injection of 7 MeV proton. In the first stage of the design of the bending magnet, the details of the radial cross section shape of the magnet were determined by a 2D field calculation under axial symmetry condition. The goal of this process was to determine the structure generating uniform field, with a compact iron yoke. The cross section structure is shown in Fig. 3-8. At both ends of the pole, so-called *shims* are attached to realize uniform field by a narrow pole (Fig. 3-9). And the both ends of the pole are cut in a circle to avoid the change of the field distribution due to the effect of saturation. As the cutting management of the pole end, a straight cut was also considered. However, from the result of the 2D field calculation, we have found that when the straight cut is adopted, the wider pole width is required to realize the same effective field area compared with the case of circle cut.

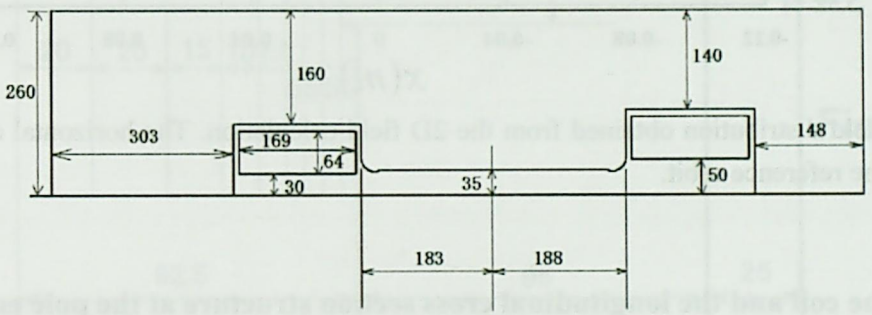

Unit: mm

Fig. 3-8. Upper half of the cross section of the bending magnet

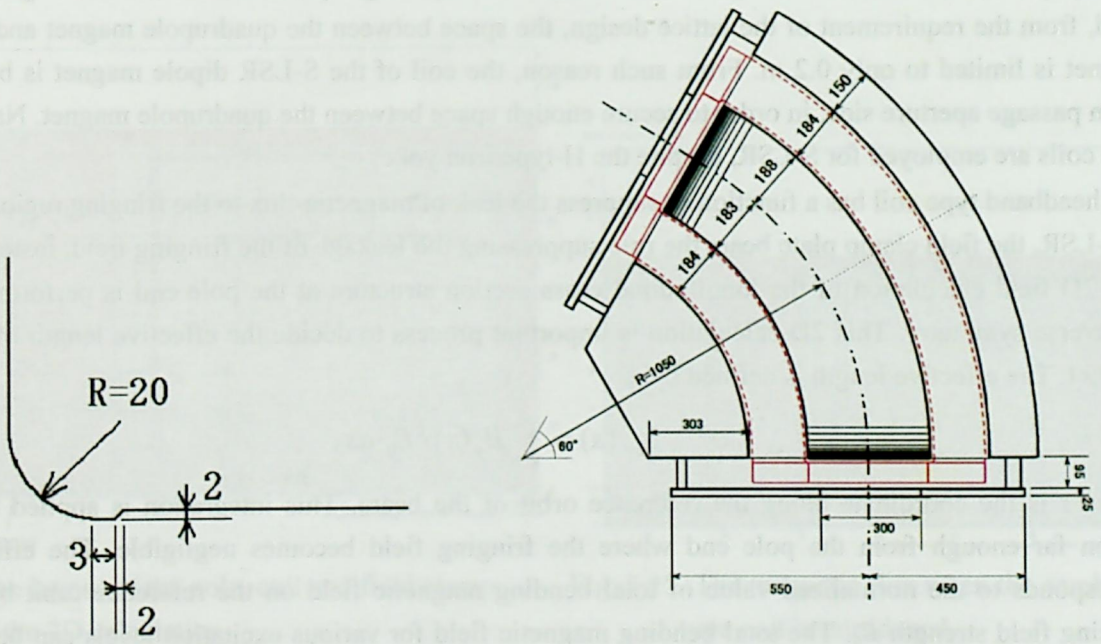

Fig. 3-9. The structure of the pole end cut and shim and the overview of the magnet

Since the magnet has fan shape, the inner return yoke designed so as to have thicker radial width compared to the outer yoke, as shown in Fig. 3-9. By this way, the flux density in the outer and inner return yoke was kept in the same level. The calculated field distribution is shown in Fig. 3-10. The deviation of the field strength is less than 5×10^{-5} at all excitation level.

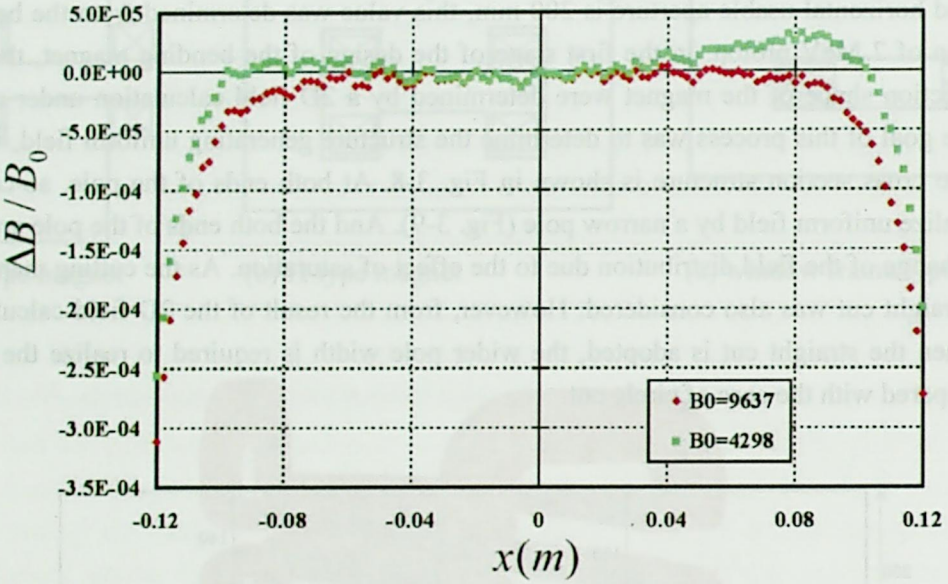

Fig. 3-10. Radial field distribution obtained from the 2D field calculation. The horizontal coordinate means the distance from the reference orbit.

3.2.3 Design of the coil and the longitudinal cross section structure at the pole end

In a conventional case, a headband type coil is utilized for H-type magnet. In order to ensure a large turn number of the coil, keeping the iron core to be light weight, the cross section shape of the coil should be wide (Fig 3-8). Then, the overhang of the coil at the beam passage aperture side becomes large. On the other hand, from the requirement of the lattice design, the space between the quadrupole magnet and the bending magnet is limited to only 0.2 m. From such reason, the coil of the S-LSR dipole magnet is bent up at the beam passage aperture side, in order to secure enough space between the quadrupole magnet. Namely, saddle type coils are employed for S-LSR, despite the H-type iron yoke.

The headband type coil has a function to suppress the leak of magnetic flux to the fringing region. In the case of S-LSR, the field clamp plate bears the role suppressing the leakage of the fringing field, instead of the coil. The 2D field calculation of the longitudinal cross section structure at the pole end is performed under the transverse symmetry. This 2D calculation is important process to decide the effective length of the bending magnet. The effective length is defined by

$$L_{eff}(s) = \int_{-\infty}^{\infty} B_y(s)/B_0 \, ds \, .$$

where s is the coordinate along the reference orbit of the beam. This integration is applied thorough the region far enough from the pole end where the fringing field becomes negligible. The effective length corresponds to the normalized value of total bending magnetic field on the reference orbit by the central bending field strength B_0. The total bending magnetic field for various excitation levels can be obtained by multiplying the central field strength and the effective length, as long as the saturation is negligible. For a

high excitation current, the influence of saturation arises. From the reason explained in section 3.1.2, the field strength reduces near the longitudinal pole end i.e. around the beam entrance and the exit. Since the area where the bending field exists is also changes, it may induce closed orbit distortion. In order to avoid this problem, the longitudinal pole end also has to be cut, as well as Fig 3-9. In the case of S-LSR, the longitudinal pole end cut is Rogowski's curve approximated by steps (Fig. 3-11). The effective length was adjusted by shifting the starting point of the Rogowski cut, so as to agree the actual pole length. The layout of the pole, coil and field clamp in the 2D field calculation is shown in Fig. 3-12.

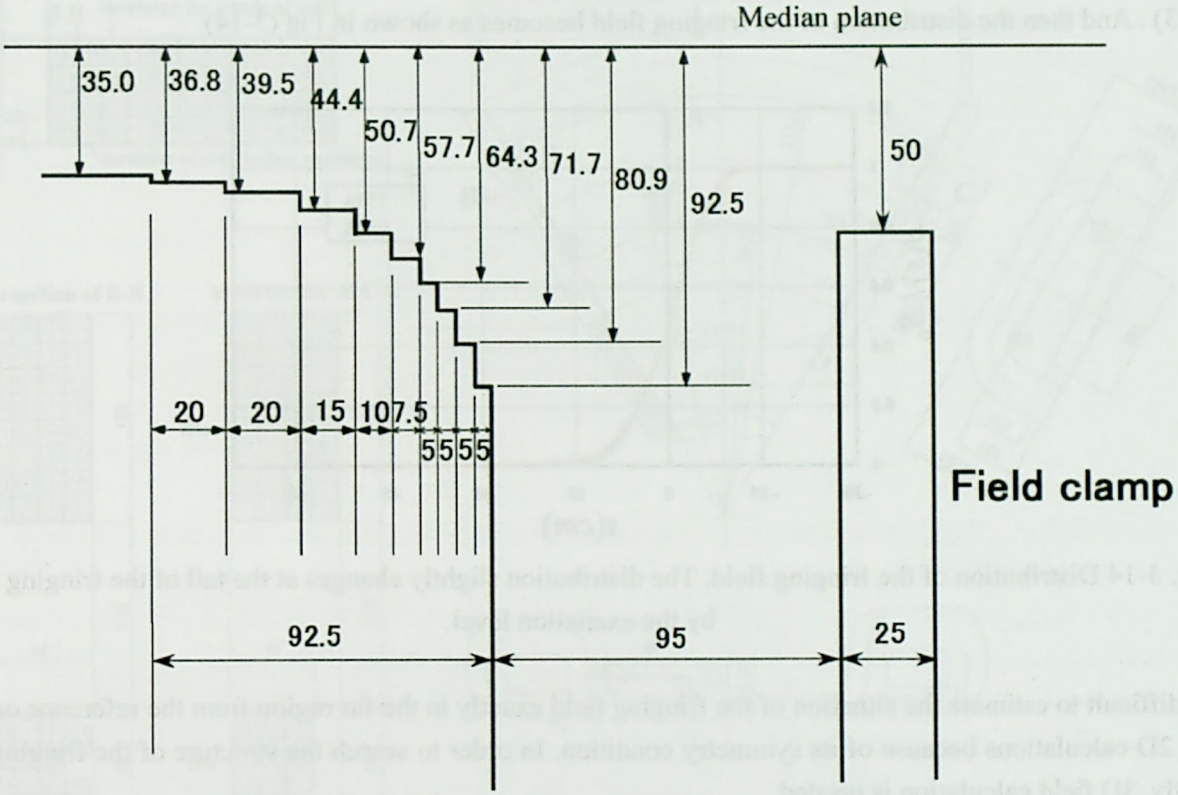

Fig. 3-11. Rogowski's curve approximated by steps

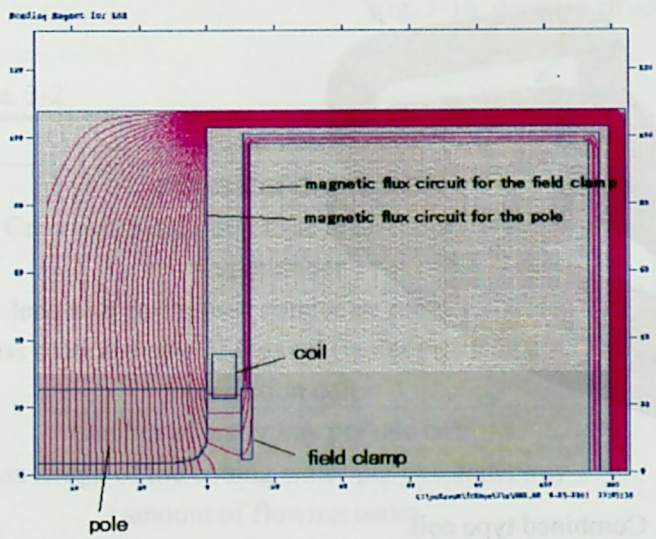

Fig. 3-12. The layout of the pole, coil and field clamp in the 2D calculation.

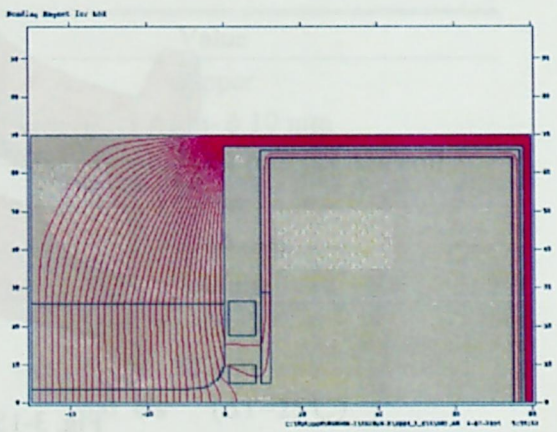

Fig. 3-13. The magnetic flux when the combined type coil is introduced.

In this calculation, materials which have infinite permeability are attached on the field clamp and the pole to ensure the magnetic flux circuit. Such 2D field calculation method is good approximation, near the reference orbit, it is proved by comparing with the measured field in section 3.9.5.

Although the reason that the head bend type coil has not been adopted is due to the problem of space between the quadrupole magnet, the coil shown in Fig. (3-15) can be applied. This coil is the combination of the head band type and the saddle type. This coil can suppress the spread of the fringing field, rather than the saddle type. Finally, this type of coil is adopted for S-LSR, although the fabrication process becomes complex. The magnetic flux in the fringing region when the combined type coil is applied is shown in Fig (3-13) . And then the distribution of the fringing field becomes as shown in Fig (3-14).

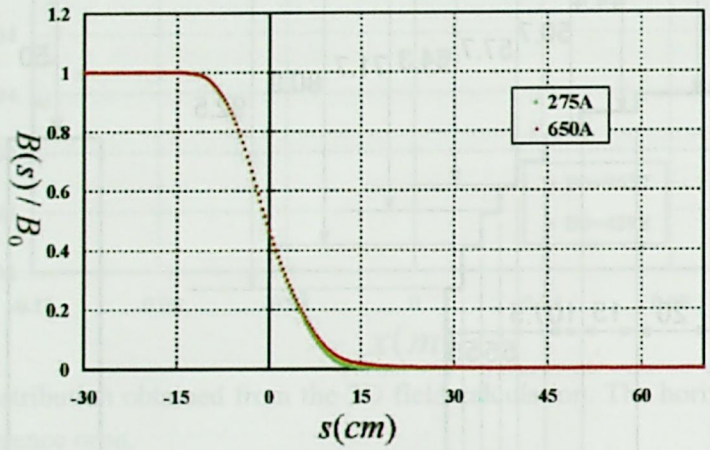

Fig. 3-14 Distribution of the fringing field. The distribution slightly changes at the tail of the fringing field by the excitation level.

It is difficult to estimate the situation of the fringing field exactly in the far region from the reference orbit by such 2D calculations because of its symmetry condition. In order to search the structure of the fringing field exactly, 3D field calculation is needed.

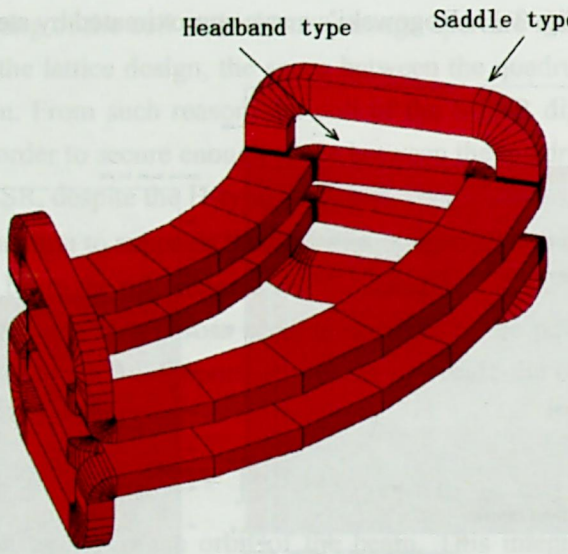

Fig. 3-15. Combined type coil

The coil is constructed with bundling a hollow conductor. The material of the hollow conductor is copper without oxygen, and the structure is a long hollow wire. By taking into account the balance between the presser drop of the cooling water and current density, the diameter of the hollow conductor is decided to be a

square of the size □14×14 mm, with the hole for cooling water of the diameter of ϕ 10 mm. Then the required turn number and the maximum excitation current become 650A and 44 turn per one coil, respectively. The detailed parameters of the coil are shown in Table 3-2. The difference of the field strength results from the gap size error is corrected by bypass circuit of the main power supply. Thus, the bending magnet of S-LSR has no correction coil.

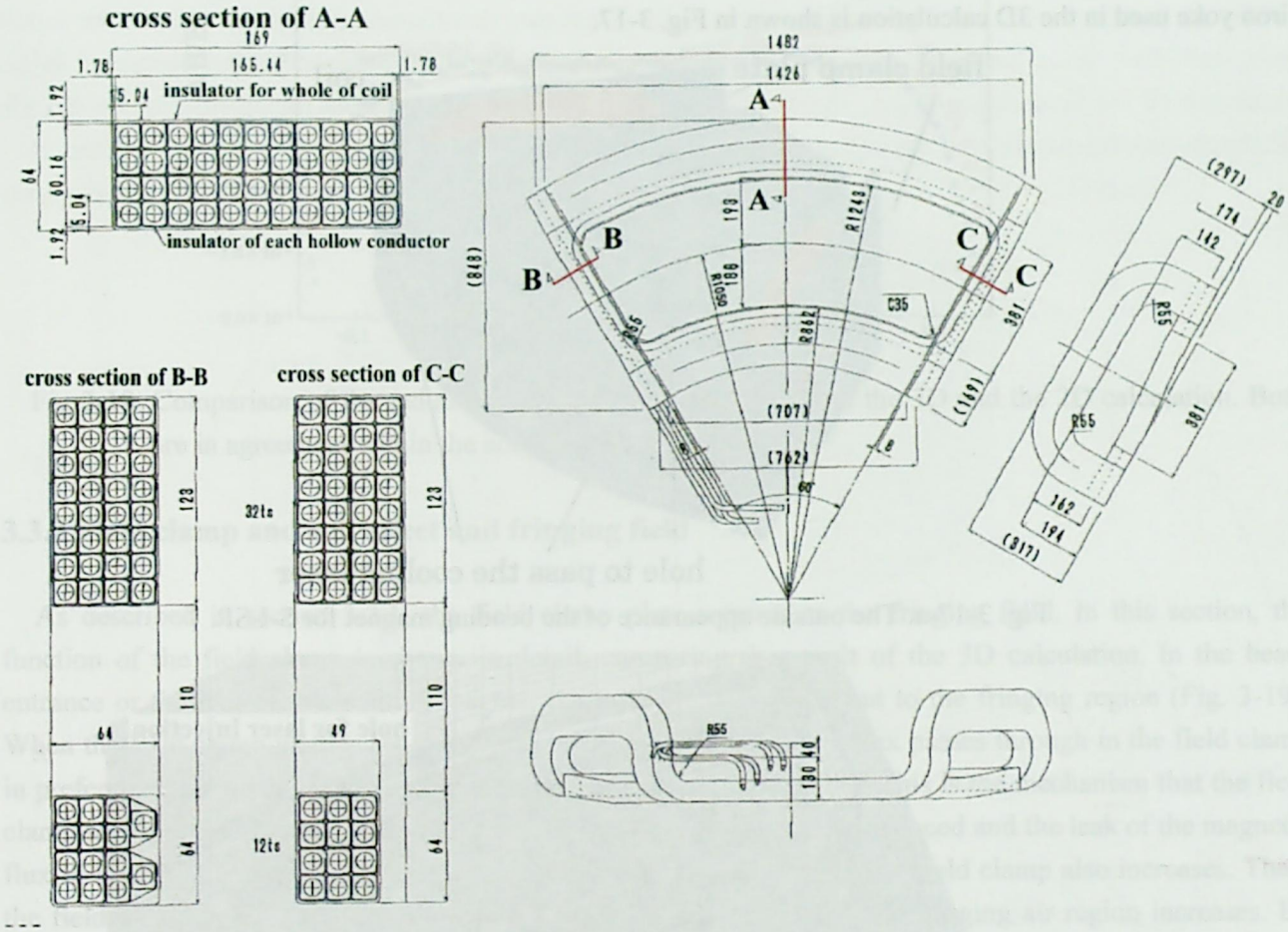

Fig. 3-16. detailed structure of the coil

Table. 3-2

Parameter	Value
material of the coil	copper
Cross sectional size of the hollow conductor	□14 mm-ϕ 10 mm
turn number	4-layer, 11-line, 44 turn per one coil
length of the hollow conductor per one coil	3.89m
cross sectional size of the coil (including insulator)	169×64 mm
correction coil	Nothing
number of waterway per one coil	2
pass length of the cooing water per one waterway	85.6 m
amount of flowing water	5.0 ℓ/s (ΔT=25℃)
pressure depression per one water way	2.0 kg·weight/cm^2
resistance of the coil per one magnet	5.9×10^{-2} Ω (60℃)
maximum excitation voltage per one magnet	38.4 V (60℃)

3.3 3D field calculation by TOSCA

3.3.1 Field distribution

The purpose of the 3D field calculation is to check the result of the 2D calculation, under the more realistic situation. Especially, the structure of the fringe field is investigated precisely. The upper half of the iron yoke used in the 3D calculation is shown in Fig. 3-17.

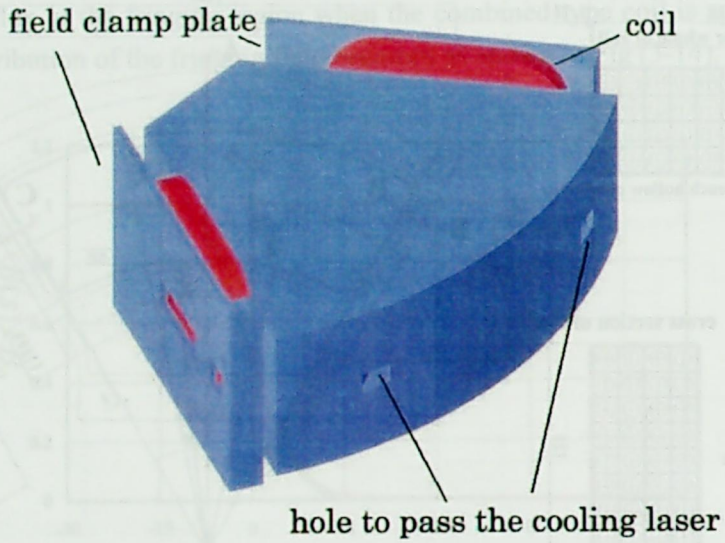

Fig. 3-17-a. The outside appearance of the bending magnet for S-LSR

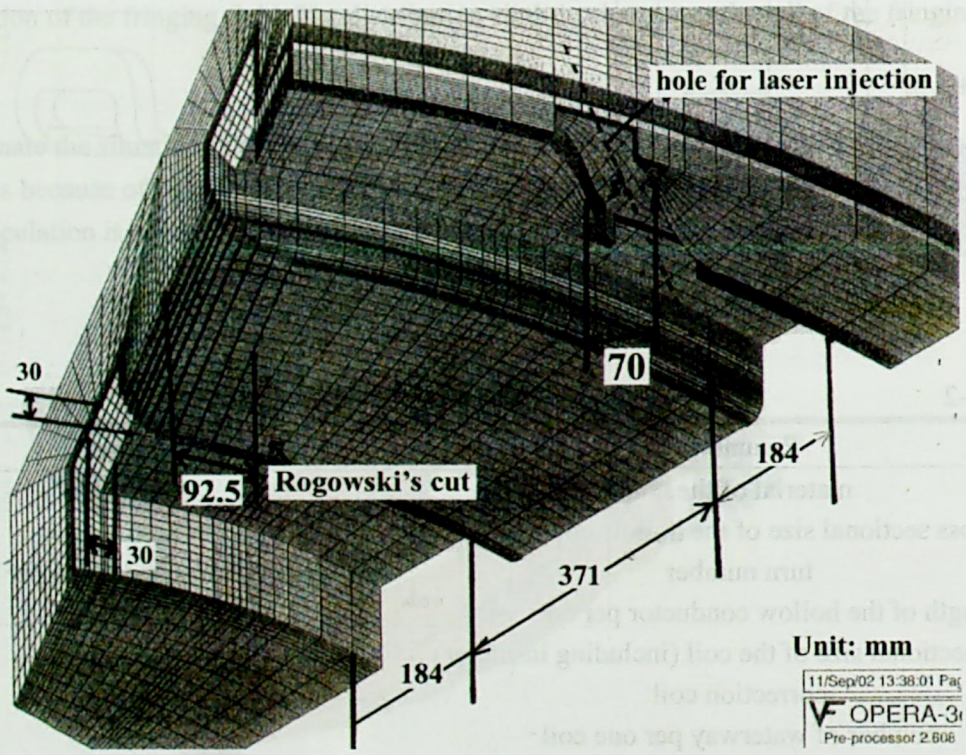

Fig 3-17-b. The pole surface structure.

Two through holes are made in the outer return yoke to pass the cooling laser. Therefore, the area of the outer return yoke becomes slightly narrower compared to the 2D calculation. The radial field distribution obtained from the 3D calculation is shown in Fig. 3-18. The field distribution coincides with that of the 2D

calculation within the accuracy of 0.5×10^{-4}.

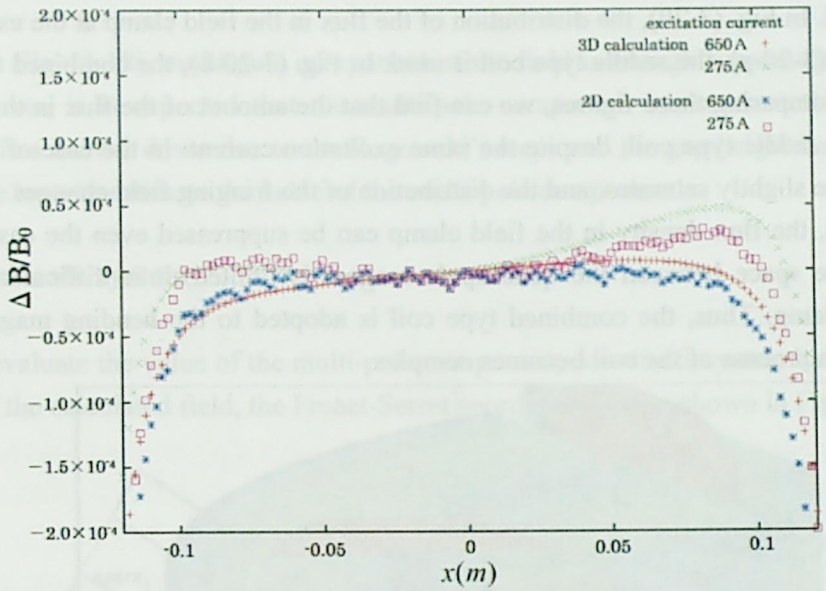

Fig 3-18. Comparison of the radial field distribution, obtained from the 3D and the 2D calculation. Both are in agreement within the accuracy of $\pm0.5\times10^{-4}$

3.3.2 Field clamp and coil effect and fringing field

As described in section 3.2.1, the field clamp plate suppresses the fringing field. In this section, the function of the field clamp is shown in detail, comparing the result of the 3D calculation. In the beam entrance or the exit of the bending magnet, the magnetic flux leaks out to the fringing region (Fig. 3-19). When the field clamp plate is set to the fringing region, the magnetic flux passes through in the field clamp in preference to the fringing air region because of its high permeability. This is the mechanism that the field clamp suppresses the fringing field. However, if the excitation level is enhanced and the leak of the magnetic flux to the fringing region increases, the amount of the flux flowing to the field clamp also increases. Then, the field clamp is saturated, and the ratio of the flux passing through the fringing air region increases. By such reason, the distribution of the fringing field changes, even if the pole end of the magnet is cut in Rogowski's curve.

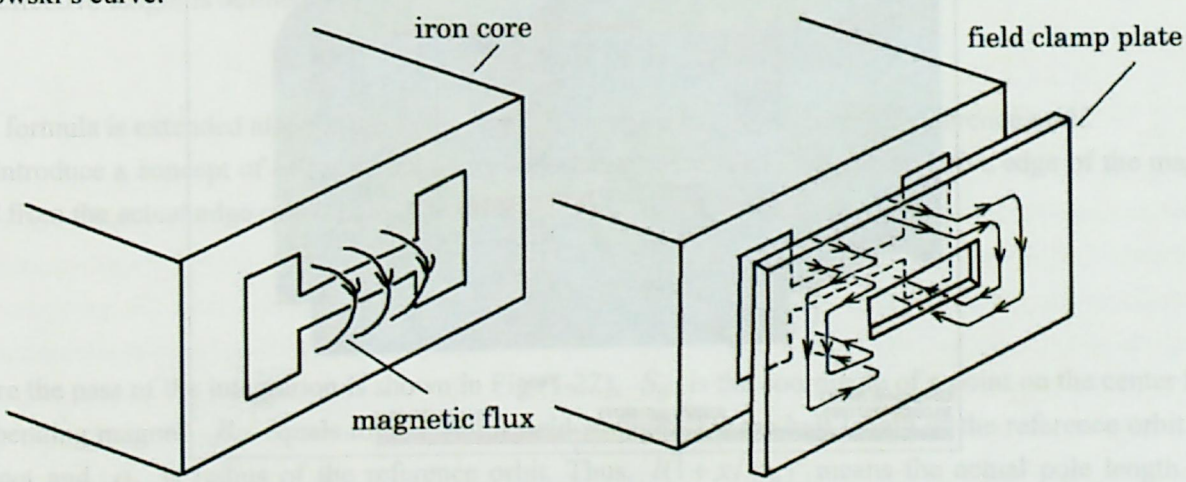

Fig 3-19. conceptual illustration of the function of the field clamp plate

To ensure the enough volume of the field clamp and to avoid the saturation is needed, in order to avoid

this matter. In addition to this device, effect of the coil is also important. In the 3D field calculation, two types of coil were tested. In Fig. (3-20), the distribution of the flux in the field clamp at the excitation current 650 A is shown. In Fig. (3-20-a), the saddle type coil is used. In Fig. (3-20-b), the combined type coil shown in Fig. (3-15) is used. Comparing these figures, we can find that the amount of the flux in the field clamp is larger in the case of the saddle type coil, despite the same excitation current. In the case of the saddle type coil, the field clamp plate slightly saturates, and the distribution of the fringing field changes. If the thickness of the plate is increased, the flux density in the field clamp can be suppressed even the case of the saddle type coil. But, since the space between the quadrupole magnet is limited, it is difficult to adopt larger thickness of the field clamp. Thus, the combined type coil is adopted to the bending magnet for S-LSR, although the construction process of the coil becomes complex.

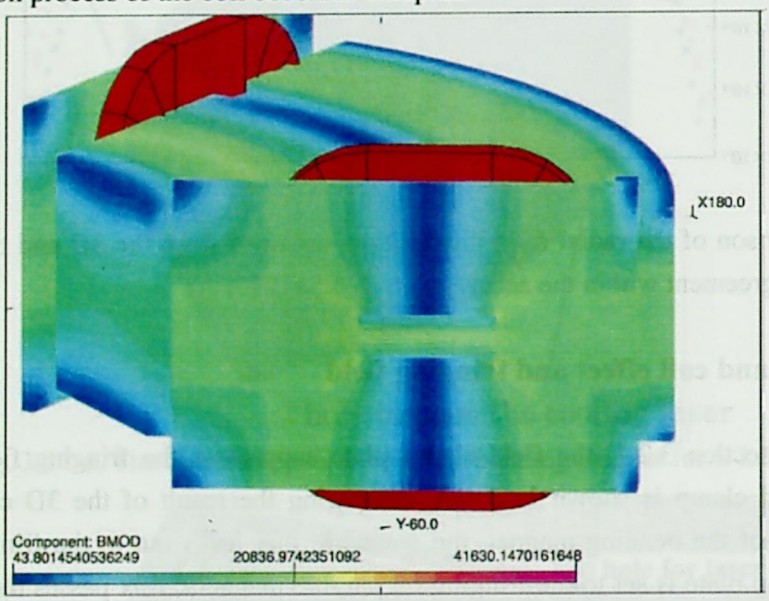

Fig 3-20-a. The distribution of the magnetic flux in the field clamp and the iron yoke. In this case saddle type coil is used with the excitation current 650A.

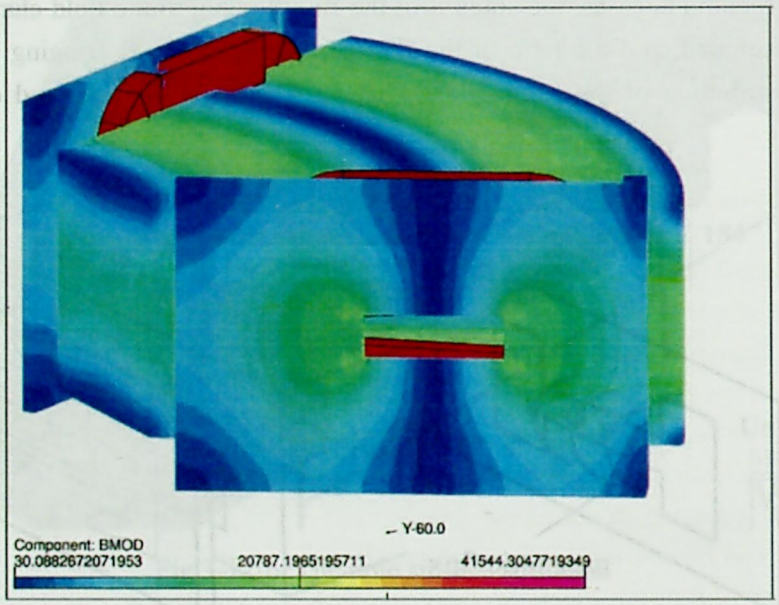

Fig 3-20-b. The distribution of the magnetic flux in the field clamp and the iron yoke. In this case combined type coil is used with the excitation current 650A. The amount of the magnetic flux in the field clamp is suppressed compared to Fig 3-20-a.

3.3.3 Multi-pole component of the calculated field

As shown in Fig. (3-18), multi-pole component of the field is enough suppressed at enough inner side of the gap. However, it is expected that the multi-pole component increases at the longitudinal pole end, because the shims are cut down due to the Rogowski's steps and the gap height becomes higher due to this steps. Thus, we have to estimate the value of the multi-pole component.

3.3.3.1. Coordinate system

In order to evaluate the value of the multi-pole component, coordinate system has to be defined exactly. In the analysis of the calculated field, the Frenet-Serret coordinate system shown in Fig (3-21) is used.

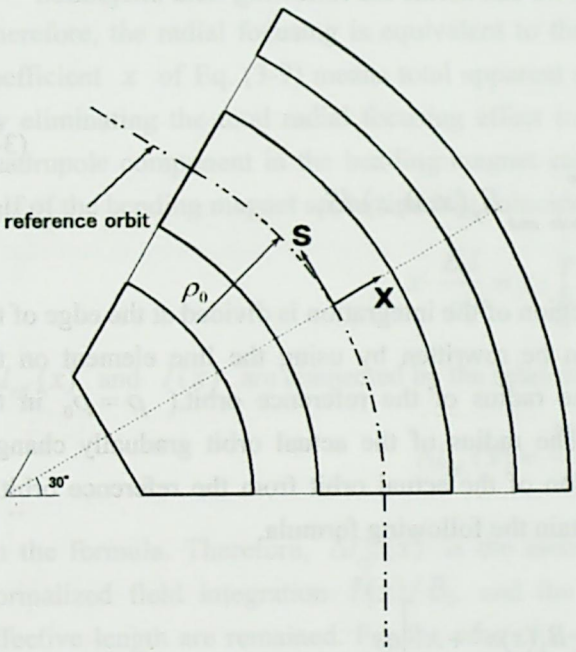

Fig. 3-21. Coordinate system.

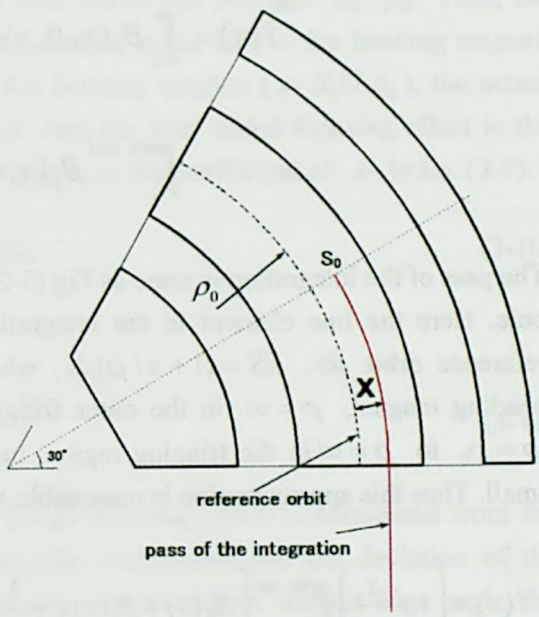

Fig 3-22. Pass of the integration of the field

The effective length is defined by [3-2]

$$L_{eff}(x) = \int_{-\infty}^{\infty} B_y(x, 0, s) / B_0 \, ds . \tag{3-5}$$

This formula is extended also for the orbits which have the other radius than the reference orbit.
We introduce a concept of effective boundary to indicate the deviation of the effective edge of the magnetic field from the actual edge of the pole. The effective boundary is defined by

$$\Delta l_{eff}(x) = \int_{S_0}^{\infty} B_y(x, 0, s) / B_0 \, ds - l\left(1 + \frac{x}{\rho_0}\right) \tag{3-6}$$

where the pass of the integration is shown in Fig (3-22), S_0 is the coordinate of a point on the center line of the bending magnet, B_0 equals to the central field strength, l is the half length of the reference orbit in the magnet and ρ_0 is radius of the reference orbit. Thus, $l(1+x/\rho_0)$ means the actual pole length at the orbit radius $\rho_0 + x$. Therefore, the effective boundary means the deviation of the effective length from the actual pole length in each orbit radius.

We can obtain the information about the multi-pole component from the effective boundary. The method to obtain the multi-pole component is shown in next section.

3.3.3.2. Evaluation of the multi-pole component

We suppose a simple model in order to assess the effective boundary. The expansion of the field distribution of a bending magnet on the median plane up to third-order can be expressed as [3-3]

$$B_y(x, 0, s) = B_0 + B_1 x + \frac{1}{2!}B_2 x^2 + \frac{1}{3!}B_3 x^3 + \ldots = \sum_{n=0}^{\infty} \frac{B_n}{n!} x^n, \tag{3-7}$$

where B_n $(n \geq 1)$ denotes the coefficient of the multi pole component. The field of an actual bending magnet has s dependence everywhere; $B_n = B_n(s)$. Then we can define the following field integration

$$\begin{aligned} I(x) &= \int_{S_0}^{\infty} B_y(x, 0, s) dS \\ &= \int_{S_0}^{pole\ end} B_y(x, 0, s) dS + \int_{pole\ end}^{\infty} B_y(x, 0, s) dS. \end{aligned} \tag{3-8}$$

The pass of the integration is same as Fig (3-22), but the region of the integration is divided at the edge of the pole. Here the line element in the integration (dS) can be rewritten by using the line element on the reference orbit ds; $dS = (1 + x/\rho)ds$, where ρ is the radius of the reference orbit.($\rho = \rho_0$ in the bending magnet, $\rho = \infty$ in the outer fringing region. The radius of the actual orbit gradually changes $\rho = \rho_0$ to $\rho = \infty$ in the fringing region, but the deviation of the actual orbit from the reference orbit is small. Thus this approximation is reasonable.) Then we obtain the following formula.

$$\begin{aligned} I(x) = &\left(1 + \frac{x}{\rho_0}\right) \int_{S_0}^{pole\ end} \left[B_0(s) + B_1(s)x + \frac{1}{2!}B_2(s)x^2 + \frac{1}{3!}B_3(s)x^3 + \ldots \right] ds \\ &+ \int_{pole\ end}^{\infty} \left[B_0(s) + B_1(s)x + \frac{1}{2!}B_2(s)x^2 + \frac{1}{3!}B_3(s)x^3 + \ldots \right] ds \\ = &\int_{S_0}^{\infty} B_0(s) ds + x \cdot \left[\int_{S_0}^{pole\ end} \frac{1}{\rho_0} B_0(s) ds + \int_{S_0}^{\infty} B_1(s) ds \right] + x^2 \cdot \left[\int_{S_0}^{pole\ end} \frac{1}{\rho_0} B_1(s) ds + \int_{S_0}^{\infty} \frac{1}{2!} B_2(s) ds \right] + \ldots \end{aligned} \tag{3-9}$$

By this process, the integration pass has been summarized only to the reference orbit. We can find that each coefficient of x is not merely the component of magnetic field of its order. The lower order component in the bending magnet is mixed in each coefficient. We can also find that the field integration $I(x)$ correspond to the apparent magnetic field which is felt by the beam. In a flat pole bending magnet, the dipole component behaves as if it is the quadrupole component. In the flat pole bending magnet a beam is focused horizontally by the radial focusing effect, even if there is no quadrupole component. The apparent radial focusing field generated by the dipole component corresponds to the first term in the coefficient of x in Eq. (3-9). Similarly, the quadrupole component in a bending magnet behaves as a sextupole component in a formula of the horizontal chromaticity of the bending magnet. The apparent sextupole component

corresponds to the first term in the coefficient of x^2 in Eq. (3-9). These apparent effects arise due to the finite curvature of the beam orbit. When the bending radius ρ_0 is large, these effects are negligible. (Actually, in Eq. (3-9), if ρ_0 is set to ∞ the mixing of the magnetic field components vanishes.)
Next, we consider the relation between the effective boundary $\Delta l_{eff}(x)$ and the field integration $I(x)$. The equation of motion of the reference particle in the flat pole bending magnet is given by

$$\frac{d^2x}{ds^2} = -\frac{1}{\rho_0^2}\cdot x .$$

The equation of motion for the same reference particle in a quadrupole magnet is given by

$$\frac{d^2x}{ds^2} = -\frac{B_1}{B_0\rho_0}\cdot x$$

Therefore, the radial focusing is equivalent to the quadrupole field which has strength B_0/ρ_0. Thus, the coefficient x of Eq. (3-9) means total apparent quadrupole component in the half of the bending magnet. By eliminating the total radial focusing effect in the half of the bending magnet ($x\cdot B_0 l/\rho_0$), the actual quadrupole component in the bending magnet can be extracted. And the total radial focusing effect in the half of the bending magnet approximately coincides with the first term in the coefficient of x in Eq. (3-9).

$$x\cdot\frac{B_0 l}{\rho_0} \approx x\cdot\int_{s_0}^{pole\ end}\frac{1}{\rho_0}B(s)ds \tag{3-10}$$

$\Delta l_{eff}(x)$ and $I(x)$ are connected by the relation

$$\Delta l_{eff}(x) \approx \frac{I(x)}{B_0} - l\left(1+\frac{x}{\rho_0}\right) \tag{3-11}$$

on the formula. Therefore, $\Delta l_{eff}(x)$ is the amount that the radial focusing effect is eliminated from the normalized field integration $I(x)/B_0$ and the actual quadrupole component and the deviation of the effective length are remained. For the case of S-LSR or a flat pole dipole magnet without edge angle, the quadrupole component is strongly suppressed in the inner gap. Therefore, the coefficient of x^2 in Eq. (3-9) is almost the total sextupole component of the bending magnet. When the multi-pole components are enough suppressed in the inner gap, the effective boundary can be expressed approximately by

$$\Delta l_{eff}(x) \approx \frac{1}{B_0}\left(\left[\int_{s_0}^{\infty}B_0(s)ds - B_0 l\right] + x\cdot\int_{s_0}^{\infty}B_1(s)ds + x^2\cdot\int_{fringe}\frac{1}{2!}B_2(s)ds + x^3\cdot\int_{fringe}\frac{1}{3!}B_3(s)ds + \ldots\right). \tag{3-12}$$

This means that the first term of the expansion ($\Delta l_{eff}(0)$) represents the difference between the half effective length and the half actual pole length on the reference orbit, and the coefficients of the higher order terms represents the $B_n L$ product in the half region of the magnet. Therefore, by expanding the effective boundary around the reference orbit ($x=0$) the information of the multi-pole component is obtained approximately.

The effective boundary obtained from the 3D field calculation using the iron core of Fig. (3-17) and the coil (Fig. 3-16) is shown, at the high excitation current 650A and the low excitation current 275A. (Fig. 3-23)

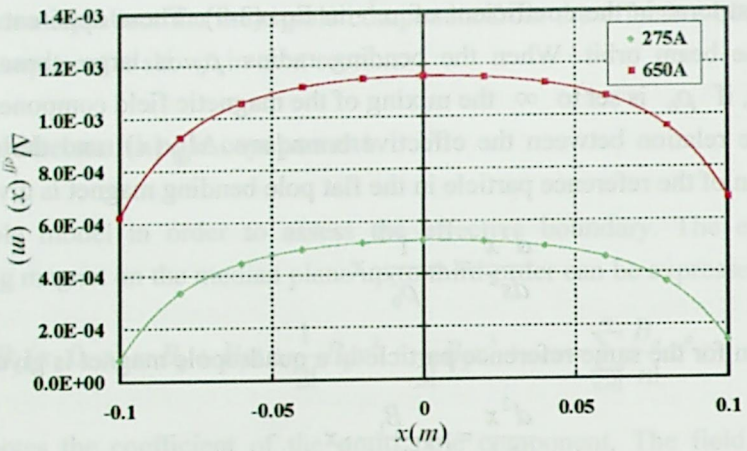

Fig. 3-23. Effective boundary obtained from the 3D field calculation based on the iron core shown in fig. (3-17). The effective lengths of each excitation level are slightly longer than the actual pole length.

From Fig. 3-23, we can find that the effective boundary slightly changes by the excitation current despite the Rogowski's cut is applied to the longitudinal pole end. It is thought to be induced by the saturation of the field clamp, rather than the saturation of the pole end. The effective length near the reference orbit is longer than that of the end of the usable aperture (± 0.1 m). This means that the sextupole component is included in the effective boundary. When the effective boundary is expanded as

$$\Delta l_{eff}(x) = b_0 + b_1 x + b_2 x^2 + \ldots, \tag{3-13}$$

these coefficients becomes as shown in table 3-3.

3.3.3.3. Suppression of the multi-pole component

The cause of the sextupole component is the longer effective length near the reference orbit. Therefore, if the actual pole length is slightly shortened near the reference orbit, the difference of the effective length depending on the radial position may be reduced. At the same time, the sextupole component is suppressed. In order to realize this situation, we cut down the last two steps of the Rogowski's cut, as shown in Fig. 3-24.

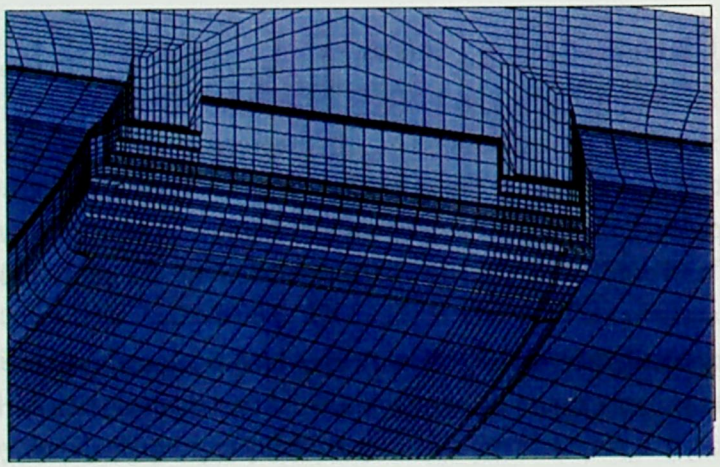

Fig. 3-24-a. Pole end structure to suppress the sextupole component. The last two steps of the Rogowski's cut are cut down.

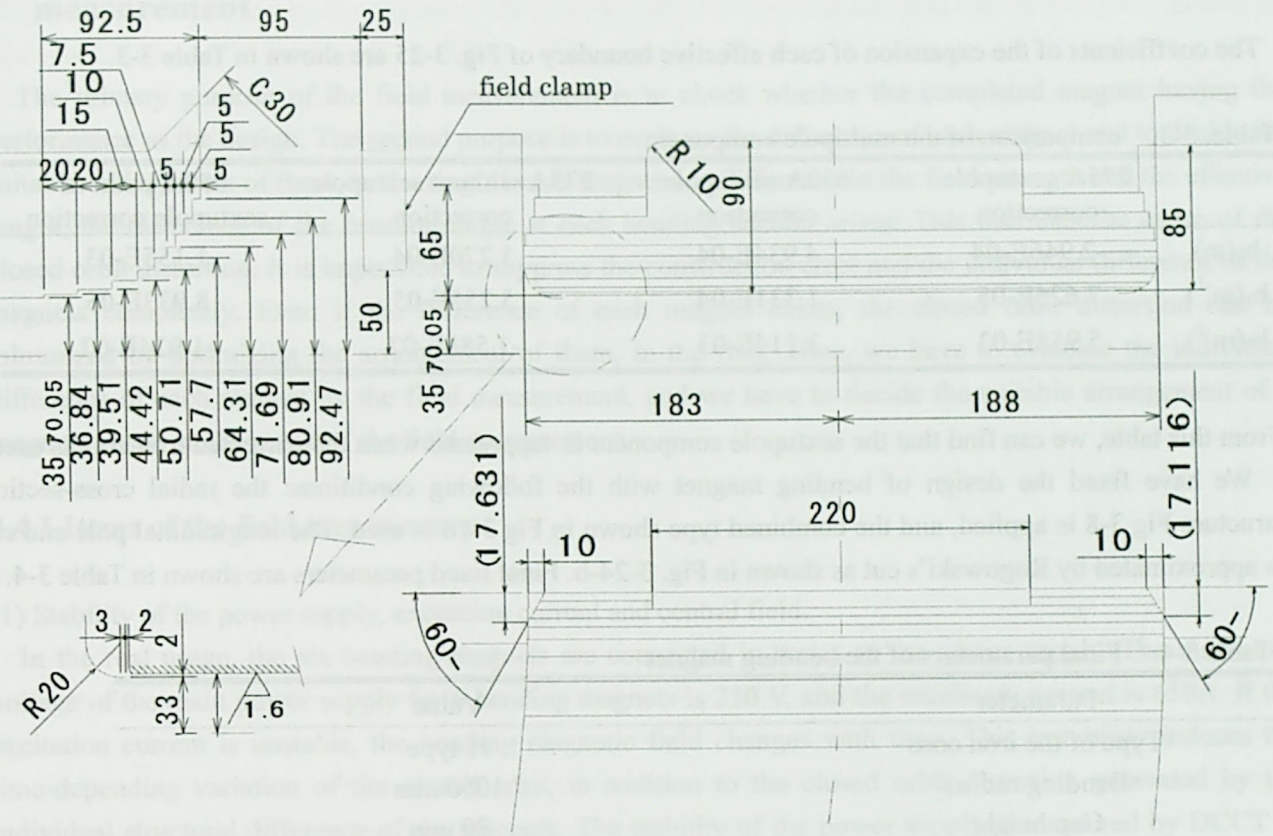

Fig. 3-24-b. detailed dimensions of the pole end cut.

By this way, the actual pole length near the reference orbit is shortened. The result of the 3D field calculation using the iron core (Fig. 3-24) and the combined type coil (Fig 3-16) is shown in Fig 3-25, comparing the result of the previous field calculation.

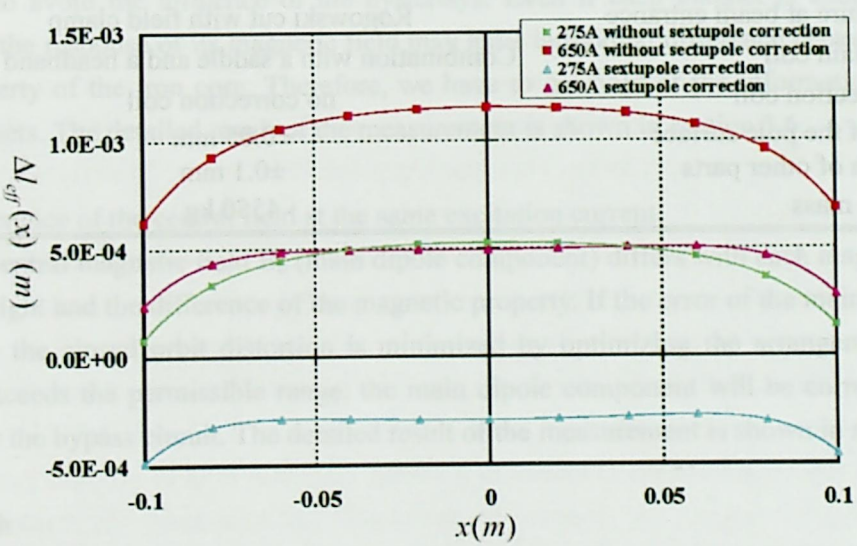

Fig. 3-25. Comparison of the effective boundary. When the iron core which is shown in Fig. 3-24-a is used, the radial difference of the effective boundary is reduced.

3.3.3.4. Evaluation of the multi-pole component

The coefficients of the expansion of each effective boundary of Fig. 3-25 are shown in Table 3-3.

Table. 3-3. comparison of the multipole component

	275A sextupole correction	650A sextupole correction	275A without sextupole correction	650A without sextupole correction
b_0(m)	-2.946E-04	4.934E-04	5.270E-04	1.155E-03
b_1(m^{-1})	7.626E-05	1.331E-04	5.255E-05	8.933E-05
b_2(m^{-2})	5.958E-03	3.114E-03	-1.588E-02	-1.924E-02

From this table, we can find that the sextupole component is suppressed when the corrected iron core is used.

We have fixed the design of bending magnet with the following conditions: the radial cross-section structure Fig 3-8 is applied, and the combined type shown in Fig 3-16 is used. The longitudinal pole end cut is approximated by Rogowski's cut as shown in Fig. 3-24-b. Final fixed parameters are shown in Table 3-4.

Table 3-4. Final parameters of the bending magnet

Parameter	Value
Type of the iron core	H-type
Bending radius	1050 mm
Gap height	70 mm
Pole width	371 mm
Bending angle	60°
Edge angle	0°
Maximum excitation current	57200 A·T
Coil number per one magnet	2
turn number of the coil	44 turn per one coil
Pole end structure at beam entrance	Rogowski cut with field clamp
main coil	Combination with a saddle and a headband type
correction coil	no correction coil
precision of the pole surface	±0.05 mm
precision of other parts	±0.1 mm
mass	4550 kg

3.4 Outline of performance assessment of the bending magnets by field measurement

The primary purpose of the field measurement is to check whether the completed magnet having the performance as the design. The second purpose is to evaluate the difference of each magnet and to decide the suitable arrangement of them, in the ring. If each magnet has difference in the field strength and the effective length, the difference of the bending angle at each bending section arises. This becomes the cause of the closed orbit distortion. It is impossible to suppress the construction error and the individual difference of the magnets completely. Even if the difference of each magnet exists, the closed orbit distortion can be minimized by optimizing the arrangement of them, in the ring. Thus, we have to evaluate the individual difference of each magnet by the field measurement, and we have to decide the suitable arrangement of 6 magnets based on the result of the field measurement.

3.4.1 Items of the field measurement

(1) Stability of the power supply, excitation current and central field.

In the real usage, the six bending magnets are connected in series to the power supply. The maximum voltage of the main power supply for 6 bending magnets is 250 V, and the maximum current is 650A. If the excitation current is unstable, the bending magnetic field changes with time. This instability induces the time-depending variation of the closed orbit, in addition to the closed orbit distortion generated by the individual structural difference of the magnets. The stability of the power supply is measured by DCCT in the state that the power supply is connected to a single bending magnet for the field measurement. The detailed result of the measurement is shown in section 3.5.

(2) Excitation property of each bending magnet

The excitation level of the bending magnets is set up to the target value after initialization excitation process, in order to avoid the influence of the hysterisys. Even if each magnet is excited with the same excitation pattern, the response of its magnetic field may have individual difference because of difference of the magnetic property of the iron core. Therefore, we have to get hold of the information of all excitation property of 6 magnets. The detailed result of the measurement is shown in section 3.6.

(3) Individual difference of the central field at the same excitation current.

In general, the central magnetic field B_0 (main dipole component) differs with each magnet because of the error of the gap height and the difference of the magnetic property. If the error of the main dipole component is tolerable range, the closed orbit distortion is minimized by optimizing the arrangement of 6 magnets. When the error exceeds the permissible range, the main dipole component will be corrected by correction current induced by the bypass circuit. The detailed result of the measurement is shown in section 3.7.

(4) Effective length

The effective length implies the effective region where the bending magnetic field exists. The individual difference of the effective length induces closed orbit distortion along the reference orbit.

The detailed instruments and methods of the measurement are shown in section 3.4.2, and the results are shown in Section 3.9.

(5) Field distribution

Ideally, the flat pole bending magnet has no higher order field component. However, the actual fabricated magnet usually has a sextupole component due to the finite width of the pole and a small quadrupole component due to the construction error. The sextupole component of the bending magnet induces resonances around at a certain operating point and beam instability may happen. The error of the quadrupole component generates the "stop band" near integer or half integer tune values. In general, the effect to the integer or half integer stop band is smaller than that of the error of the quadrupole magnets. We confirm the degree of the quadrupole component error of the bending magnet by the field measurement. The higher-order component included in the bending magnetic field induces resonances, and a kind of stop band is created around the resonance line in the tune diagram [3-4] [3-5]. Therefore, we also have to investigate the degree of existence of the higher-order component.

The detailed instruments and methods of the measurement are shown in section 3.4.2, and the results are shown in Section 3.9, together with the measurement of the effective length.

3.4.2 Main instruments for the field measurement

(1) Power supply

The power supply converts a three phase alternating current (210 V ±10% 50/60 Hz) to a direct current. The maximum specification of the power supply is 200 kW. The assumed resistance of the power supply is 0.354 Ω, which corresponds to the total resistance of the six bending magnets plus the wiring resistance. The maximum current and voltage is 650 A and 250V, respectively. The current stability is ±50 ppm per 4 hour, at the maximum current. The ratio of the ripple to the maximum current is less than 50 ppm.

(2) Current meter

The excitation current was measured by DCCT which is inserted in the internal circuit of the power supply.

(3) NMR

When a nuclear magnetic moment associated with a nuclear spin is placed in an external magnetic field, the different spin states are given different magnetic potential energies. In the presence of the static magnetic field which produces a small amount of spin polarization, a radio frequency signal of the proper frequency can induce a transition between spin states. This spin flip places some of the spins in their higher energy state. If the radio frequency signal is then switched off, the relaxation of the spins back to the lower state produces a measurable amount of RF signal at the resonant frequency associated with the spin flip. This process is called Nuclear Magnetic Resonance (NMR). The precession of the proton spin in the magnetic field is the interaction which is used in proton NMR. The proton spin will tend to precess around the magnetic field with a frequency traditionally called the Larmor frequency. The Larmor frequency is proportional to strength of the magnetic field. For a 1 T magnetic field this Larmor frequency is 42.5781 MHz. As a probe, a sample containing protons (hydrogen nuclei) is placed in a strong magnetic field to produce partial polarization of the protons. A strong RF field is also imposed on the sample to excite some of the nuclear spins into their higher energy state. When this strong RF signal is switched off, the spins tend to return to their lower state, producing a small amount of radiation at the Larmor frequency associated with that field. The emission of radiation is associated with the spin relaxation of the protons from their excited state. It induces a radio frequency signal in a detector coil which is amplified to display the NMR signal.

The NMR magnetic field meter used in our field measurement was ECHO DENSHI, EFM-2000AX. The range of this NMR meter is 0.1~2 T, and the resolution is 0.1 μ T. The sample of the NMR probe is proton. The NMR probe was placed near the center of the pole. The NMR probe can measure the absolute value of the magnetic flux density. Since there is only dipole component at the center of the pole, we can regard the value measured by NMR as the central field (main dipole component) of the magnet; B_0.

(4) Hall probe

As a method of the measurement of effective length, a long flip coil measurement can be considered. However, this method is not feasible for a sector magnet with the small bending radius, and we want to investigate the detailed structure of the fringing field. Thus, we chose the field mapping method by a Hall-probe. The field was measured on the points of rectangular grids. By this way, field distribution in the bending magnet was measured.

The function of a Hall sensor is based on the physical principle of the Hall-effect. The Hall-effect is that a voltage is generated transversely to the current flow direction in an electric conductor (the Hall voltage), if a magnetic field is applied perpendicularly to the conductor. By reading out this voltage the magnetic file component perpendicular to the Hall-element is measured. The Hall-effect is most pronounced in semiconductors, and the most suitable Hall element is a small platelet made of semiconductive material.

There is various type of Hall probe [3-5]. Hall effect has temperature dependence. Thus the value measured by a Hall-probe has to be corrected with the temperature. Group3 Hall-probe performs this correction automatically and exactly. Therefore, we chose Group3 Hall-probe. The Group3 Hall-probe type-MPT-141 is connected to the tesla meter type-DTM-151. The measurable range of this Hall-tesla meter system is $\pm$3 T. The range is divided to 4 region; 0.3T, 0.6T, 1.2T, 3.0T, and the resolution in each range is 0.1μT, 1μT, 1μT, and 1μT, respectively. The accuracy is within $\pm$ (0.01% of reading + 0.006% of full scale) at 25°C. The sensor area of MPT-141 is shown in Fig. 3-26-a, it is enough small for mapping. Hall probe can measure only the field component perpendicular to the sensor surface. The main component of the field measurement is B_y. Therefore the angle of the installation becomes important. Calibration of the absolute value and the center of the sensor region were made as shown in section 3.8.

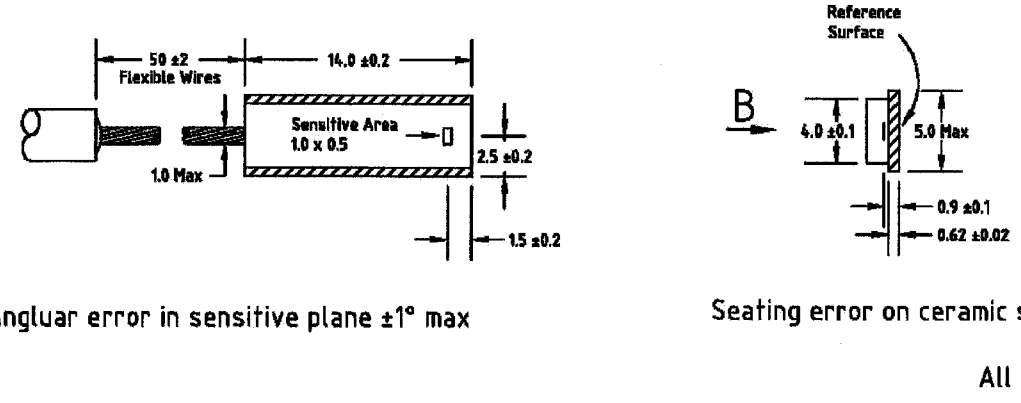

Fig 3-26-a. Structure of Group3 Hall-probe MPT-141

(5) 3 axis drive stage

The field mapping was performed, mounting the Hall-probe on a 3-axis drive stage. The drivable range of this stage is (1450×440×260 mm; longitudinal, transverse, and vertical, respectively.) The stage is driven

with the resolution of 5 μ m by three stepping motors. The stepping mother drivers are connected to TUJI DENSHI PM4C four-cannel pulse motor controller.

Three linear scales are equipped to each axis, in order to confirm that the motor system works well. The position linearity of the pulse motor system was checked by these scales. We found that the longitudinal axis has worst linearity, but the deviation is only 20 μ m which is accurate enough for our mapping purpose.

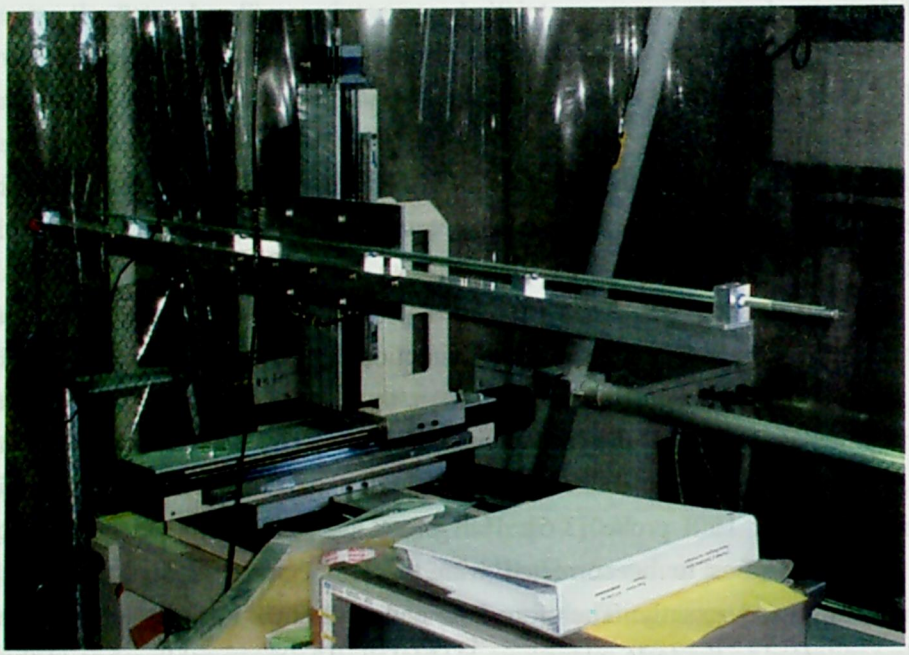

Fig 3-26-b. 3-axis drive stage used in the mapping measurement.

All instruments were controlled and read out by PC through a NI PCMCIA-GPIB card.

3.4.3 The precision of measurement

The manufacturing error of the gap height is estimated to 70 ± 0.05 mm. In order to investigate the effect of this error to the magnetic field, the precision of the NMR and the Group3 Hall probe is desirable to be within $\pm 1 \times 10^{-4}$. This precision is achieved in the nominal performance. However, in the actual use, various other factors to make the precision worse exist. For example, the oscillation of the Hall probe which is attached to the tip of the 3 axis drive stage is considered as the factor. As proven later, even with the other factors, the precision of the probes is enough. The manufacturing error of the pole length is estimated to be ± 0.1 mm. Therefore, the precision of the measured effective length is desirable to be within ± 0.1 mm.

3.5 Stability of the excitation current, the magnetic field and instruments

3.5.1 Surroundings of the measurement

The measurement had been performed at National Institute of Radiological Science. The bending magnet and the instruments had been surrounded by vinyl sheets to suppress the changes of the temperature and air flow.

3.5.2 Initialization pattern

Initialization of the excitation is needed to avoid the difference of the central magnetic field due to the hysterisys. The excitation pattern of the initialization is shown in Fig 3-27. Initially, the excitation current is raised linearly to the maximum value 650A during about 30 seconds. After maintaining the maximum excitation level for 10 seconds or 30 seconds (TOP time in Fig. 3-27), the excitation current is set up to the target value. After the central magnetic field settles down at the target value, the storage of the beam is to be started. We investigated the suitable TOP time and FALL time in Fig. 3-27. As the TOP time, we tested 10 seconds and 30 seconds. The time dependence of the central field is shown in Fig. 3-28. Each measurement was performed 3 times independently. In the both cases, the central fields are settled to the certain values after 800 seconds. The central field coincides with precision of 2×10^{-5} in the both cases. Finally, we chose the TOP time as 30 second, although the both cases were satisfactory.

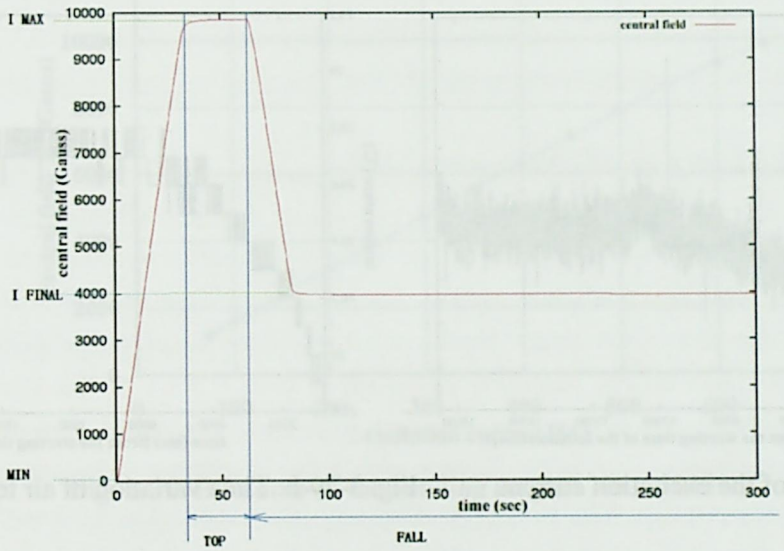

Fig 3-27. The excitation pattern of the initialization.

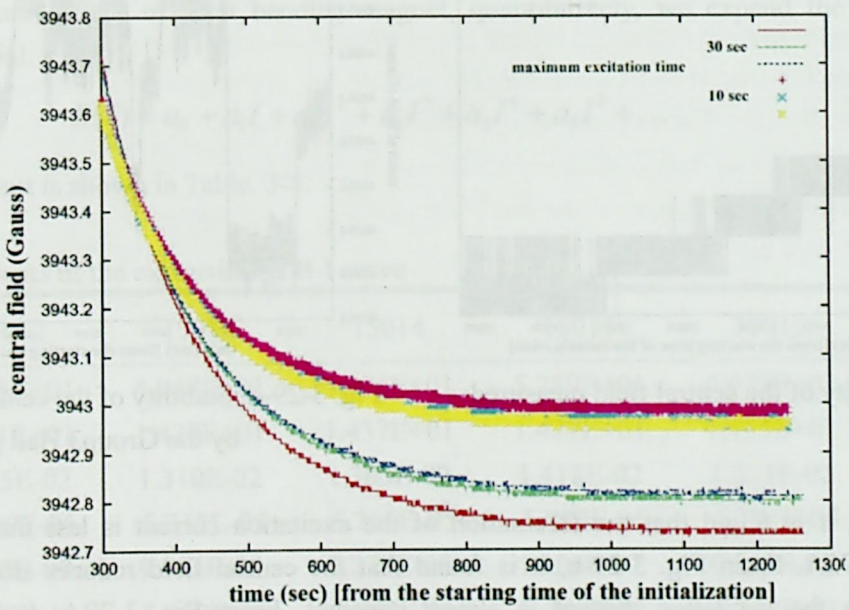

Fig 3-28. Time dependence of the central field

3.5.3 Long time stability of the central field, the excitation current and the instruments

As shown later, the mapping time per one measurement is about 4 hour. Therefore we have to investigate the long time stability of the instruments, the magnet and excitation current, prior to mapping measurement. The stability of the instruments during about 5 hour is shown in Figures 3-29-a-d together with the stability of the excitation current and the central field. These values are measured at the same time. Thus, they must correlate each other. For example, the NMR probe measures the absolute value of the magnetic flux density $|\vec{B}| = \sqrt{B_x^2 + B_y^2 + B_s^2}$ and the Group3 Hall probe measures the vertical component of the field B_y. In the median plane of the magnet the $\vec{B}$ has only B_y component. Thus the value of the Hall-probe can be calibrated with the NMR. Furthermore, the excitation current and the central field ($B_0 \approx |\vec{B}| \approx B_y$; at the center of the gap) are correlated by the relation Eq. (3-3). They have to be in proportion. Therefore, if the one of these values has large deviation from their correlations, its instrument or actual value is abnormal.

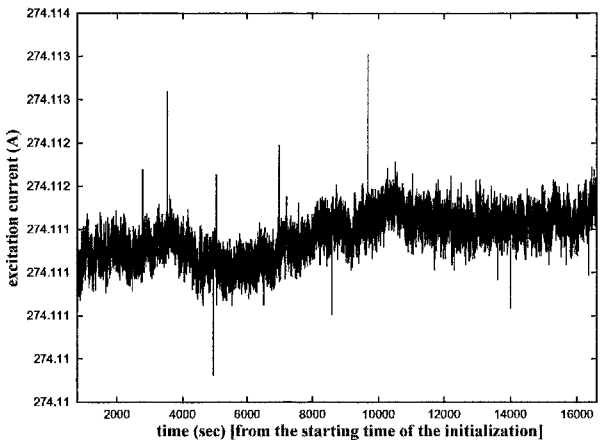

Fig. 3-29-a. Stability of the excitation current.

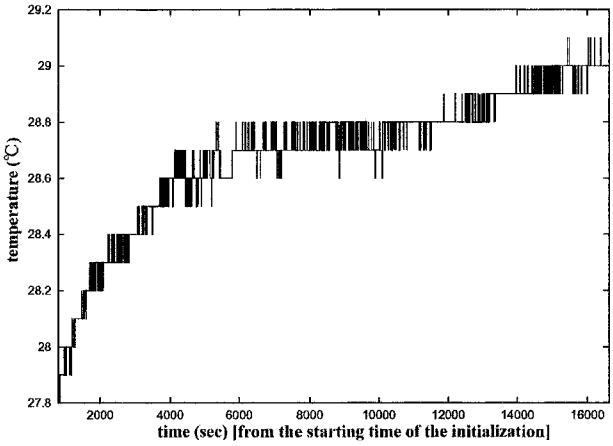

Fig. 3-29-b. Time variation of air temperature in the gap

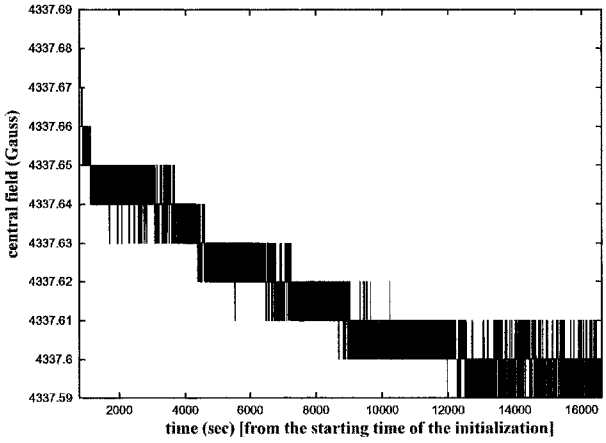

Fig. 3-29-c. Stability of the central field measured by the NMR.

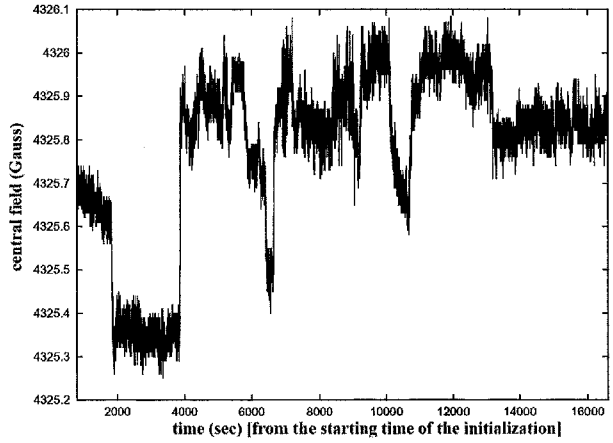

Fig. 3-29-d. Stability of the central field measured by the Group3 Hall probe.

From Fig. 3-29-a, it is found that the fluctuation of the excitation current is less than $\pm 5 \times 10^{-6}$ at the excitation level 275A. From Fig. 3-29-c, it is found that the central field reduces slowly (about 2×10^{-5} reduces), although the excitation current is almost constant. From Fig. 3-29-b, it is thought that the temperature of the iron core rises and then the gap height slightly increased. This is the cause that the central

field reduces slowly. The reduction of the central field is small enough compared with the target accuracy and the resolution of the Group3. As shown in Fig. 3-29-d, the measured value of Group3 Hall probe jumps suddenly. The value of this jump is less than $\pm 1 \times 10^{-4}$. This error is within the target accuracy of the measurement and within the specifications.

3.6 Excitation property of each bending magnet

The relation between the central field B_0 and the excitation current was investigated. The central field was measured by NMR after the initialization described in section 3.5.2. The excitation current was changed by 50 A steps, except for 75 A and 100 A. The initialization was performed for every excitation level. The fabricated bending magnets have been numbered from 15012 to 15017. The B-I curve of the magnet number 15012 is shown in Fig. 3-30.

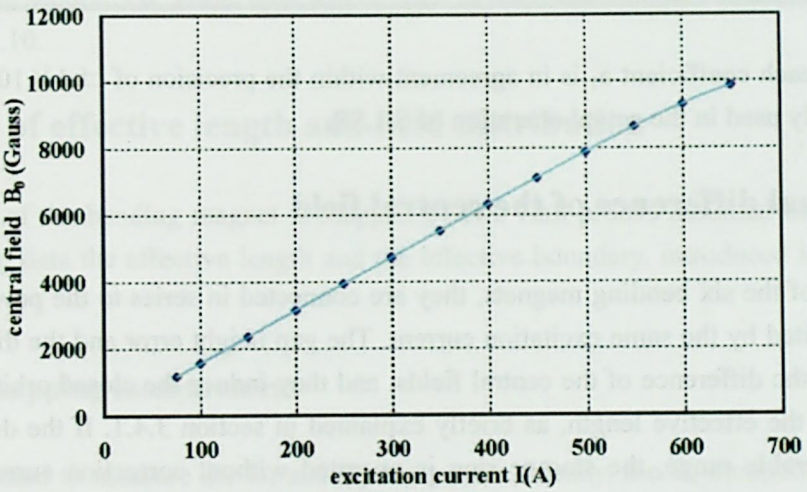

Fig. 3-30. B-I curve of the bending magnet No. 15012.

The central field deviates from the linear proportion to the excitation current at high excitation current. This deviation originates in the saturation of the iron core. In order to express the relation between the excitation current and the central field of each bending magnet, quantitatively, we expand the B-I curve by the following polynomial.

$$B(I) = a_0 + a_1 I + a_2 I^2 + a_3 I^3 + a_4 I^4 + a_5 I^5 + \ldots \qquad (3\text{-}14)$$

Then, each coefficient is shown in Table. 3-5.

Table. 3-5. Coefficients of the expansion of B-I curve

Magnet No.	15012	15013	15014	15015	15016	15017
a_0	5.515E+01	4.948E+01	4.974E+01	5.289E+01	4.979E+01	4.613E+01
a_1	1.421E+01	1.437E+01	1.437E+01	1.427E+01	1.435E+01	1.446E+01
a_2	1.475E-02	1.310E-02	1.303E-02	1.418E-02	1.321E-02	1.201E-02
a_3	-6.140E-05	-5.333E-05	-5.256E-05	-5.890E-05	-5.371E-05	-4.706E-05
a_4	1.162E-07	9.584E-08	9.279E-08	1.104E-07	9.645E-08	8.056E-08
a_5	-7.979E-11	-5.452E-11	-4.953E-11	-7.308E-11	-5.518E-11	-3.495E-11

In Table 3-5, the deviation of the coefficient of the linear component a_1 is too large despite usage of the same power supply and the material of the iron core. In low excitation level, where the effect of the saturation is negligible, the coefficient of the linear component is given by Eq. 3-3. The cause of the deviation of the constant term a_0 and the linear component a_1 might be the error of the fitting due to including up to high excitation level in the expansion of B-I curve. If the expansion is limited in the low excitation region, the exact a_1 and a_0 may be obtained. When the relation of B and I is fitted by a linear function $B(I) = a_0 + a_1 I$ in the low excitation region up to 250A, 4000 Gauss, the coefficients becomes as shown in Table 3-6.

Table 3-6. Coefficients of the expansion of B-I line. (Low excitation region)

Magnet No.	15012	15013	15014	15015	15016	15017
a_0	-4.1277E+00	-3.9880E+00	-3.9059E+00	-3.8285E+00	-4.2387E+00	-4.0818E+00
a_1	1.5787E+00	1.5786E+01	1.5786E+01	1.5786E+01	1.5786E+01	1.5784E+01

It is found that each coefficient a_1 is in agreement within the precision of $\pm 1 \times 10^{-4}$. This excitation region is most frequently used in the actual operation of S-LSR.

3.7 Individual difference of the central field

In actual use of the six bending magnets, they are connected in series to the power supply. Therefore, all magnets are excited by the same excitation current. The gap height error and the difference of the magnetic property induce the difference of the central fields, and they induce the closed orbit distortion together with the deviation of the effective length, as briefly explained in section 3.4.1. If the degree of the closed orbit distortion is tolerable range, the storage ring is operated without correction current, although the bypass circuit is equipped to the power supply The bypass circuit can adjust the excitation current of each magnet individually. Delicate adjustment of the main excitation current is required in the actual circulation of a beam. If the correction of each excitation current is performed, each time, the operation becomes very complicated. Therefore, we want to operate the storage ring without using the correction current basically. However, in the case of dispersion-free operating mode (where the horizontal aperture is rather limited as 30 mm (see chapter 4)), careful adjustment of each excitation current may be required.

In order to decide the necessity of the correction current, we investigated the individual difference of the central field. The central field was measured by the NMR at the end of the mapping measurement, since the temperature of the iron core was considered relatively stable. The central field is slightly affected by the temperature of the iron core because of the thermal expansion of the gap height. The central fields obtained from each measurement are shown in table 3-7.

Table 3-7-a. Central field of each bending magnet

Magnet NO.	Central field (Gauss)	Excitation current (A)	Air temperature in the gap (℃)
15012	4337.876	274.1160	26.4
15013	4337.541	274.1198	25.9
15014	4337.159	274.1180	26.3
15015	4337.588	274.1200	27.2
15016	4337.106	274.1170	26.1
15017	4336.779	274.1182	26.7

Table 3-7-b. Converted central field excited with the completely same excitation current 274.12 (A)

Magnet NO.	Central field at the same excitation current(Gauss); Average value: 4337.370 Gauss	Deviation
15012	4337.939	1.3E-04
15013	4337.544	4.0E-05
15014	4337.191	-4.1E-05
15015	4337.588	5.0E-05
15016	4337.153	-5.0E-05
15017	4336.807	-1.3E-04

The excitation current in each measurement is slightly different because of the difference of the circumstances of the power supply. Thus, each central field is corrected for the same excitation current using the B-I curves obtained in section 3.6. These data will be used in the estimation of the closed orbit distortion, as described in section 3.10.

3.8 Measurement of effective length and field distribution

The field distribution of the bending magnet is mapped by two Hall-probes mounted on the 3 axis drive stage. From the mapping data the effective length and the effective boundary, introduced in section 3.3, are calculated.

3.8.1 Setup of the mapping measurement

Two Hall probes are used to measure the B_x and B_y component. Ideally, the B_x component is zero on the median plane because of the symmetry of the magnet. Two Hall-probes are installed on a two axis holder (Fig 3-31-a). The holder is made so that the base plates (reference surfaces) of the Hall-probes intersect at right angles between each other. However, the Hall-sensor may have finite angle against to the base plate (Fig 3-26-a). Therefore, finally, the installation angle of the B_y Hall-probe was adjusted so that it observes the largest value of magnetic field. B_x Hall-probe was used for the purpose of the confirmation of the B_x field, although we did not use the B_x component for the beam dynamics calculation. Nevertheless, it is difficult to

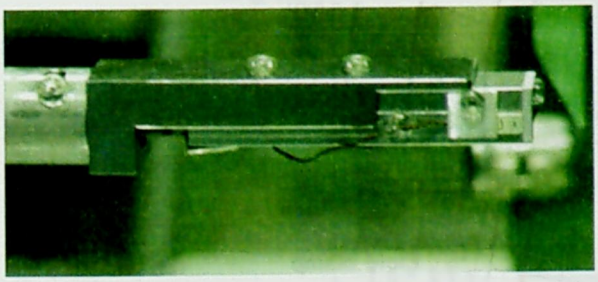

Fig 3-31-a. Two axis Hall-probe holder.

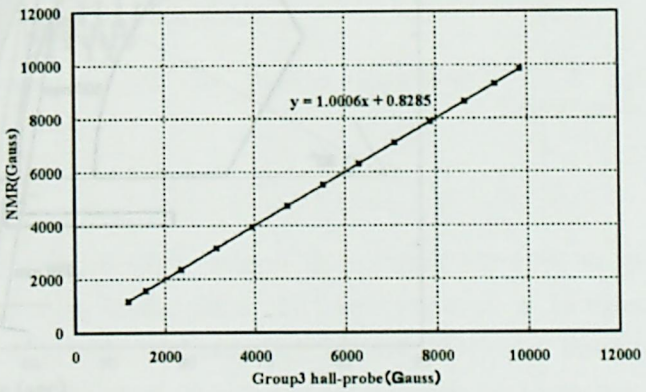

Fig 3-31-b. The calibration line of the measured value of B_y Hall-probe. B_y corresponds to y and x is the bare value of the B_y Hall probe.

set the sensor surface perpendicularly to B_y. The measured value of the Hall probe is proportional to the value of NMR. Therefore, we can calibrate the value of the Hall-probe by the value of NMR (Fig 3-31-b). The relation of these values was investigated each time when the setup of the mapping measurement is changed. The setup of the mapping measurement is shown in Fig. 3-32. The longitudinal axis of the drive stage has a crossing angle of 10 degree against to the normal line of the pole edge. The probe accessible area is limited due to the small aperture of the field clamp. The probe accessible area is shown in Fig 3-33. Thus, we divide the mapping region into two regions; beam exit side and entrance side.

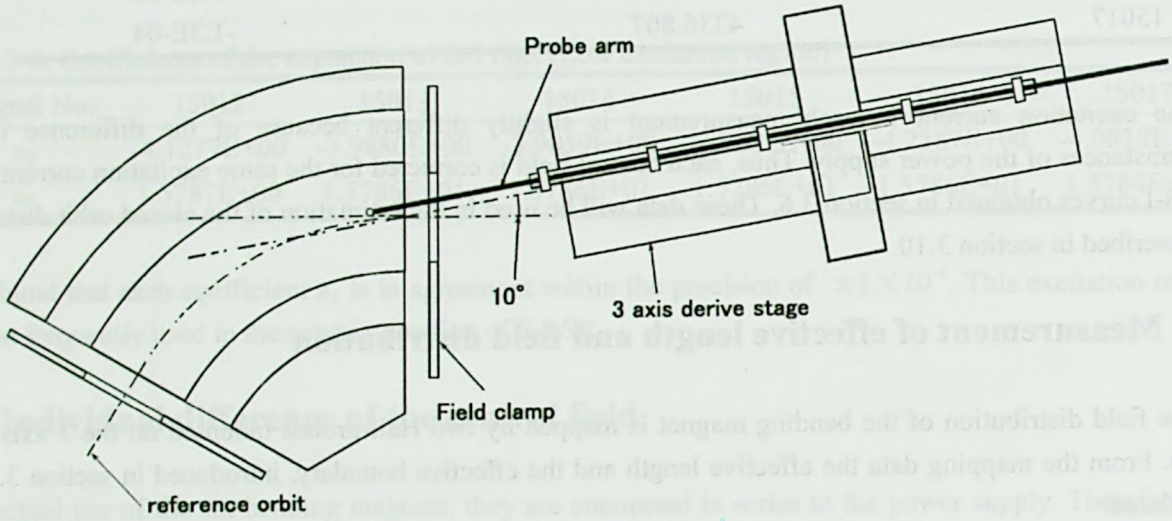

Fig 3-32. Setup of the mapping measurement

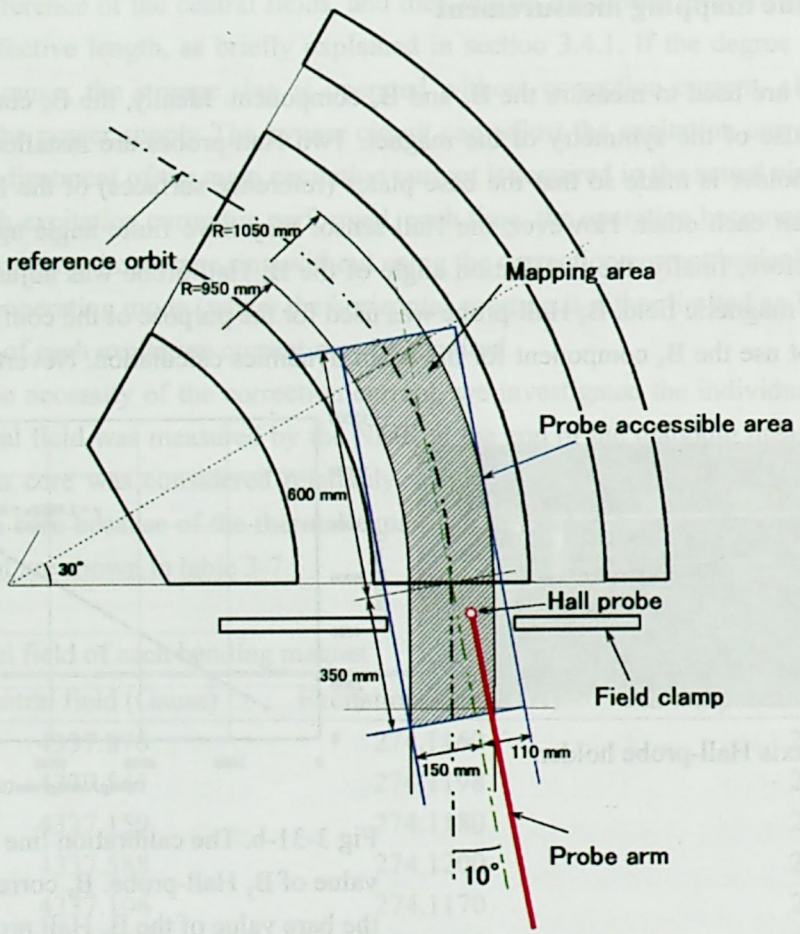

Fig .3-33. Probe accessible area and the mapping area.

3.8.2 Decision of the mapping grid interval

The measurement was performed on the points of square grids. When the drive stage reaches to the target point and stops, the probe arm starts oscillation. This oscillation may influence the measurement at the fringing region. The oscillation damps according to time. And, the amplitude of the oscillation can be reduced with the slow driving speed. However, if the enough waiting time for the oscillation damping and the low driving speed are selected, long mapping time is needed. Therefore, the suitable waiting time and the driving speed have to be investigated. It was also found that the degree of the oscillation was also depending on the drive interval; i.e. the suitable drive method has to be considered together with the size of the mapping grid. The size of the mapping grid also decides the total mapping time. As the grid interval becomes large, the needed mapping time reduces, but the accuracy of the field integration becomes worse.

First, two mapping were performed on the line of the reference orbit in the fringing region (the waiting time to avoid the influence of the oscillation is ensured enough). One is 5 mm interval, the other is 10 mm interval. Then the difference of these effective length was 4.6×10^{-7} m. Therefore, we decided the grid interval to 10 mm, taking into account the total mapping time.

Next, the waiting time at each mapping point and the treatment of the data measured at the mapping point were considered. As shown in Fig. 3-7, when the bending magnets used in the ring the, quadrupole magnets are put near the bending magnet. Therefore, the mapping was also performed with the quadrupole magnet. The influence of the oscillation of the Hall-probe must be remarkable in the quadrupole field. Therefore, if the suitable driving method is established in the quadrupole field, it is enough for the measurement of the bending magnetic field. The data of the Hall-probe is read out every 0.15 seconds, after reaching to the target point. In Fig. 3-34, the data of 5 measurement points which are measured by the Hall-probe is shown. The Hall-probe moves in the quadrupole field, and measures the field during 15 sec at each measurement point. When the measurement modes of the tesla meter DTM-151 is selected "filter on", the response in a changing field becomes worse. Therefore, we used the tesla meter in the mode "filter off" and finally the measurement value was averaged at each measurement point.

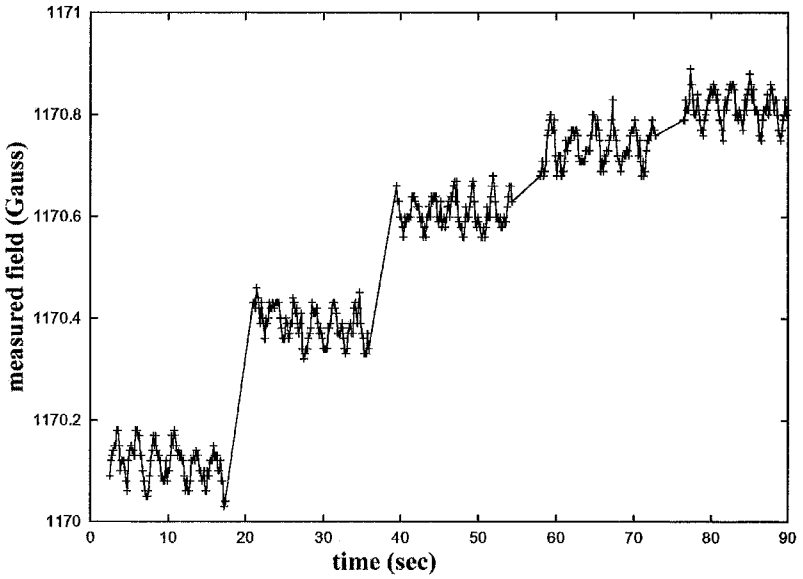

Fig. 3-34. The value which was read out from the Hall-probe. The data of the Hall probe during the measurement of 5 points in the quadrupole magnet is plotted. In this case, the driving seed is selected suitably. Thus, it is found that the effect of the oscillation is negligible compared with the fluctuation due to the efficiency of the Hall probe.

As seen in Fig 3-34, it was found that the measured value at each point was fluctuating in the state "Filter off". This fluctuation originates from the property of the Group3 Hall-probe, but not the influence of the oscillation. In Fig. 3-34, since the driving seed is selected suitably, the influence of the oscillation does not arise. The oscillation of the probe arm dumps almost completely, in 1 sec, even if the drive speed and the interval of the measurement points are not selected suitably. Finally, it was decided so that the probe waits during 1 sec after reaching the target point and then the probe measures the field 10 times during 1.5 sec. The averaged value of the 10 times measurement at each point and the original 10 data were recorded, respectively.

3.8.3 Alignment method

In order to obtain the exact effective length and field distribution, the measured field value is needed to be corresponded to the exact coordinate of its measuring point. Therefore, exact alignment of the banding magnet and the 3-axis drive stage is essential. Especially to decide the relative longitudinal position of the probe center to the bending magnet is important. In the case of S-LSR bending magnet, the possible mapping

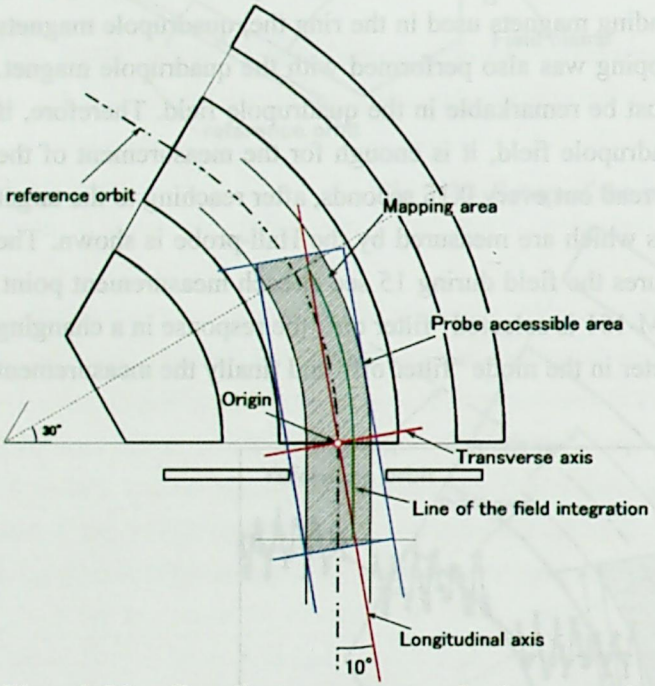

Fig. 3-35. Coordinate system of the mapping measurement

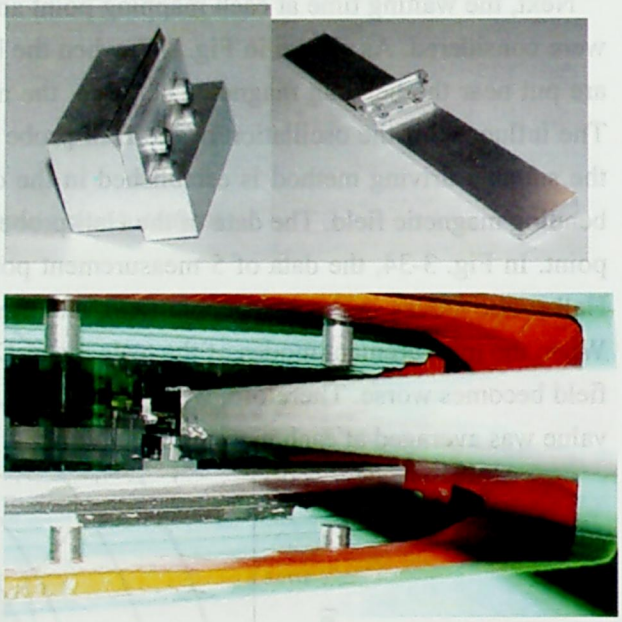

Fig. 3-36-a. The knife-edge was mounted on the aluminum. Then, the aluminum block was placed on the Rogowski's cut. The data shown in Fig. 3-37 was obtained by the mapping measurement across the edge.

area at the same time is half region of the bending magnet, as show in Fig. 3-33. (If all regions can be measured at the same time, this complicated process is unnecessary, because the effective length can be obtained merely integrating the measured field in the longitudinal direction.) Therefore, the longitudinal deviation of the alignment is reflected to the error of the effective length almost directly.

First, the longitudinal derive axis of the 3-axis drive stage was aligned with the line which has inclination of 10 degree from the normal line of the pole edge (Figs 3-32 and 3-33). The position of the stage was recorded as the pulse number sent from the pulse motor. The 1 pulse corresponds to 5 μ m. The pitch of the

ball screw of the drive stage is 5 mm. The pulse motor turns one turn by 1000 pulse. In order to avoid the back rash of the screw shaft, the measurement was always performed, driving to the same direction. The coordinate system and the origin of the mapping measurement were decided as shown in Fig. 3-35. It is difficult to align the center of the Hall-probe sensor by using the mark on the probe, because this mark may include the error. The most exact method is to use the magnetic field sensed by the Hall-sensor. The precise position of the center of the Hall probe to the magnetic field center was calibrated with use of the sharp edge of a knife set to a certain position on the Rogowski's cut (Fig. 3-36) When the field was mapped on the line crossing this edge, the field distribution shown in Fig. 3-37 was obtained. This field distribution can be fitted by Gaussian. From the coordinate of the center of this Gaussian the absolute position of the origin was obtained.

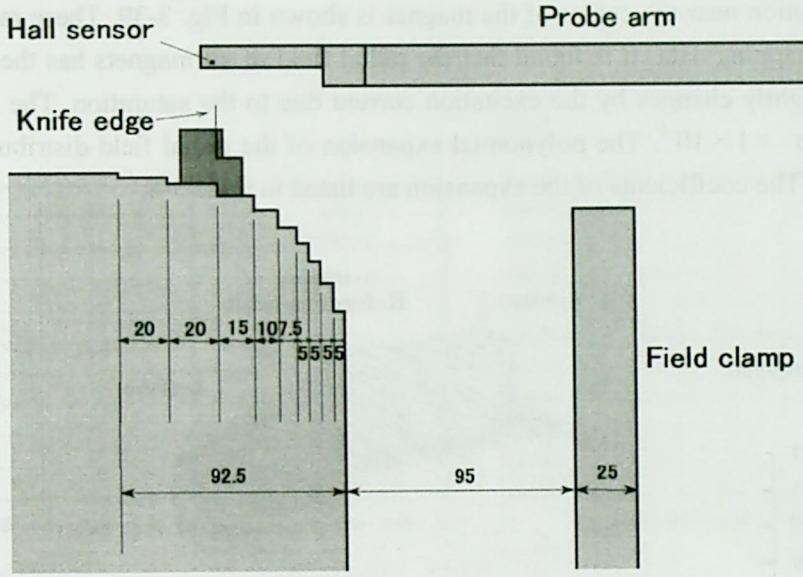

Fig. 3-36-b. The set up of the measurement to calibrate the precise position of the center of the Hall probe and the magnetic field center with use of a sharp edge of a knife set on the Rogowski's cut. The field distribution along the line across the edge becomes as shown in Fig 3-37.

(a)Mapping data to decide the longitudinal origin

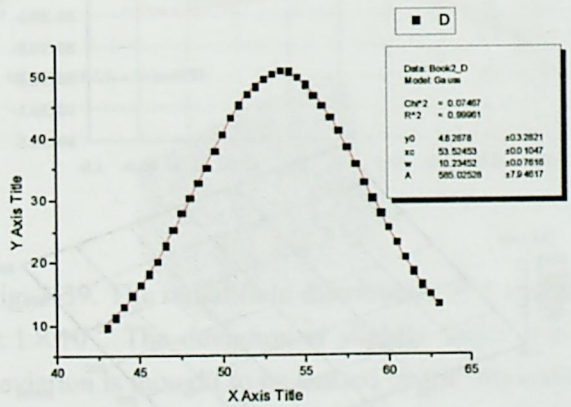

(b) Mapping data to decide the transverse origin

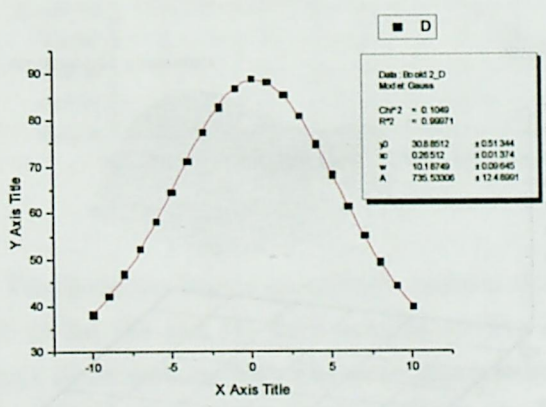

Fig. 3-37. The field distribution obtained from mapping measurement across the edge. When the edge is sharp, this field distribution can be fitted by Gaussian.

3.9 Analysis of the measured field

The mapped data becomes as shown in Fig. 3-38. From this data, effective length and the effective boundary is calculated. Since the mapped field data exists on the points of rectangular grids, the mapped points may not locate on the line of the field integration (Fig. 3-35). Therefore, interpolation of the points was performed. The mapped data were analyzed on the Frenet-Serret coordinate system defined in section 3.3.3.1.

3.9.1 Radial field distribution

The radial field distribution near the center of the magnet is shown in Fig. 3-39. These radial distribution were obtained from the mapping data. It is found that the radial field of all magnets has the same tendency. The radial distribution slightly changes by the excitation current due to the saturation. The deviation of the field distribution is within $\pm 1 \times 10^{-4}$. The polynomial expansion of the radial field distribution correspond to Eq. (3-7) is performed. The coefficients of the expansion are listed in table 3-8.

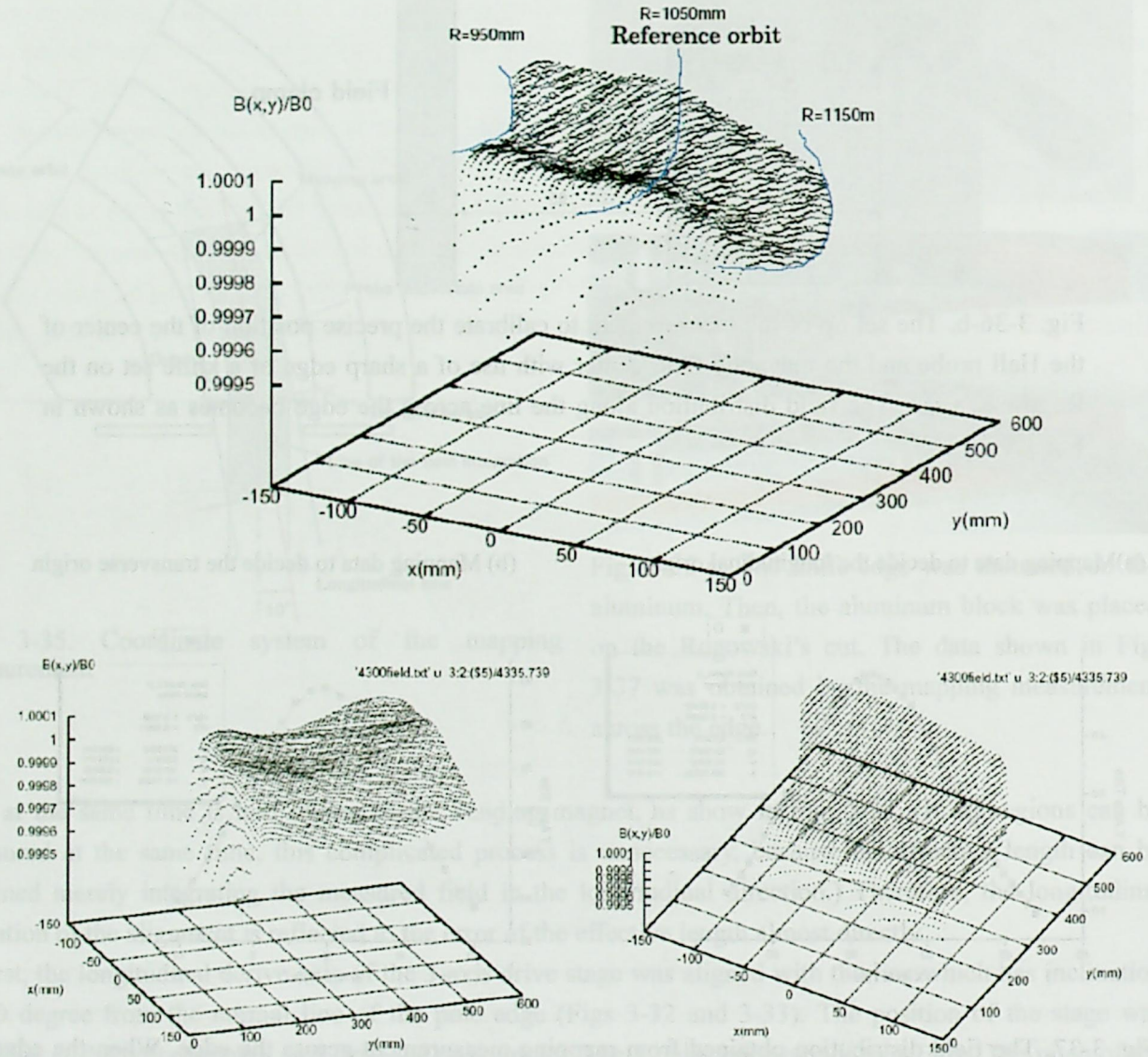

Fig.3-38. Mapped field distribution enough inner gap of the dipole magnet.

15012

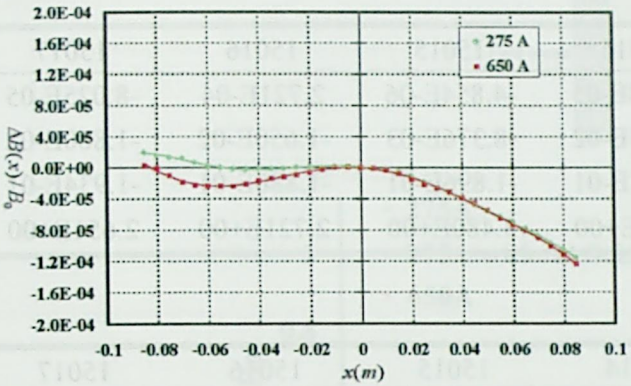

15013

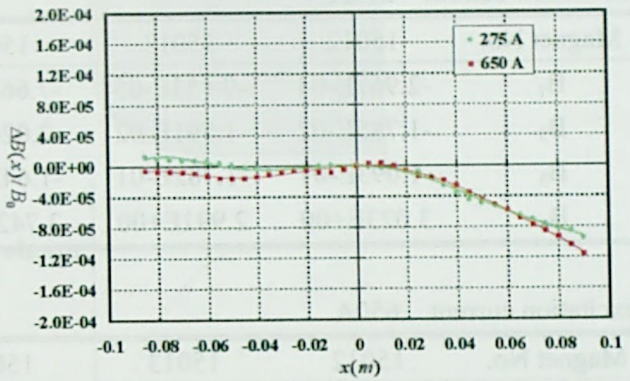

15014

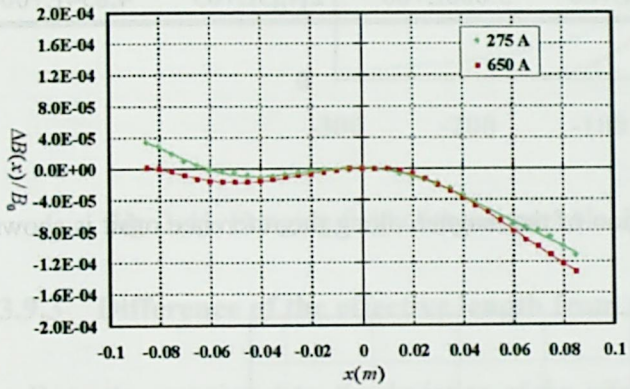

15015

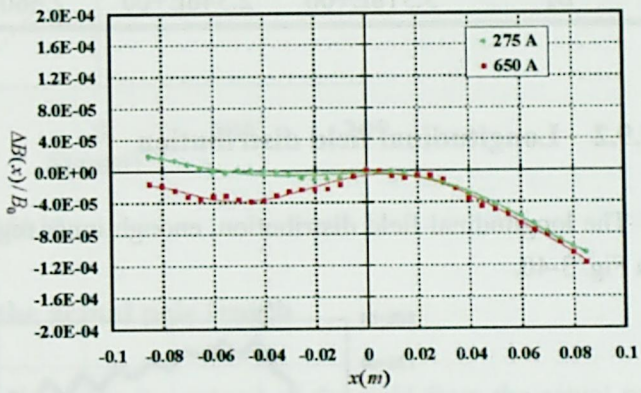

15016

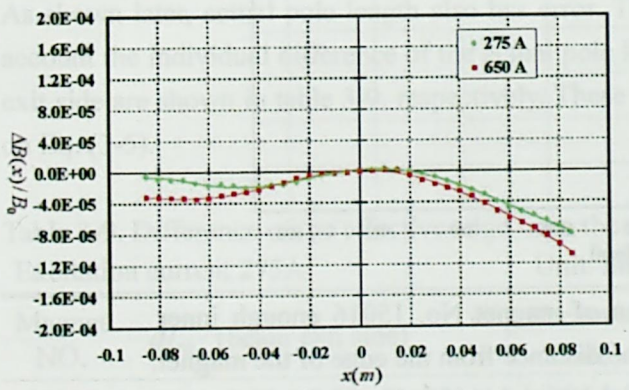

15017

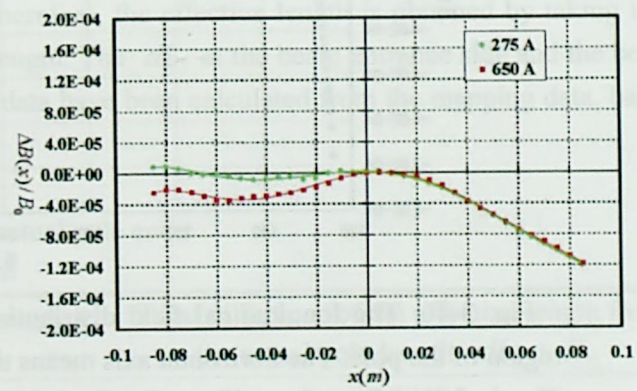

Fig. 3-39. The radial field distribution of 6 magnets. The deviation from a completely uniform field is within $\pm 1 \times 10^{-4}$. The deviation is slightly larger than that of the 2D and 3D field calculation (Fig 3-18). This deviation is thought to be caused by the fabrication error of the pole surface. The error appears similarly with all magnets. This tendency is thought to originate from the method of the shaping of the pole surface. The pole surfaces of 6 magnets were simultaneously shaped on a very large lathe.

Table 3-8. Coefficients of the polynomial expansion of the radial field distribution.

excitation current 275A

Magnet No.	15012	15013	15014	15015	15016	15017
B_1	-2.967E-04	-9.153E-05	-7.668E-05	-4.854E-06	2.721E-04	-8.025E-05
B_2	-1.785E-02	-1.591E-02	-2.024E-02	-8.376E-03	-1.650E-02	-1.860E-02
B_3	-1.093E-01	-1.782E-01	-1.642E-01	-1.896E-01	-1.880E-01	-1.934E-01
B_4	3.023E+00	2.991E+00	3.742E+00	3.480E+00	2.721E+00	2.651E+00

excitation current 650A

Magnet No.	15012	15013	15014	15015	15016	15017
B_1	-1.841E-04	7.969E-05	-3.276E-05	3.880E-04	4.641E-05	3.060E-04
B_2	-2.278E-02	-1.631E-02	-2.102E-02	-2.242E-02	-2.012E-02	-2.734E-02
B_3	-4.632E-02	-1.694E-01	-2.007E-01	-2.245E-01	-7.602E-02	-2.438E-01
B_4	3.318E+00	2.346E+00	2.660E+00	3.606E+00	2.453E+03	4.834E+00

3.9.2 Longitudinal field distribution

The longitudinal field distribution, enough inner region of the magnet, along the reference orbit is shown in Fig. 3-40.

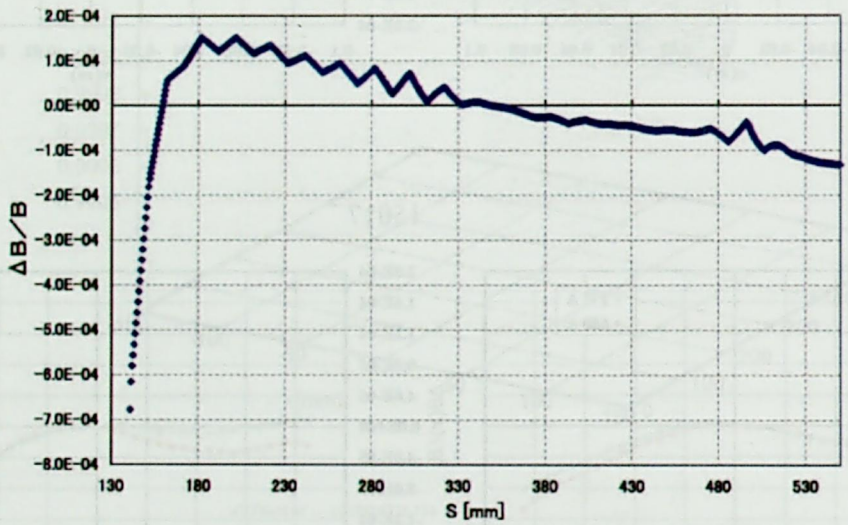

Fig. 3-40. The longitudinal field distribution of magnet No. 15016 enough inner region of the pole. The horizontal axis means the distance from the edge of the magnet. The deviation from the uniform distribution is about $\pm 1 \times 10^{-4}$. The deviation of the longitudinal field distributions of the other magnets is smaller than that of magnet No.15016.

The longitudinal field distribution in the fringing region is shown in Fig. 3-41. It is found that the structure of the fringing field doesn't depend on the excitation current, and the tail of the fringing field is well suppressed by the field clamp.

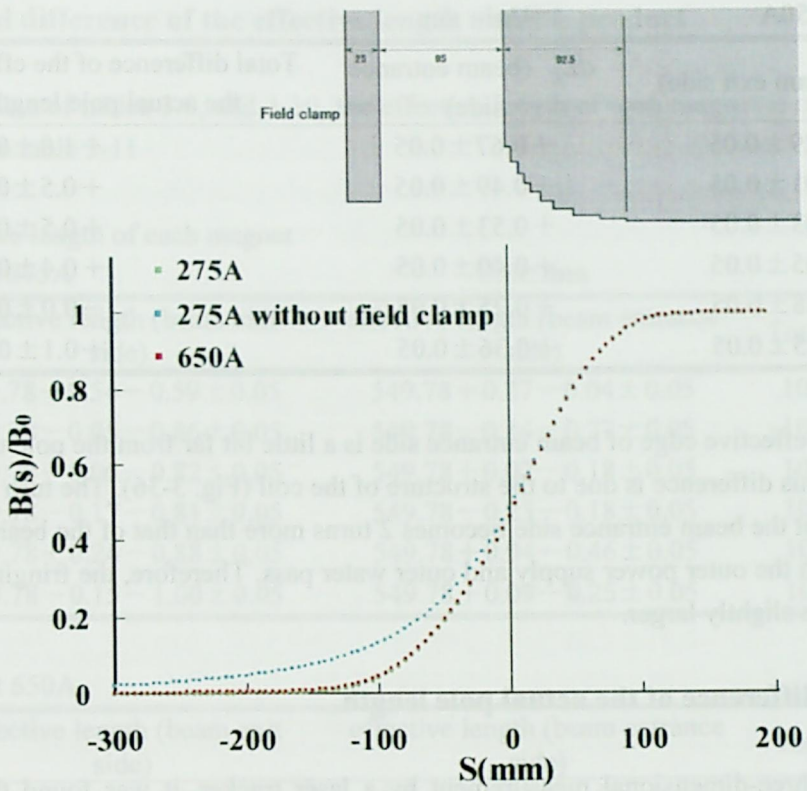

Fig. 3-41. Fringing field of the magnet No. 15012

3.9.3 Difference of the effective length from the actual pole length

From the mapping data, the deviation of the effective edge (boundary) of the field from the actual pole edge is obtained. We define this value as dL;

$$dL = \int_{half\ region} B_y(0,0,s)/B_0 ds - \text{actual half pole length}$$

As shown later, actual pole length also has error. Therefore, the effective length is obtained by taking into account the individual difference of the actual pole length. The dL at the beam entrance side and the beam exit side are shown in table 3-9, respectively. These data have been calculated from the mapping data, based on Eq. (3-5).

Table 3-9. Difference of the effective edge from the actual pole end.

Excitation current 275A Unit: mm

Magnet NO.	dL_R (beam exit side)	dL_L (beam entrance side)	Total difference of the effective length from the actual pole length $dL_R + dL_L$
15012	-0.59 ± 0.05	-0.04 ± 0.05	-0.6 ± 0.1
15013	-0.86 ± 0.05	-0.27 ± 0.05	-1.1 ± 0.1
15014	-0.82 ± 0.05	-0.18 ± 0.05	-1.0 ± 0.1
15015	-0.81 ± 0.05	-0.18 ± 0.05	-1.0 ± 0.1
15016	-0.88 ± 0.05	-0.46 ± 0.05	-1.3 ± 0.1
15017	-1.00 ± 0.05	-0.25 ± 0.05	-1.3 ± 0.1

Excitation current 650A		Unit: mm	
Magnet NO.	dL_R (beam exit side)	dL_L (beam entrance side)	Total difference of the effective length from the actual pole length $dL_R + dL_L$
15012	$+0.29 \pm 0.05$	$+0.67 \pm 0.05$	$+1.0 \pm 0.1$
15013	-0.01 ± 0.05	$+0.49 \pm 0.05$	$+0.5 \pm 0.1$
15014	-0.03 ± 0.05	$+0.53 \pm 0.05$	$+0.5 \pm 0.1$
15015	-0.05 ± 0.05	$+0.40 \pm 0.05$	$+0.4 \pm 0.1$
15016	-0.28 ± 0.05	$+0.25 \pm 0.05$	-0.0 ± 0.1
15017	-0.25 ± 0.05	$+0.36 \pm 0.05$	$+0.1 \pm 0.1$

In all magnets, the effective edge of beam entrance side is a little bit far from the pole edge compared with the beam exit side. This difference is due to the structure of the coil (Fig. 3-36). The turn number of the head band part of the coil at the beam entrance side becomes 2 turns more than that of the beam exit side, because of the connection with the outer power supply and outer water pass. Therefore, the fringing field at the beam entrance side becomes slightly larger.

3.9.4 Individual difference of the actual pole length

From the precise three-dimensional measurement by a laser tracker, it was found that the actual pole length has individual difference. The length shown in Fig. 3-42 was measured.

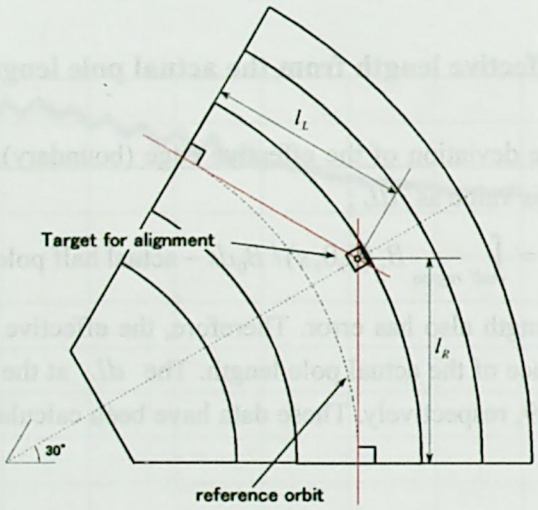

Fig. 3-42. Measured length to investigate the individual difference of the actual pole length

Table 3-10. Actual pole length of the 6 bending magnets. Unit: mm

Magnet No	l_R (beam exit side)	l_L (beam entrance side)	Total actual pole length along the reference orbit	deviation from the ideal value
15012	605.68	606.49	1099.281	-0.279
15013	606.17	606.08	1099.371	-0.189
15014	606.16	606.24	1099.523	-0.037
15015	606.05	605.99	1099.160	-0.400
15016	606.48	606.26	1099.857	0.297
15017	606.07	606.31	1099.506	-0.054
ideal value	606.22	606.22	1099.560	

3.9.5 Individual difference of the effective length and BL product

Combining the data of tables 3-9, and 3-10, the effective length of each magnet is obtained. These values become as shown in table 3-11

Table 3-11. Effective length of each magnet

Excitation current 275A Unit: mm

Magnet NO.	effective length (beam exit side)	effective length (beam entrance side)	Total effective length
15012	549.78−0.54−0.59±0.05	549.78+0.27−0.04±0.05	1099.56−0.9±0.1
15013	549.78−0.05−0.86±0.05	549.78−0.14−0.27±0.05	1099.56−1.3±0.1
15014	549.78−0.06−0.82±0.05	549.78+0.02−0.18±0.05	1099.56−1.0±0.1
15015	549.78−0.17−0.81±0.05	549.78−0.23−0.18±0.05	1099.56−1.4±0.1
15016	549.78+0.26−0.88±0.05	549.78+0.04−0.46±0.05	1099.56−1.0±0.1
15017	549.78−0.15−1.00±0.05	549.78+0.09−0.25±0.05	1099.56−1.3±0.1

Excitation current 650A

Magnet NO.	effective length (beam exit side)	effective length (beam entrance side)	Total effective length
15012	549.78−0.54+0.29±0.05	549.78+0.27+0.67±0.05	1099.56+0.7±0.1
15013	549.78−0.05−0.01±0.05	549.78−0.14+0.49±0.05	1099.56+0.3±0.1
15014	549.78−0.06−0.03±0.05	549.78+0.02+0.53±0.05	1099.56+0.5±0.1
15015	549.78−0.17−0.05±0.05	549.78−0.23+0.40±0.05	1099.56−0.1±0.1
15016	549.78+0.26−0.28±0.05	549.78+0.04+0.25±0.05	1099.56+0.3±0.1
15017	549.78−0.15−0.25±0.05	549.78−0.15+0.36±0.05	1099.56+0.1±0.1

The deviation of the BL product at the excitation current 275 A (274.12 A) can be obtained from tables. 3-7 and 3-11, the result is shown in Fig 3-43.

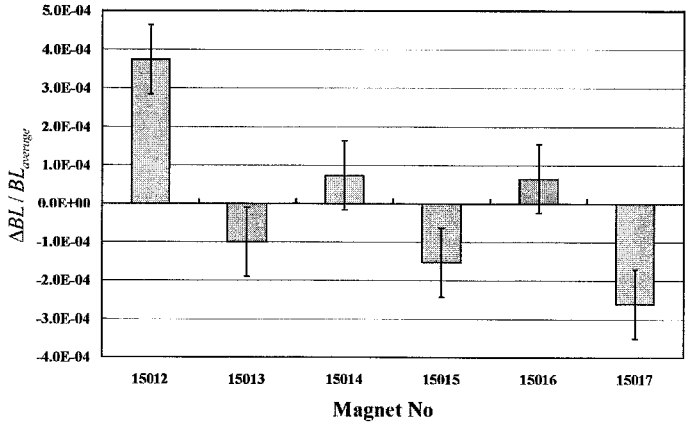

Fig 3-43. Deviation of the BL products at the excitation current 275 A.

In Fig. 3-43, the BL product of the magnet No. 15012 is obviously large. In order to reduce the size of the deviation of the BL products the position of the field clamp of magnet No. 15012 was shifted 2 mm to the pole side. By the 2D field calculation, the reduction of the effective length was estimated to be shortened

0.27 mm. The result of the field measurement showed that the effective length on the reference orbit has been shortened about 0.30 mm. (Table. 3-12)

By this adjustment, the individual difference of the effective length and the BL products were reduced at low excitation current. Even for the high excitation current, the individual difference of the effective length and the BL products were reduced. After the adjustment of the effective length of the magnet No. 15012, the following effective length and BL products has been obtained.

Table 3-12. Effective length of each magnet, after the adjustment the effective length of the magnet No 15012.

Excitation current 275A Unit: mm

Magnet NO.	effective length (beam exit side)	effective length (beam entrance side)	Total effective length
15012	549.78−0.54−0.92±0.05	549.78+0.27−0.33±0.05	1099.56−1.5±0.1
15013	549.78−0.05−0.86±0.05	549.78−0.14−0.27±0.05	1099.56−1.3±0.1
15014	549.78−0.06−0.82±0.05	549.78+0.02−0.18±0.05	1099.56−1.0±0.1
15015	549.78−0.17−0.81±0.05	549.78−0.23−0.18±0.05	1099.56−1.4±0.1
15016	549.78+0.26−0.88±0.05	549.78+0.04−0.46±0.05	1099.56−1.0±0.1
15017	549.78−0.15−1.00±0.05	549.78+0.09−0.25±0.05	1099.56−1.3±0.1

Excitation current 650A

Magnet NO.	effective length (beam exit side)	effective length (beam entrance side)	Total effective length
15012	549.78−0.54+0.19±0.05	549.78+0.27+0.35±0.05	1099.56+0.3±0.1
15013	549.78−0.05−0.01±0.05	549.78−0.14+0.49±0.05	1099.56+0.3±0.1
15014	549.78−0.06−0.03±0.05	549.78+0.02+0.53±0.05	1099.56+0.5±0.1
15015	549.78−0.17−0.05±0.05	549.78−0.23+0.40±0.05	1099.56−0.1±0.1
15016	549.78+0.26−0.28±0.05	549.78+0.04+0.25±0.05	1099.56+0.3±0.1
15017	549.78−0.15−0.25±0.05	549.78−0.15+0.36±0.05	1099.56+0.1±0.1

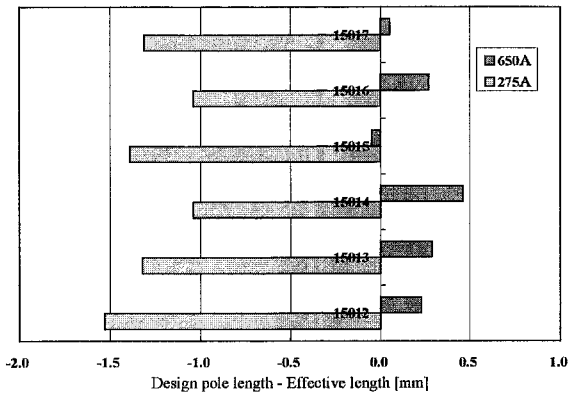

Fig 3-44. Deviation of the effective length from the design pole length.

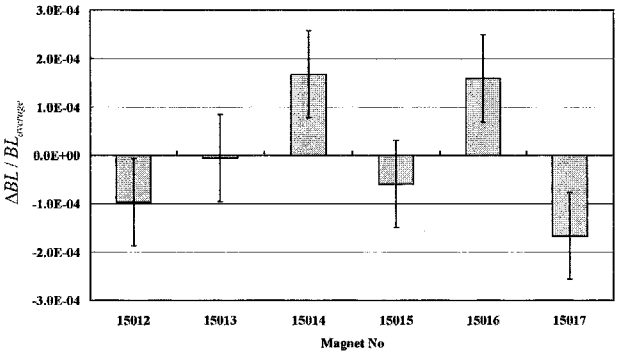

Fig. 3-45. Deviation of the BL products at the excitation current 275 A.

3.9.6 Effective boundary and multi-pole component

The information of the multi-pole component of the measured field can be obtained by comparing the measured effective boundary and the formula of effective boundary Eq. (3-12)

Therefore, by comparing the expansion of the measured $\Delta l_{eff}(x)$ with the right hand side of Eq. (3-12) the total value of the multi-pole component $B_nL/n!$ (B_nL product) in the half region in the bending magnet can be estimated. However, as described in section 3.3.3.2, this is an approximate method. In this section, the multi-pole components are calculated from the effective boundary by the more precise method. As shown in Eq. (3-8), The field integration to obtain the effective boundary can be divided to inner gap region and the outer fringing region.

1. Effective boundary in the inner side of the magnet.

$$\Delta l_{eff}\Big|_{inner\ gap} = \frac{1}{B_0}\left(\int_{S_0}^{pole\ end} B_0(s)ds + x\cdot\int_{S_0}^{pole\ end} B_1(s)ds + x^2\cdot\left[\int_{S_0}^{pole\ end}\frac{1}{\rho_0}B_1(s)ds + \int_{S_0}^{pole\ end}\frac{1}{2!}B_2(s)ds\right] + x^3\left[\int_{S_0}^{pole\ end}\frac{1}{\rho_0}\frac{1}{2!}B_2(s)ds + \ldots\right]\right) \tag{3-15}$$

2. Effective boundary in the fringing region.

$$\Delta l_{eff}\Big|_{fringe} = \frac{1}{B_0}\left[\int_{pole\ end}^{\infty} B_0(s)ds + x\cdot\int_{pole\ end}^{\infty} B_1(s)ds + x^2\cdot\int_{pole\ end}^{\infty}\frac{1}{2!}B_2(s)ds + x^3\cdot\int_{pole\ end}^{\infty}\frac{1}{3!}B_3(s)ds\right] \tag{3-16}$$

The total effective boundary is the summation of Eq. (3-15) and Eq. (3-16). When the following notations are defined

$$C_n = \int_{S_0}^{pole\ end}\frac{1}{n!}B_n(s)ds \tag{3-17}$$

the effective boundary in the inner gap can be written as

$$\Delta l_{eff}\Big|_{inner\ gap} = C_0 + x\cdot C_1 + x^2\cdot\left(\frac{1}{\rho_0}C_1 + C_2\right) + x^3\cdot\left(\frac{1}{\rho_0}C_2 + C_3\right) + \ldots + x^n\left(\frac{1}{\rho_0}C_{n-1} + C_n\right) + \ldots. \tag{3-18}$$

The relations to the coefficients of the expansion of the effective boundary of the inner gap $\Delta l_{eff}\,|_{inner\ gap} = b_0 + b_1x + b_2x^2 + b_3x^3 + \ldots$ are given by

$$b_0 = C_0,\quad b_1 = C_1,\quad b_2 = \frac{1}{\rho_0}C_1 + C_2,\quad b_n = \frac{1}{\rho_0}C_{n-1} + C_n\ \ (n>2), \tag{3-19}$$

where b_n $(n \geq 0)$ is the known amount obtained from the measured effective boundary.

First C_0 and C_1 can be obtained by comparing the polynomial expansion of the measured effective boundary. Next the higher order component C_2 is obtained from the relation

$$b_2 = \frac{1}{\rho_0}C_1 + C_2$$

If the value of C_2 is decided, the higher-order component C_3 is also obtained by the similar way. Repeating such process, the coefficient C_n is decided one after another. By this way the actual multi-pole component in the inner gap region is obtained. The multi-pole components in the outer fringing region are obtained directly from the polynomial expansion of the measured effective boundary. The summation of the multi-pole component in each region becomes exact total multi-pole component in the bending magnet. The total multi-pole components in the half region of the magnet (beam entrance side and beam exit side) are shown in table 3-13.

Table 3-13. Total multi-pole component in the half region of the magnet.

$$b_0 = \frac{1}{B_0}\left(\int_{s_0}^{\infty} B_0(s)ds - B_0 l\right) = \Delta l_{eff}(0) \qquad b_n = \frac{1}{B_0}\int_{s_0}^{\infty}\frac{1}{n!}B_n(s)ds \tag{3-20}$$

beam entrance side
excitation current 275A

Magnet No.	15012	15013	15014	15015	15016	15017
b_0(m)	-3.350E-04	-2.732E-04	-1.851E-04	-1.724E-04	-4.647E-04	-2.476E-04
b_1(m^0)	-2.844E-04	-5.150E-04	-9.417E-04	8.795E-04	-5.260E-05	2.770E-05
b_2(m^{-1})	-2.529E-02	-2.050E-02	-1.497E-02	-2.189E-02	-1.793E-02	-1.772E-02
b_3(m^{-2})	-9.847E-02	-1.292E-01	-5.229E-02	-2.349E-01	-2.313E-01	-1.573E-01
b_4(m^{-3})	2.389E+00	7.831E-01	4.479E-01	1.532E+00	2.890E-02	-1.048E+00

excitation current 650A

Magnet No.	15012	15013	15014	15015	15016	15017
b_0(m)	3.481E-04	4.955E-04	5.250E-04	4.084E-04	2.576E-04	3.721E-04
b_1(m^0)	2.597E-04	-5.880E-04	-6.322E-04	1.209E-03	-9.770E-05	2.026E-04
b_2(m^{-1})	-2.383E-02	-2.292E-02	-3.063E-02	-2.504E-02	-3.147E-02	-2.892E-02
b_3(m^{-2})	-2.163E-01	-4.693E-02	-2.106E-01	-3.474E-01	-2.184E-01	-1.661E-01
b_4(m^{-3})	-4.074E-01	-1.137E+00	2.514E+00	-6.316E-01	-4.371E-01	-8.910E-03

beam exit side
excitation current 275A

Magnet No.	15012	15013	15014	15015	15016	15017
b_0(m)	-9.243E-04	8.581E-04	-8.241E-04	-8.141E-04	-8.397E-04	-1.006E-03
b_1(m^0)	-3.058E-04	-1.202E-04	-7.570E-05	1.570E-04	1.138E-03	-2.070E-05
b_2(m^{-1})	-2.695E-03	-1.519E-03	-1.470E-02	-2.037E-02	-5.072E-03	-1.019E-02
b_3(m^{-2})	-1.532E-01	-1.115E-01	-1.286E-01	-1.812E-01	-2.450E-01	-1.839E-01
b_4(m^{-3})	-3.392E-01	-2.089E+00	3.284E+00	3.351E+00	-2.722E-01	1.111E+00

excitation current 650A

Magnet No.	15012	15013	15014	15015	15016	15017
b_0(m)	1.890E-04	1.610E-06	-3.470E-05	-4.800E-05	-2.813E-04	-3.618E-04
b_1(m^0)	1.849E-04	3.270E-05	-5.563E-04	-1.997E-04	4.961E-04	-1.972E-04
b_2(m^{-1})	-4.230E-02	-7.567E-03	-2.683E-02	-2.980E-02	-1.096E-03	-1.994E-02
b_3(m^{-2})	-5.421E-02	-3.366E-02	-1.081E-01	-5.653E-02	-3.254E-02	9.001E-03
b_4(m^{-3})	5.794E+00	-1.918E+00	5.376E+00	3.122E+00	-9.832E-01	3.936E+00

In the followings, measured effective boundaries of all bending magnets are shown.

Fig. 3-46. Structure of the effective boundary of all magnets.

Magnet No 15012.

Beam entrance side

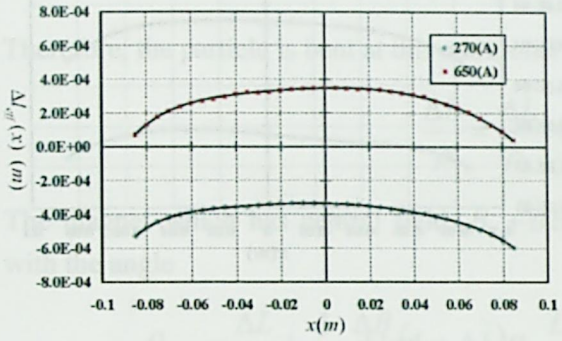

Beam exit side

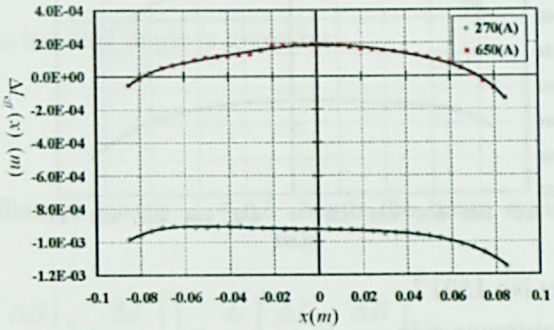

Magnet No 15013.

Beam entrance side

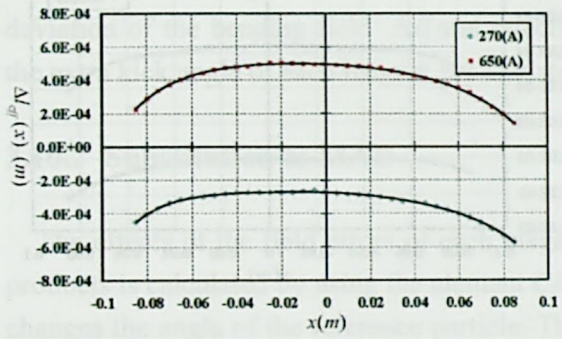

Beam exit side

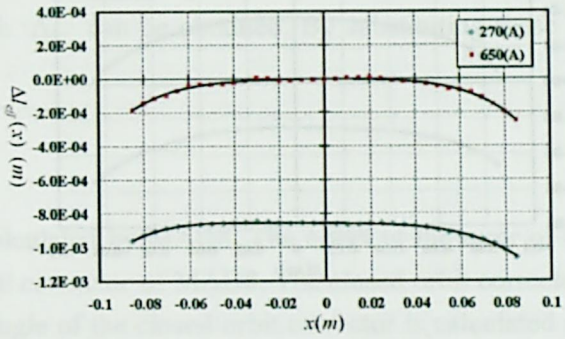

Magnet No 15014.

Beam entrance side

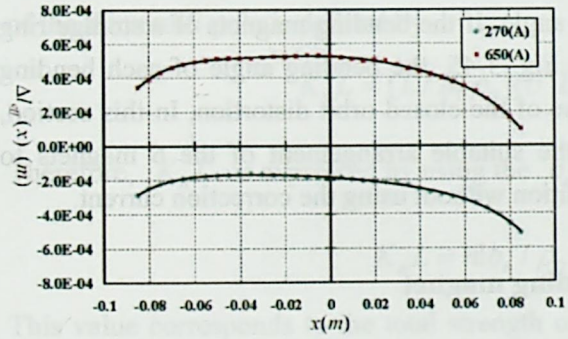

Beam exit side

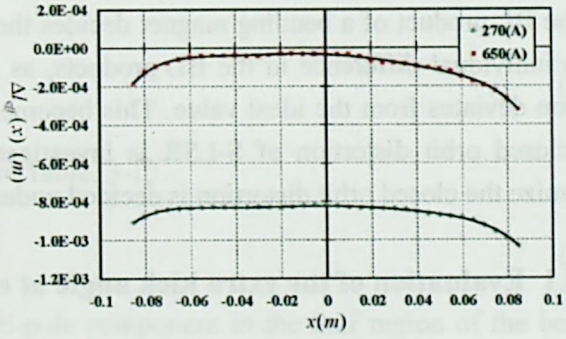

Magnet No 15015.

Beam entrance side

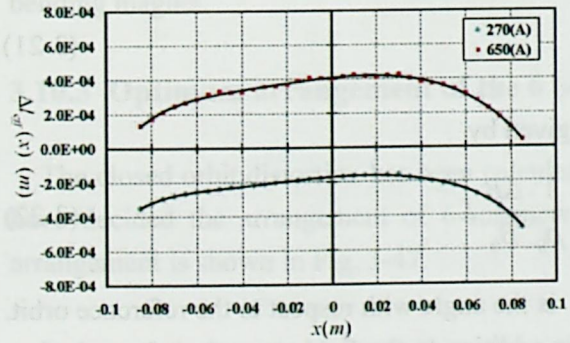

Beam exit side

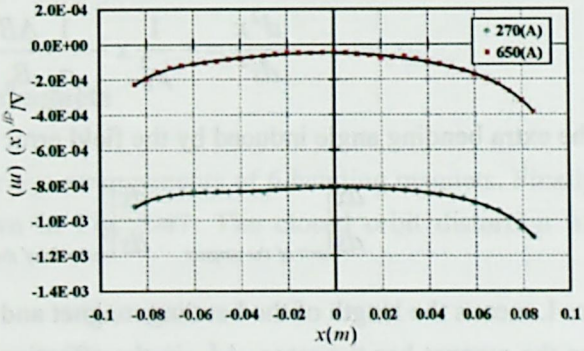

Magnet No 15016.

Beam entrance side

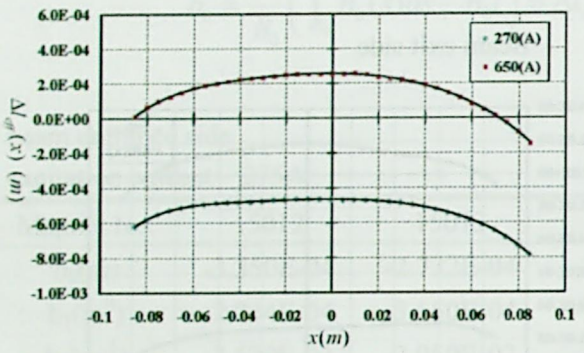

Beam exit side

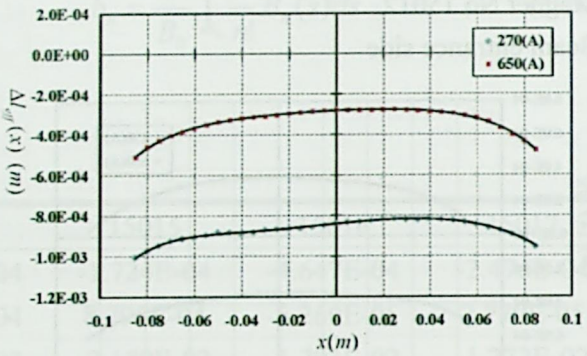

Magnet No 15017.

Beam entrance side

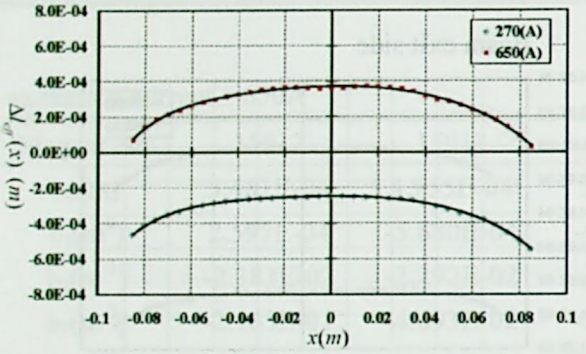

Beam exit side

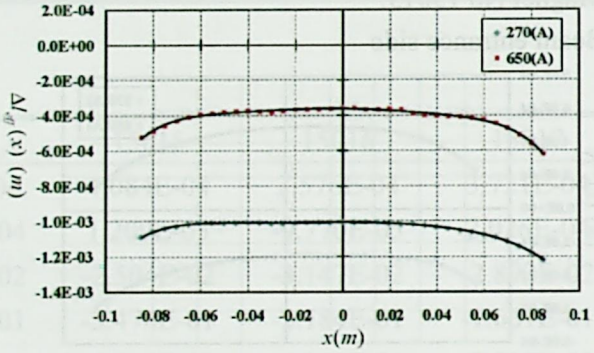

3.10 Arrangement of the 6 magnets to minimize the closed orbit distortion

The BL product of a bending magnet decides the bending angle. If the bending magnets of a storage ring have individual difference in the BL products, as shown in Fig. 3-45, the bending angle of each bending section deviates from the ideal value. This becomes the cause of the closed orbit distortion. In this section, the closed orbit distortion of S-LSR is investigated, and the suitable arrangement of the 6 magnets to minimize the closed orbit distortion is decided under the condition without using the correction current.

3.10.1 Evaluation of the extra kick angle at each bending magnet

When the bending magnet has error in the main dipole component B_0, the equation of motion of reference particle in this magnet becomes as [3-4]

$$\frac{d^2x}{ds^2} = -\frac{1}{\rho_0^2}x - \frac{1}{\rho_0}\frac{\Delta B}{B_0}. \tag{3-21}$$

The extra bending angle induced by the field error ΔB is given by

$$\left.\frac{dx}{ds}\right|_{exit\ of\ the\ amgnet} - \left.\frac{dx}{ds}\right|_{entrance\ of\ the\ amgnet} = \frac{1}{\rho_0}\frac{\Delta B}{B_0}L \tag{3-22}$$

where L means the length of the bending magnet and dx/ds is the angle with respect to the reference orbit. When the magnet has the error ΔL in the effective length, in addition to the field strength, it is equivalent

that the short bending magnet which has length ΔL and field strength $B_0 + \Delta B$ is attached to the ideal length bending magnet. The bending radius of the beam in this additional part is given by

$$\frac{1}{\rho} = \frac{1}{\rho_0} + \frac{1}{\rho_0}\frac{\Delta B}{B_0} \tag{3-23}$$

Therefore, the particle is bent at this additional part. This bending angle is given by

$$\frac{\Delta L}{\rho} = \frac{\Delta L}{\rho_0}\left(1 + \frac{\Delta B}{B_0}\right) \tag{3-24}$$

The magnet which has central field $B_0 + \Delta B$ and effective length $L + \Delta L$ bends the beam excessively with the angle

$$\theta_{kick} = \frac{\Delta L}{\rho_0} + \frac{1}{\rho_0}\frac{\Delta B}{B_0}(L + \Delta L) = \frac{L}{\rho_0}\left(\frac{\Delta L}{L} + \frac{\Delta B}{B_0}\left[1 + \frac{\Delta L}{L}\right]\right) \approx \frac{L}{\rho_0}\left(\frac{\Delta L}{L} + \frac{\Delta B}{B_0}\right), \tag{3-25}$$

compared to the magnet which has central field B_0 and effective length L. From tables 3-7 and 3-10, the deviation of the bending field ΔB and effective length ΔL can be obtained. By substituting these values the extra kick angle of each magnet is calculated.

3.10.2 Substitution to MAD

The effects of the field errors of each magnet are calculated by MAD8. The effect of the error of the BL products is calculated by using the element *Closed orbit corrector* of MAD8. The closed orbit corrector only changes the angle of the reference particle. The kick angle of the closed orbit corrector is calculated at both the beam entrance side and beam exit side. The kick angle of the closed orbit corrector is calculated from Eq. (3-25). The multi-pole components obtained in section 3.9.5 are also taken in MAD8. In MAD8 the strength of the thin multi-pole is defined by

$$K_n L = (L / B_0 \rho_0)(\partial^n B_y / \partial x^n) \tag{3-26}$$

Therefore, $K_n L$ is expressed by using the b_n shown in Table. 3-13.

$$K_n L = n! b_n / \rho_0 \tag{3-27}$$

This value corresponds to the total strength of the multi-pole component in the half region of the bending magnet (beam entrance side or the exit side). The multi-pole components are included to the transfer matrix calculation by a thin lens approximation. Such thin lenses are installed to the beam entrance and exit of the bending magnet.

3.10.3 Optimum arrangement of the 6 bending magnets

The closed orbit distortion has been calculated in various arrangements of 6 bending magnets. Finally, we have decided the arrangement of 6 magnets as shown in Fig. 3-47. The closed orbit distortion in this arrangement is shown in Fig. 3-47.

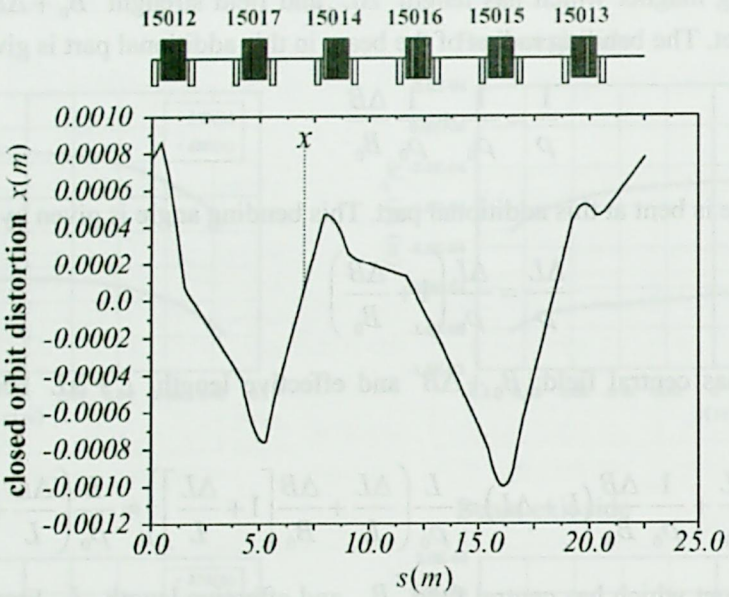

Fig 3-47. Arrangement of 6 bending magnets to minimize the closed orbit distortion. The closed orbit distortion was calculated at the operating point (1.74, 1.09). This operating point is to be used for the injection of 7 MeV proton. The closed orbit distortion has to be most suppressed in this operation.

3.11 Field measurement in off-median plane

The mapping measurement was also performed in off median plane (y=±15 mm). When the magnet has vertical symmetry, the field structures in the planes y=-15 mm and y=15 mm have to be identical. However, we found that the effective length in the plane y=15 mm differs from that in the plane of y=-15 mm. In Fig 3-48, the effective boundaries of the beam entrance side of magnet No. 15017 is shown. The effective length on the plane y=15 mm differs about 0.3 mm from that of y=-15 mm. It is difficult to explain this difference by the measurement error because the measurement error of the effective boundary was estimated to be 0.05 mm. Furthermore, the effective boundary of the other magnets showed the same tendency; the effective length becomes long, as the height of the mapping plane becomes lower.

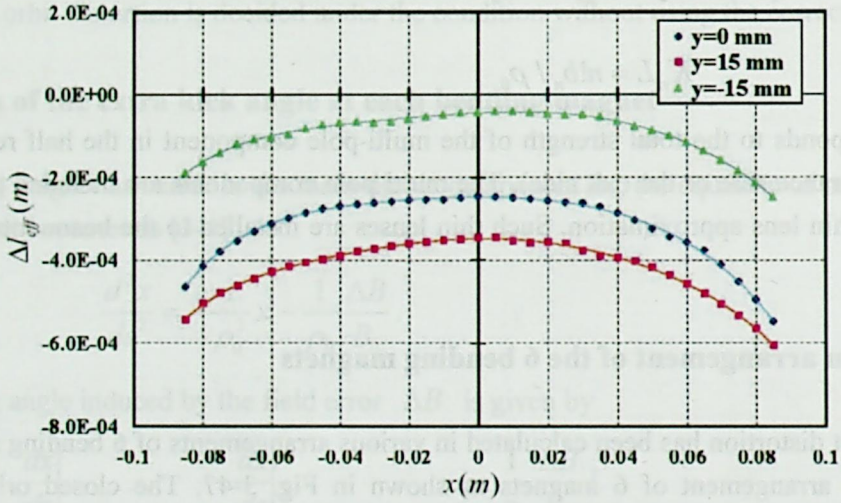

Fig. 3-48, The effective boundaries of the beam entrance side of magnet No. 15017. The effective length of y=15 mm and y=-15 mm are obviously difference. This is contrary to the requirement from the vertical symmetry of the magnet; the effective length of y=15 mm and y=-15 mm have to be same.

Then, we found the Hall probe had tilt angle in the longitudinal direction, as shown in Fig 3-49. Since the Hall-probe measures the field component perpendicular to the Hall-sensor, if the probe is tilt as shown in Fig. 3-49, the field strength which is sensed by the Hall probe differs by the height from the medial plane in the fringing field.

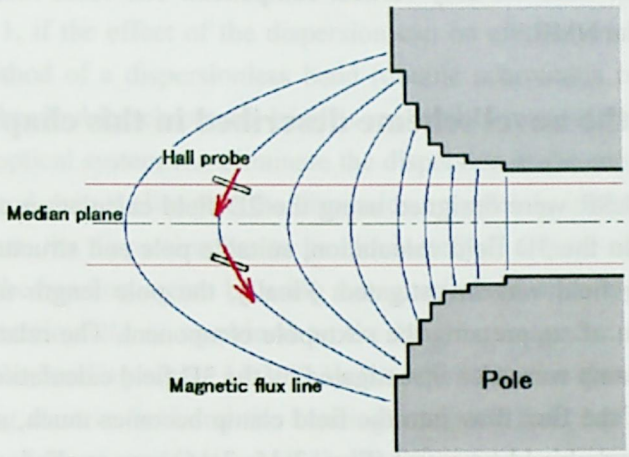

Fig. 3-49. Magnetic flux line in the fringing region.

In the case of our measurement, the Hall probe had tilt angle opposite to that of Fig. 3-49. Thus, the effective length measured by longitudinally leaned probe becomes longer as the height of the measurement plane becomes low. After the longitudinal tilt angle was corrected as small as possible, the difference of the effective length became very small. In Fig. 3-50, the effective boundaries of the beam exit side of magnet No. 15012 are shown. In this measurement a Hall-probe which is corrected the tilt angle are used. The difference of the effective length is suppressed less than 0.07 mm. These values almost agree within the measurement error. In this measurement, the mapping region was limited only in the fringing region, although, it is sufficient to see the height dependence of the effective boundary.

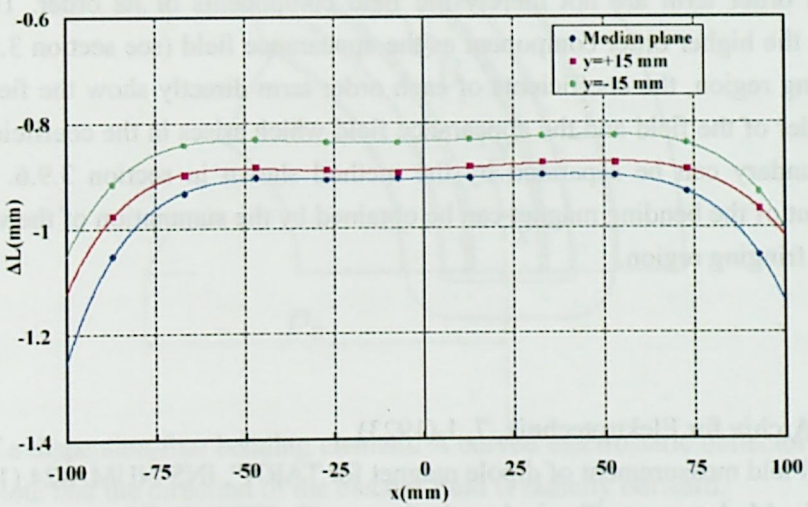

Fig. 3-50, The effective boundaries of the beam exit side of magnet No. 15012

Therefore, we can conclude that the cause of the height dependence of the measured effective length is longitudinal tilt angle of the Hall probe. If one will measure the effective length at off-median plane, one has to notice the longitudinal tilt angle of the Hall-probe.

Since the Hall-probe senses only the perpendicular field component to the sensor, the accuracy of the field

measured by Hall-probe in the region where more than two field components exist such as fringing region in off median plane, is not guaranteed, and it is important to correct the tilt angle of the probe accurately. In the case of the mapping measurement in the median plane, the small tilt angle of the probe did not become problem, since the magnetic field has only vertical component. The value read out from the Hall-probe is calibrated by the value of the NMR.

3.12 Summary of the novel scheme described in this chapter

Bending magnets for S-LSR were designed using the 2D field calculation code POISSON and 3D field calculation code TOSCA. In the 3D field calculation, suitable pole end structure to suppress the sextupole component of the fringing field was investigated. Finally, the pole length near the reference orbit was shortened with the intention of suppressing the sextupole component. The relation of the coil structure and the saturation of the field clamp were also investigated by the 3D field calculation. When the saddle type coil was applied, the amount of the flux flow into the field clamp becomes much, and the field clamp becomes easily saturated. When the combined type coil (Figs. 3-15, 3-16) was applied, saturation of the field clamp was suppressed.

The result of the field measurement showed that only one magnet has the large deviation of the BL product, among the six bending magnets. We corrected the effective length of this magnet by adjusting the position of the field clamp. The distance of the movement of the field clamp was expected from the 2D field calculation beforehand. The result of the field measurement of the corrected magnet agreed with the expectation by the 2D field calculation. Therefore, we can find that the 2D field calculation in the fringing field reproduces the actual state, near the reference orbit.

We have shown a method to estimate the total multi-pole component in a bending magnet. The information of the multi-pole components is obtained from the polynomial expansion of the effective boundary. In the calculation of the multi-pole component from the effective boundary, it was found that the coefficients of each order term are not merely the field components of its order. The lower order field component arises in the higher order component as the appearance field (see section 3.3.3.2) in the bending region. In the fringing region, the coefficients of each order term directly show the field components of its order. The actual order of the field and the appearance field which arises in the coefficients of the expansion of the effective boundary can be separated by the method shown in section 3.9.6. And the exact total multi-pole component of the bending magnet can be obtained by the summation of the value of the inner gap region and the outer fringing region.

References

[3-1] W. Rogowski, Archiv fur Elektrotechnik, **7**, 1 (1923)

[3-2] T. Hori et al., "Field measurement of dipole magnet for TARN", INS-NUMA-24 (1980)

[3-3] F. C. Iselin, "The Mad program Physical method manual", CERN/SL/92

[3-4] T. Kamei, M. Kihara "*Accelerator Science*" (Maruzen, Tokyo, 1993) [in Japanese]

[3-5] A. Morita, "performance assessment of a combined function type synchrotron based on an extremely precise field measurement" Dissertation; Department of Physics, Faculty of Science, Kyoto-University (2002)

[3-6] A. Morita, Y. Iwashita, A. Noda, T. Shirai, H. Tongu, M. Umezawa, K. Hiramoto, M. Tadokoro, Phys. Rev. ST-AB **4** 122401 (2001).

Chapter 4. Dispersion-free storage ring

4.1 Dispersionless bend

As discussed in chapter 1, if the effect of the dispersion can be eliminated, a 3D crystal beam structure may be stabilized. The method of a dispersionless bend (double achromatic bend) is often used in a low emittance radiation ring. The double achromatic bend is realized by a quadrpole magnet and two bending magnets [4-1]. Such beam optical system can eliminate the dispersion at the entrance and exit of the bending section. However, this method cannot eliminate the dispersion completely in the bending section. In order to stabilize the 3D crystal beam, the dispersion has to be eliminated all around of the ring. It is impossible to eliminate the dispersion at the bending region by using a magnetic field or an electric field only. On the other hand, if a bending electrostatic field is combined to the bending magnetic field, the dispersion can be eliminated at the whole of the bending region [4-2][4-3]. In order to realize the dispersion free bending field, the direction of the bending electric field and the bending magnetic field has to cross at right angle. This bending field can be realized by a combination of dipole magnet and an electrostatic deflector (Fig 4-1). When the beam has a central velocity $\mathbf{v}_0$, the relation between the bending electric field **E** and the bending magnetic field **B** is written by

$$\left(1+\frac{1}{\gamma_0^2}\right)\mathbf{E}(\rho_0) = -\mathbf{v}_0 \times \mathbf{B},$$

where γ_0 and ρ_0 denote the Lorentz factor and the bending radius of the beam, respectively.

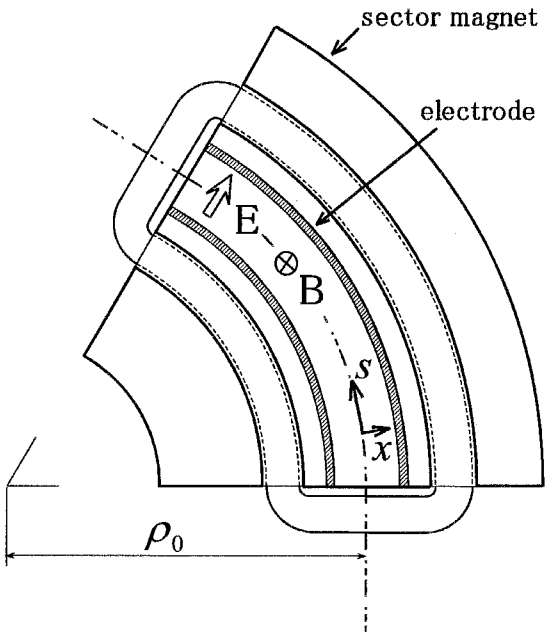

Fig. 4-1. Example of a dispersion-free bending element. A curved electrostatic deflector is installed in the gap of a dipole magnet. Note that the direction of the electric field is radially outward.

4.2 Dispersion suppresser

4.2.1 Formulation of the bending field

In the dispersion-free deflection element, if the ratio of the superposition of the electric field and the magnetic field is changed, it can create the situation in which the dispersion is suppressed. Thus in the

followings, we call generally the deflection element in which the dispersion is not eliminated completely, as a *dispersion-suppresser*. In this section, the equation of motion in the dispersion-suppresser is formulated in the Frenet-Serret coordinate system. The bending field of the dispersion-suppresser has to be the solution of Maxwell equation. We suppose the magnetic field is created by a flat pole dipole magnet. Then the vector potential can be written as

$$A_s = -\frac{B_y}{2}(\rho_0 + x), \tag{4-1}$$

The electric field is created by a cylindrical electrostatic deflector which is the simplest equal potential surface obtained from the solution of Maxwell equation, and such a electrostatic deflector is ordinarily used in an electrostatic storage ring [4-21]. Then the electric field and the electrostatic potential can be written as

$$E_x(x) = \frac{V_0}{\rho_0 + x} \tag{4-2}$$

$$\phi_D = -V_0 \cdot \ln\left(1 + \frac{x}{\rho_0}\right) = V_0 \cdot \sum_{n=1}^{\infty} \frac{(-1)^n}{n}\left(\frac{x}{\rho_0}\right)^n. \tag{4-3}$$

The direction of the bending electric field is opposite to the conventional electrostatic deflector, in order to compensate the dispersion.

4.2.2 Equation of motion

Hamiltonian of a dispersion-suppressor is derived in Frenet-Serret coordinate system [4-4]. Choosing the path length s as the independent variable, we obtain the relativistic Hamiltonian, that governs the motion of a charged particle in a bending region where not only a dipole magnetic field but also an electric field for dispersion compensation is present, of the form [4-5]

$$H = -\left(1 + \frac{x}{\rho_0}\right)\sqrt{\left(\frac{p_t + q\phi_D}{c}\right)^2 - m^2c^2 - p_x^2 - p_y^2} - q\left(1 + \frac{x}{\rho_0}\right)A_s, \tag{4-4}$$

where m and q are the rest mass and the charge state of particles, c is the speed of light, ϕ_D is the scalar potential in the electrostatic deflector, p_t is the longitudinal canonical momentum conjugate to time t, and we have assumed that the vector potential $\mathbf{A}$ only has the longitudinal component, i.e. $\mathbf{A} = (0, 0, A_s)$. By expanding the square root and leaving only low-order terms, Eq. (4-4) becomes

$$H = -\left(1 + \frac{x}{\rho_0}\right)qA_s - \left(1 + \frac{x}{\rho_0}\right)p + \frac{p_x^2 + p_y^2}{2p}, \tag{4-5}$$

where $p = m\beta\gamma c = \sqrt{(p_t + q\phi)^2/c^2 - m^2c^2}$ with β being the normalized velocity by the light speed c. This is good approximation when the transverse momenta p_x and p_y are far small compared to the longitudinal momentum. In a conventional beam transport line or an accelerator, this approximation is always effective. The scalar potential in the electrostatic deflector is given by Eq. (4-3) and the vector potential is given by Eq. (4-1). Note that the equilibrium kinetic momentum $p_0 (\equiv m\beta_0\gamma_0 c)$ is not equal to $qB_y\rho$ due to the existence of the bending electric field. Since the electric field strength is V_0 / ρ_0 along the design orbit, the equilibrium kinetic momentum becomes

$$p_0 = qB_y\rho_0 - \frac{qV_0}{\beta_0 c}. \tag{4-6}$$

The momentum deviation from the design momentum $p_0 = m\beta_0\gamma_0 c = \sqrt{E_0{}^2/c^2 - m^2c^2}$ can approximately be written as

$$\Delta p \equiv p - p_0 \approx \frac{\Delta E - q\phi_D}{\beta_0 c} - \frac{1}{2p_0}\left(\frac{\Delta E - q\phi_D}{\beta_0 c\gamma_0}\right)^2, \tag{4-7}$$

where ΔE is the energy deviation from the design value $-\Delta E = m\gamma_0 c^2 - (-p_t)$. This relation is obtained by taking up to the second order term of ΔE or $q\phi_D$. Inserting Eq. (4-1) and $p = p_0 + \Delta p$ into Eq. (4-5) and neglecting nonlinear terms, one finds

$$\tilde{H} = \frac{qV_0}{\beta_0^2 E_0}\frac{x}{\rho_0} + \frac{1}{2}\left(1 + \frac{qV_0}{\beta_0^2 E_0}\right)\left(\frac{x}{\rho_0}\right)^2 - \left(1 + \frac{x}{\rho_0}\right)\frac{\Delta p}{p_0} + \frac{\tilde{p}_x^2 + \tilde{p}_y^2}{2}, \tag{4-8}$$

where the transverse momenta have been scaled to be dimensionless; namely, $\tilde{p}_{x(y)} = p_{x(y)}/p_0$. Substitution of Eq. (4-7) together with Eq. (4-3) into Eq. (4-8) yields the approximate Hamiltonian

$$\tilde{H} = -\frac{\Delta E}{\beta_0^2 E_0}\frac{x}{\rho_0}\left(1 - \frac{qV_0}{\gamma_0^2\beta_0^2 E_0}\right) - \frac{\Delta E}{\beta_0^2 E_0} + \frac{1}{2\gamma_0^2}\left(\frac{\Delta E}{\beta_0^2 E_0}\right)^2 + \frac{\tilde{p}_x^2 + \tilde{p}_y^2}{2} + \left[1 + \frac{1}{\gamma_0^2}\left(\frac{qV_0}{\beta_0^2 E_0}\right)^2\right]\frac{x^2}{2\rho_0^2}, \tag{4-9}$$

From this Hamiltonian, we obtain the horizontal equation of motion in the bending region

$$\frac{d^2x}{ds^2} \approx -\left[1 + \frac{1}{\gamma_0^2}\left(\frac{qV_0}{\beta_0^2 E_0}\right)^2\right]\frac{x}{\rho_0^2} + \frac{1}{\rho_0}\left(1 - \frac{qV_0}{\gamma_0^2\beta_0^2 E_0}\right)\frac{\Delta E}{\beta_0^2 E_0}. \tag{4-10}$$

Clearly, the last term in the right hand side of Eq. (4-10) gives rise to linear dispersion, and its coefficient $1/\rho_0(1 - qV_0/\gamma_0^2\beta_0^2 E_0)$ decides the strength of the dispersion. It is thus possible to control momentum dispersion over a wide range by changing the electric and magnetic field strengths with the condition (4-6) fulfilled. In particular, dispersive effects can be minimized provided that

$$\frac{qV_0}{\gamma_0^2\beta_0^2 E_0} = 1, \tag{4-11}$$

which leads, by using Eq. (4-6), to $V_0/\rho = B_y \cdot [\beta c/(2-\beta^2)]$. This equation indicates that, when the beam energy is high, a very large voltage is needed to compensate dispersive effects. Therefore, the present dispersion suppressor is relevant only to low-energy beams. From Eqs. (4-6) and (4-11), we find $(1+1/\gamma_0^2)V_0/\rho_0 = B_y\beta_0 c$ that is identical to the dispersion-free bending condition described in section 4.1. When the dispersion-free condition (4-11) is satisfied, the horizontal equation of motion in the bending region becomes

$$\frac{d^2x}{ds^2} \approx -\frac{1+\gamma_0^2}{\rho_0^2} \cdot x, \tag{4-12}$$

where the horizontal motion has been decoupled from the longitudinal motion in linear approximation.

4.3 Application to a storage ring

For the transport of charged particles, dispersion-free deflection elements were proposed in [4-2] and [4-3]. But this scheme has never been used in the design of synchrotrons and storage rings up to now, because the

required electric fields become too large for particle beams used in these accelerators. We propose the possibility of incorporating this scheme in a low energy storage ring. In this section, we show some characteristics of a storage ring constructed with dispersion-suppressors.

4.3.1 Hamiltonian of a storage ring

A beam circulating in a dispersion-free storage ring receives only the alternating focusing force, thus, one can expect the beam dynamics of the dispersion free ring coincides with that of a linear beam transport line or a linear ion trap. In this section, the Hamiltonian of the storage ring constructed with dispersion-suppressors is investigated. Here, a separated function type lattice is assumed. When quadrupole magnets and an rf cavity are taken into account in addition to dispersion-suppressors, the vector potential becomes

$$A_s = -\frac{B_y}{2}(\rho + x) + \frac{1}{2}B_1(x^2 - y^2) + \delta_p(s)\frac{V_{RF}}{\omega}\cos(\omega t + \phi_0) \tag{4-13}$$

where B_1 is the gradient of the quadrupole field. V_{RF} and ϕ_0 are a voltage amplitude and an initial phase of the rf cavity, respectively. Since a storage ring is considered now, the rf frequency ω is constant and $\omega = h\omega_0$, where ω_0 is the angular revolution frequency of the synchronous particle and h is the harmonic number. The rf cavity is installed at the straight section of the coordinate $s = 0$.
When Eq. (4-13) and $p = p_0 + \Delta p$ are inserted into Eq. (4-5) and nonlinear terms are neglected, one finds

$$\begin{aligned}\tilde{H} = &-\frac{\Delta E}{\beta_0^2 E_0}\frac{x}{\rho}\left(1 - \frac{q\kappa}{\gamma_0^2\beta_0^2 E_0}\right) - \frac{\Delta E}{\beta_0^2 E_0} + \frac{1}{2\gamma_0^2}\left(\frac{\Delta E}{\beta_0^2 E_0}\right)^2 + \frac{\tilde{p}_x^2 + \tilde{p}_y^2}{2} + \frac{1}{2}\left(K_x x^2 + K_y y^2\right) \\ &- \delta_p(s)\frac{qV_{RF}}{p_0\omega}\cos(\omega t + \phi_0)\end{aligned} \tag{4-14}$$

where

$$K_x = \frac{1}{\rho^2}\left[1 + \frac{1}{\gamma_0^2}\left(\frac{q\kappa}{\beta_0^2 E_0}\right)^2\right] - \frac{qK_1}{p_0}, \qquad K_y = \frac{qK_1}{p_0}.$$

ρ, κ, and K_1 are function of s; $\rho = \rho_0$, $\kappa = V_0$ in the bending region, and $\rho = \infty$, $\kappa = 0$ in the other regions. K_1 is B_1 in the quadrupole magnet region, and $K_1 = 0$ in other regions. If Hamiltonian (4-14) is compared to that of the conventional magnetic storage ring Eq. (1-30), one can find that the difference arises in the first term (shear term).

4.3.2 Effect of the electrostatic potential

The electrostatic potential of the dispersion-suppressor causes the energy transfer between kinetic energy and potential energy of charged particles while conserving the total energy. Here, the total energy means summation of the kinetic energy and potential energy, and it corresponds to E in the notation used in this thesis. One can find that ΔE is also an approximate constant of motion, if the rf voltage is not imposed (see Eq. (4-14)). On the other hand, the kinetic energy and the momentum may not be constant, in contrast with a conventional magnetic storage ring.

Suppose an ion beam is strongly cooled by a cooling force in a storage ring. If the design orbit is linear, the momentum spread eventually vanishes, i.e. $\Delta p = 0$, at low temperature limit where the beam is Coulomb

crystallized. As shown in Ref [4-6], [4-7], when the density of the beam is low, crystalline structure is a 1D chain. If the density is larger than the 1D state, a 2D crystalline structure is developed in the weaker focusing direction. If the density is enhanced more, the particles naturally arrange into a 3D crystal structure, and the beam has a finite horizontal extent. In an ordinary storage ring, however, the condition $\Delta p = 0$ does not meet the stability requirement of a crystalline state with a finite horizontal extent because the bending magnets generate the shearing force; as briefly discussed in chapter 1, a radially outer particle must travel slightly faster than the inner particles, so as to realize a condition such that the angular velocities of all particles, rather than the linear velocity, are identical. The stability of a multi-dimensional crystalline beam is, therefore, not guaranteed unless the cooling force is "tapered" [4-8]. By contrast, the present dispersion-free system can compensate the difference of the angular velocities even if the cooling force is not tapered, because of the above energy transfer mechanism. However, in order to realize this condition, it is essential that the ring has a straight section, in addition to satisfying a dispersion free condition. The reason is as follows.

First, for pedagogical purpose, we consider a dispersion-free ring with a constant bending field i.e. the whole circumference of the ring is occupied by the bending element. The cooling force acts so that the momentum spread approaches to zero, and the momentum is almost constant in this ring, like that of conventional rings. If the beam has finite horizontal extent, this situation is not suitable for the condition of 3D crystal beam; namely, all particles don't have the same "angular" momentum. This ring is merely dispersion-free.

Next, we consider a dispersion-free ring which has straight sections. In such a ring, the momentum is not constant because of the acceleration (or deceleration) of the charged particle at the entrance (or exit) of the bending section. The relation between the deviation of the total energy ΔE and the momentum deviation Δp is given by Eq. (4-7). If a beam is cooled at a straight section, the momentum deviation Δp becomes zero and the energy deviation ΔE also becomes zero because of the zero scalar potential. When a beam with a finite horizontal extent enters into the bending region, the particles receive some kinetic energy gain (loss) from the deflection electric field in exchange for loss (gain) of the potential energy. The amount of the gain depends on the horizontal coordinate x. When $|x/\rho_0| \ll 1$, Eq. (4-3) gives $\phi_D \approx -V_0 \cdot x/\rho_0$ and, accordingly, the potential along an inner orbit is higher than that along an outer orbit; in other words, a particle traveling in the region of negative x (positive x) is decelerated (accelerated) at the entrance of the electrostatic deflector. At the exit, the opposite effect takes place, and the particle recovers the original kinetic energy before entering the bending region. Now, ΔE is zero, because of the cooling at the straight section, and it is zero all around of the ring, since it is constant of motion. Then, if once an ideal ground state [4-9] is reached, from Eq. (4-7), one obtain the relation $p \approx p_0 + (qV_0/\beta_0 c\rho_0)\cdot x$. This relation can be rewritten, with the condition (4-11), as $p/p_0 \approx 1 + \gamma^2 x/\rho_0$ or, equivalently,

$$\frac{v}{v_0} \approx 1 + \frac{x}{\rho_0}, \tag{4-15}$$

where v denotes the velocity of a particle at the horizontal position x, and $v_0 = \beta_0 c$. It is now evident that the angular velocities of all particles are approximately the same. We can thus suggest that the stability of a three-dimensional crystalline beam is greatly improved in the dispersion-free storage ring presented in this thesis.

Even if the storage ring satisfy the dispersion-free condition, making particles to have the same angular velocity is impossible without the straight section. Thus, it is essential to "cool at the straight section (which

has no electrostatic potential)" and to cause the acceleration (or deceleration) of the charged particle at the entrance (or exit) of the bending section.

4.3.3 Analytical treatment of the shearing force

As shown in previous subsection, the effect of acceleration (or deceleration) at the boundary of the bending section plays an important role. This effect is included in the Hamiltonian formalism automatically in this thesis. Therefore, we can show these effects analytically. The first term of the Hamiltonian (4-14) yields dynamic coupling between the horizontal coordinates and longitudinal momenta. From the derivation process of the horizontal equation of motion (4-10), one finds this *shear term* [4-10] generates the dispersion term of the equation of motion. As shown in section 1.5.3, the shear term also generates the shearing force. Here, in order to show the effect of the shear term explicitly, the rf cavity is switched off. When the relative time $\Delta t = t - s/\beta_0 c$ is introduced, from the Hamiltonian (4-14), the longitudinal equations of motion are given by

$$\frac{d(\Delta t)}{ds} = \frac{1}{\beta_0 c}\left[\frac{x}{\rho}\left(1 - \frac{q\kappa}{\gamma_0^2\beta_0^2 E_0}\right) - \frac{1}{\gamma_0^2}\left(\frac{\Delta E}{\beta_0^2 E_0}\right)\right] \tag{4-16}$$

$$\frac{d}{ds}\left(\frac{-\Delta E}{p_0}\right) = 0, \tag{4-17}$$

The first term of the right hand side of the equation (4-16) represents the shearing force, and it is generated from the shear term. The second term represents the difference of the revolution time caused by the energy deviation. According to Eq. (4-16), in a crystalline state (where ΔE=0, it is constant in the ring) with a finite horizontal extent x, the difference of the revolution time is dominated by the shearing force and its strength is proportional to the strength of the dispersion $1/\rho(1 - qV_0/\gamma_0^2\beta_0^2 E_0)$.

For the dispersion-free condition (4-11), the shearing force canceled out and the revolution time doesn't depend on the horizontal extent of the beam, x. Therefore, in a storage ring constructed with dispersion-suppressors, the cancellation of the shearing force is synonymous with the cancellation of the dispersion.

The shear term is caused by the geometric factor of bending; namely, this term exists because of the finite bending radius ρ. This term causes crucial difference between the Hamiltonians of the storage ring and linear ion trap. Fortunately, this term is canceled out at the dispersion free condition. Then, although there are bending sections, the dynamics of the particle becomes the same as straight section.

In the dispersion-free condition, the Hamiltonian (4-14) becomes equivalent to the Hamiltonian of rf linear ion trap in which the ions are restricted to a finite length. Therefore, the beam behavior in the dispersion-free ring, except for higher-order nonlinear terms, is similar to that in a linear ion trap in which multi-dimensional crystal structure has been observed experimentally [4-11]. The discussion about nonlinear terms is performed in Section 4.8.

4.3.4 Effect of the rf cavity

In this section, the effect of the rf cavity is taken into account. When the periodic delta function $\delta_p(s)$ is expanded in a Fourier series, we obtain the expression [4-12]

$$\delta_p(s)\cos(\omega t+\phi_0)\approx\frac{1}{C}\cos(\omega t-\frac{2\pi hs}{C}+\phi_0) \tag{4-18}$$

where C is the length of reference orbit in the ring. If the relation $\beta_0 c=\omega_0 C/2\pi$ is utilized, the phase of Eq. (4-18) can be expressed as

$$\omega t-\frac{2\pi hs}{C}+\phi_0=\omega\Delta t+\phi_0 \tag{4-19}$$

Then, only the longitudinal equation of motion (4-17) is corrected by the effect of the rf cavity.

$$\frac{d(\Delta E)}{ds}=\frac{qV_{RF}}{C}\sin\phi \tag{4-20}$$

where the synchrotron phase $\phi=\Delta\phi+\phi_0=\omega\Delta t+\phi_0$ is introduced. In the followings, the initial phase of the rf cavity ϕ_0 is set to zero so that the reference particle may not have energy gain and synchrotron oscillation. Then, Eq. (4-20) gives an energy change so that the particles which are deviated from the design phase experience oscillation.

In a low beam current limit in which the space charge effect is negligible, the longitudinal equation of motion of the dispersion-free storage ring becomes the synchrotron equation which has phase slip factor $\eta=-1/\gamma_0^2$. Thus the synchrotron oscillation is stable. This result is reasonable, because the phase slip factor is defined by $\eta=\alpha-1/\gamma_0^2$ and the momentum compaction factor of the dispersion-free ring is zero; $\alpha=1/C\oint D_x(s)/\rho(s)\,ds=0$. Here $D_x(s)$ is horizontal dispersion function of the ring, and it is zero all around the dispersion free ring. This result means the dispersion-free ring has infinite high transition energy $\gamma_t=1/\sqrt{\alpha}$.

As shown in Section 1.5.2, there are so-called *maintenance conditions* for realization of a crystal beam in a storage ring. First maintenance condition is that the beam energy must be below the transition energy; $\gamma<\gamma_t$. The second condition is $N>2\sqrt{2}\nu_T$, where N is the number of the super period of the ring, and ν_T is the transverse tune. The dispersion-free ring satisfies the first condition in principle. If the dispersion-free storage ring has a larger number of super periods or a large bending radius, it is thought to satisfy the second condition in general. Consideration of the second maintenance condition is described in Section 4.6.2.

In the followings, we consider the crystalline state, in order to explain analytically the heating mechanism of the crystalline beam induced by the dispersion. In a 3D crystalline state, betatron oscillation is strongly suppressed, and the particles no longer oscillate across the reference orbit. This means such particles always have the same sign of x in Eq. (4-16). If a bunched 3D crystalline beam continues to be cooled by a cooling force in the straight section, the energy spread ΔE of Eq. (4-16) approaches zero. But, in the bending region, the deviations of the synchrotron phases $\Delta\phi=\omega\Delta t$ of radially outer and inner particles are increased because of the first term of Eq (4-16) (shearing force), if the dispersion-free condition is not satisfied. This increase of the synchrotron phase deviation $\Delta\phi$ affects the energy spread ΔE through Eq. (4-20). Eventually, the energy spread is extended by the rf potential through Eq. (4-20). Finally, this heating rate balances with the cooling rate of the cooling force. Because of such a mechanism, the reachable temperature of the 3D crystalline beam is limited.

In the dispersion-free condition, this heating mechanism is completely suppressed due to the cancellation of the first term of Eq. (4-16), and, the stability of the 3D crystalline beam is greatly improved. In this state, the energy spread ΔE of the final equibrium state becomes zero. As shown in Ref. [4-13], the synchrotron oscillation of the crystalline beam is strongly suppressed despite the finite bunch length (finite phase deviation $\Delta\phi$). This is the same reason as the suppression of the betatron oscillation of a 3D crystalline

beam which has a finite transverse extent. Thus, the synchrotron motion of the 3D crystalline beam is suppressed completely.

In order to realize a strong three-dimensional laser cooling, the method of utilizing a synchro-betatron coupling induced by the rf cavity [4-14] has been proposed. However, in the dispersion-free storage ring, it is difficult to generate synchro-betatron coupling by a normal rf cavity, because there is no dispersion. In the dispersion-free case, we can use a *coupling rf cavity* [4-15], [4-13] for the 3D cooling. The coupling rf cavity scheme realizes the synchro-betatron coupling by using a special mode of the rf electric field which depends on the transverse position. For a low energy storage ring, even in the dispersion-free case, the coupling rf cavity can create the enough coupling strength for 3D cooling. The energy transfer between longitudinal motion and transverse motion becomes comparable, in order, to that of the energy of the laser photon for cooling, by reasonable applied voltage to the coupling-cavity.

4.4 Design of the dispersion-suppresser for S-LSR

Dispersion-free deflector or dispersion suppresser has never been constructed. The first proposal of the dispersion-free deflector [4-2], [4-3] is application to mass-analyze. However, it has been difficult to construct a deflection element as shown in Fig. 4-1, because the electric field of the electrostatic deflector is reduced by the influence of the wall of the vacuum vessel or the pole of the bending magnet. Furthermore, the result that the particles are bent with the same angle not depending on the kinetic energy is also realized by the independent use of the bending electric field and magnetic field [4-16]. The construction of the beam line for mass-analyze by setting the electrostatic deflector and the bending magnet independent position is easier than the insertion of the electrostatic deflector to the gap of the bending magnet. From the above

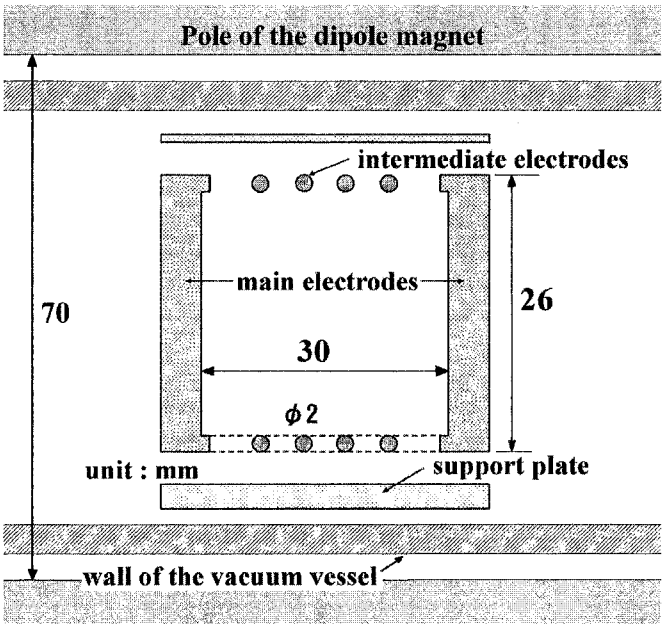

Fig 4-2. Cross-section around the electrostatic deflector. The height of the electrostatic deflector is limited by the gap size of the dipole magnet and the vacuum vessel. The electrostatic deflector is constructed by a pair of main electrodes and four pairs of intermediate electrodes. The ideal field distribution is maintained by the intermediate electrodes. In addition to the electrodes, support plates and ceramic plates are introduced for the purpose of keeping the position of the electrodes.

reason, such deflection element as a dispersion-suppresser has never been constructed. But now, the use of the dispersion-suppresser is essential for the stabilization of the 3D crystal beam structure.

In order to realize the dispersion-suppresser, an electrostatic deflector has to be installed in the gap of the dipole magnet of S-LSR. Therefore, the height of the electrostatic deflector is limited. In a conventional case, the height of the electrostatic deflector is secured enough, in order to avoid the reduction of the strength of the electric field due to the leak of the lines of electric force. In the case of S-LSR, in stead of the enhancement of the height of the electrodes, intermediate electrodes are introduced to maintain the strength and the distribution of the electric field (Fig. 4-2).

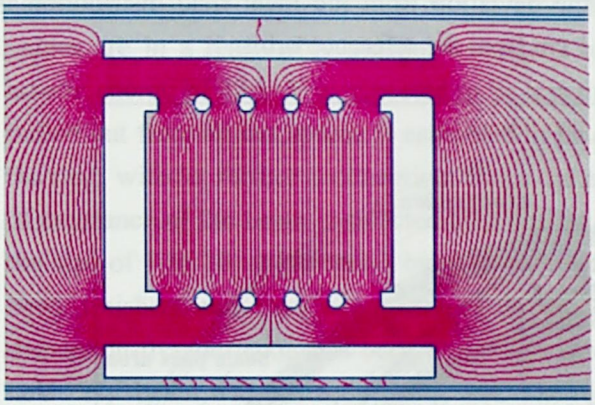

Fig 4-3-a.

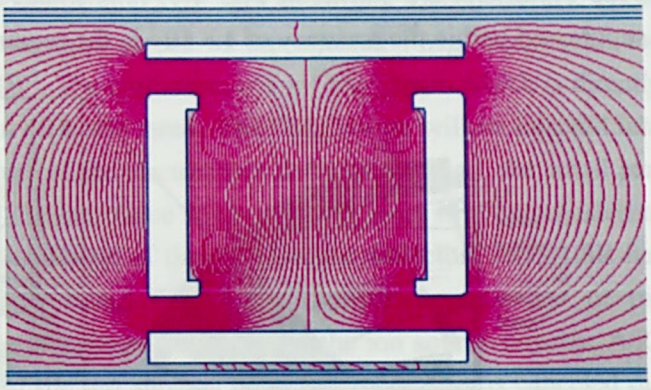

Fig 4-3-b.

Equal potential surfaces around the electrostatic deflector

Comparing Figs. 4-3-a and Fig. 4-3-b which are result of the electrostatic field calculation, it is found that the intermediate electrodes maintaining the field strength and the distribution near the center of the aperture. The pink lines represent the equal potential surface. If there is no intermediate electrode (Fig 4-3-b) the interval of the equal potential surface line changes by the height in the electrostatic deflector. This means the bending field strength and the distribution changes by the height of the beam pass. In Fig 4-3-b, it is also found that interval of the equal potential surface line becomes wider compared with that of near the main

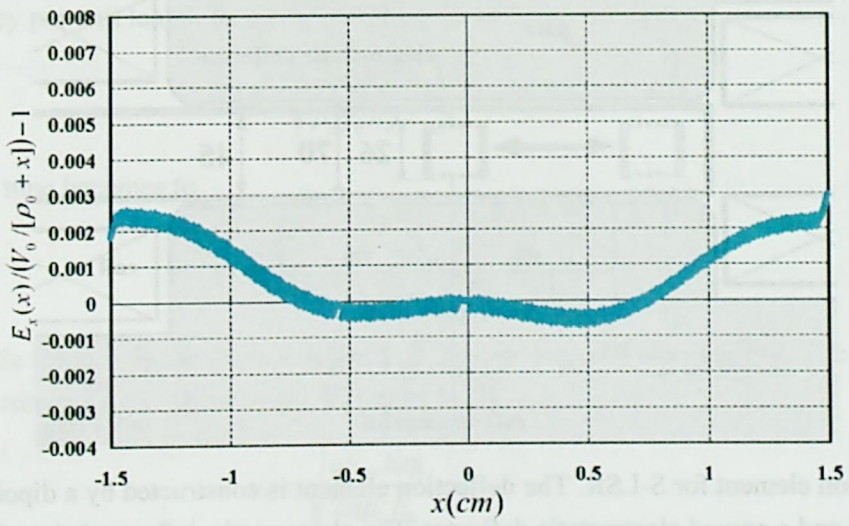

Fig. 4-4. The deviation of the redial field distribution from the ideal distribution, in the electrostatic deflector.

electrodes. This means that the field strength is weakened due to the upper and lower conductor plats attached for maintaining the interval of the main electrode. Furthermore, it is difficult to generate the enough strong bending electric field, with the structure shown in Fig 4-3-b.

As the horizontal aperture of the electrostatic deflector becomes wider, it becomes better for the beam injection and circulation. However, even if the intermediate electrodes are introduced, when the horizontal aperture becomes larger, the deviation of the radial distribution of the field from the ideal distribution becomes larger and many intermediate electrodes are required. Finally, the horizontal aperture has been determined as 30mm compromising the available aperture for beam injection or circulation and the deviation of the radial distribution of the electric field. The radial field distribution calculated by 2D field calculation code POISSON are shown in Fig. 4-4. It is found that the deviation from the ideal field distribution is suppressed within the accuracy of 1×10^{-3} in the region ± 1 cm from the reference orbit.

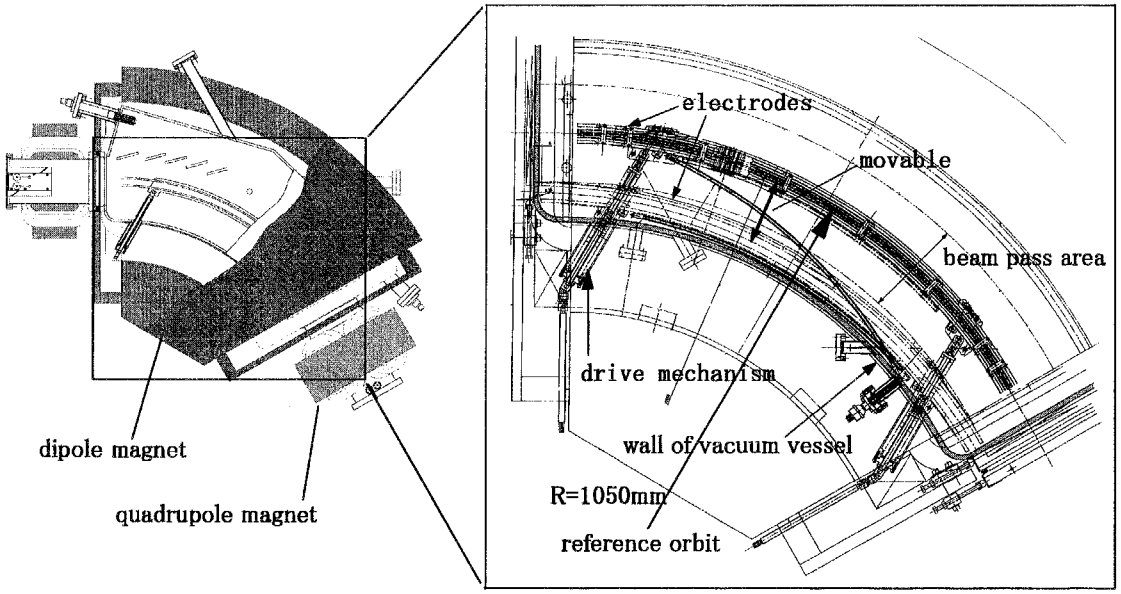

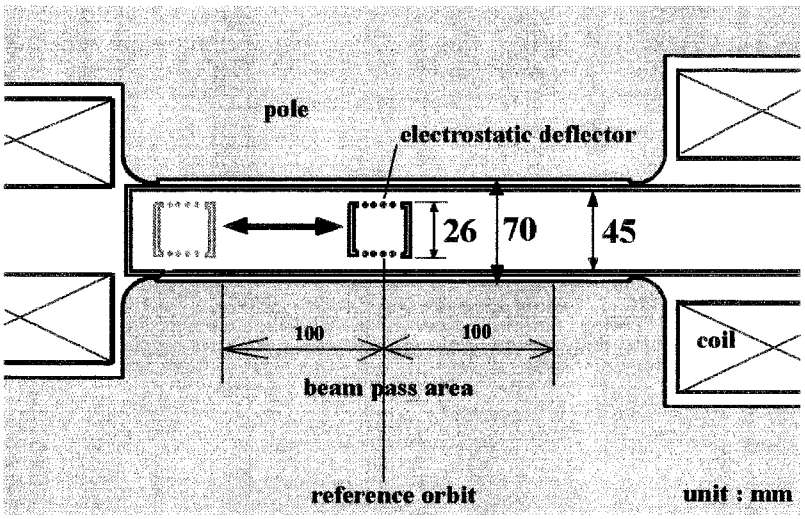

Fig 4-5. Deflection element for S-LSR. The deflection element is constructed by a dipole magnet which has no field gradient and a curved electrostatic deflector. The electrostatic deflector is installed in the gap of the dipole magnet. The electrostatic deflector can be moved out, when the deflection element is used as a normal dipole magnet

S-LSR has to be used as not only dispersion-free ring but also a conventional magnetic storage ring. When the power supply of the electrodes is switched off, S-LSR can be used as a magnetic storage ring. However, this is contradicting to the design principle of the magnetic mode of S-LSR, because the horizontal and the vertical aperture are limited to only 30 mm and 26 mm, respectively. In order to manage both a wide horizontal aperture magnetic storage ring and a dispersion-free ring with a precise bending electric field, the mechanism to move the electrostatic deflector from the reference orbit to the shunting station has been introduced (Fig 4-5).

As a possible application of the dispersion-free operating mode, the laser cooling of a $^{24}Mg^{+}$ beam is planned. The kinetic energy of the $^{24}Mg^{+}$ beam is supposed to be 35 keV. The electric and magnetic fields needed for dispersion-free storage of a 35 keV $^{24}Mg^{+}$ beam are $6.7\text{x}10^{4}$ V/m and 0.252 T, respectively. These values are in a reasonably attainable range. The momentum spread of the injected $^{24}Mg^{+}$ beam with the kinetic energy of 35 keV is expected to be less than 10^{-3}. The emittance of the $^{24}Mg^{+}$ beam which is directly pulled out from an ion source is estimated to be about 40π mm mrad. The $^{24}Mg^{+}$ beam will be injected into the ring, without further acceleration. Since the aperture of the electrostatic deflector is small, the small part of emittance of the beam is selected by a double slit. The emittance of the injected beam is to be adjusted to the size of 1 to 10 π mm mrad by the double slit. The design of the electrostatic deflectors for S-LSR has been finished and they are installed to the vacuum vessel Fig (4-5). The performance test of the dispersion-free deflector has been performed by using a beam pulled out from the ion source directly. A 25 keV $^{14}N_2^{+}$ beam was utilized for this test. The result of the test showed the linear dispersion is canceled out with good precision, when the strength of the bending magnetic field and the electric field satisfy the dispersion-free condition [4-23].

4.5 Synchrotron motion of the dispersion-free mode

The equation of the synchrotron motion of the dispersion-free ring is derived from Eqs. (4-16) and (4-20). For a particle near the bottom of the rf bucket ($\omega\Delta t << 1$), the synchrotron equation can be written as

$$\frac{d^2\phi}{ds^2} = -\frac{qV_{RF}\omega}{\beta_0^3 c\gamma_0^2 E_0 C}\phi = -\frac{2\pi q V_{RF} h}{\beta_0^2\gamma_0^2 E_0 C^2}\phi \tag{4-21}$$

The angular frequency per unit length is

$$\Omega = \sqrt{\frac{2\pi q V_{RF} h}{\beta_0^2\gamma_0^2 E_0 C^2}}, \tag{4-22}$$

thus the synchrotron tune becomes to

$$\nu_S = \frac{\Omega C}{2\pi} = \sqrt{\frac{qV_{RF}h}{2\pi\beta_0^2\gamma_0^2 E_0}} \tag{4-23}$$

Here, we can find this formula is the expanded form of the conventional storage ring. The synchrotron tune of the conventional storage ring is given by the formula [4-17]

$$\nu_S = \sqrt{\frac{qV_{RF}h|\eta|}{2\pi\beta_0^2 E_0}} \tag{4-24}$$

where η is phase slip factor of the ring. As shown in Section 4.3.4, the phase slip factor of the dispersion

free ring is $-1/\gamma_0^2$. The absolute value of η of the magnetic mode of S-LSR is usually less than 1, on the other hand that of the dispersion-free mode is always $\eta=-1$. Therefore, at the dispersion-free condition, the rf voltage or the harmonic number required for the same synchrotron-tune is rather lower than that of the magnetic mode.

4.6 Transfer matrix formula

4.6.1 Formulation of the transfer matrix

In this section, the lattice parameters of S-LSR are calculated by the transfer matrix analysis [4-18]. The transfer matrix acts on the phase space coordinates $(x,\tilde{p}_x,y,\tilde{p}_y,-c\Delta t,W)$, where $W=\Delta E/\beta_0 E_0$. The transfer matrix of the dispersion-suppressor is derived by solving the canonical equation from Hamiltonian (4-9). From the horizontal and the vertical equation of motion the following relations are obtained

$$\frac{\partial x}{\partial s}=\frac{\partial \tilde{H}}{\partial \tilde{p}_x}=\tilde{p}_x \qquad \frac{\partial y}{\partial s}=\frac{\partial \tilde{H}}{\partial \tilde{p}_y}=\tilde{p}_y \tag{4-25}$$

Therefore, in this notation, the slopes x',y' coincide with the normalized canonical momenta $\tilde{p}_x,\tilde{p}_y$; $x'=\tilde{p}_x$, $y'=\tilde{p}_y$. By solving the horizontal equation of motion (4-10) the following solution is obtained

$$x=x_0\cos\sqrt{k}s+\tilde{p}_{x0}\frac{1}{\sqrt{k}}\sin\sqrt{k}s+W\frac{1}{\beta_0}\frac{d}{k}(1-\cos\sqrt{k}s) \tag{4-26}$$

$$\tilde{p}_x=-x_0\sqrt{k}\sin\sqrt{k}s+\tilde{p}_{x0}\cos\sqrt{k}s+W\frac{1}{\beta_0}\frac{d}{\sqrt{k}}\sin\sqrt{k}s \tag{4-27}$$

where x_0 and $\tilde{p}_{x0}$ is the initial value, and the following notations have been introduced to simplify the formula.

$$k=\left[1+\frac{1}{\gamma_0^2}\left(\frac{qV_0}{\beta_0^2E_0}\right)^2\right]\frac{1}{\rho_0^2} \qquad d=\left(1-\frac{qV_0}{\gamma_0^2\beta_0^2E_0}\right)\frac{1}{\rho_0} \tag{4-28}$$

The vertical equation of motion is same as that of the drift space. The longitudinal canonical equations are given by Eqs. (4-16) and (4-17). If Eq. (4-26) is substituted to Eq. (4-16), the equation about $-c\Delta t$ is obtained.

$$\frac{d(-c\Delta t)}{ds}=-\frac{1}{\beta_0}\left[x_0 d\cos\sqrt{k}s+\tilde{p}_{x0}\frac{d}{\sqrt{k}}\sin\sqrt{k}s+W\frac{1}{\beta_0}\frac{d^2}{k}(1-\cos\sqrt{k}s)-W\frac{1}{\gamma_0^2\beta_0}\right] \tag{4-29}$$

This differential equation can be solved, and the solution is

$$-c\Delta t=-x_0\frac{1}{\beta_0}\frac{d}{\sqrt{k}}\sin\sqrt{k}s+\tilde{p}_{x0}\frac{1}{\beta_0}\frac{d}{k}\cos\sqrt{k}s-W\frac{1}{\beta_0^2}\frac{d^2}{k}\left(s-\frac{1}{\sqrt{k}}\sin\sqrt{k}s\right)+W\frac{1}{\gamma_0^2\beta_0^2}s+const \tag{4-30}$$

The initial condition decides the value of the constant in Eq. (4-30), and the solution of the longitudinal motion becomes to

$$-c\Delta t=-x_0\frac{1}{\beta_0}\frac{d}{\sqrt{k}}\sin\sqrt{k}s-\tilde{p}_{x0}\frac{1}{\beta_0}\frac{d}{k}(1-\cos\sqrt{k}s)-W\left[\frac{1}{\beta_0^2}\frac{d^2}{k}\left(s-\frac{1}{\sqrt{k}}\sin\sqrt{k}s\right)-\frac{1}{\gamma_0^2\beta_0^2}s\right]-c\Delta t_0 \tag{4-31}$$

From the above relations, the linear transfer matrix is derived
In this transfer matrix, L denotes the path length of the reference particle in the dispersion-suppresser.

$$M=\begin{pmatrix} \cos\sqrt{k}L & \frac{1}{\sqrt{k}}\sin\sqrt{k}L & 0 & 0 & 0 & \frac{1}{\beta_0}\frac{d}{k}(1-\cos\sqrt{k}L) \\ -\sqrt{k}\sin\sqrt{k}L & \cos\sqrt{k}L & 0 & 0 & 0 & \frac{1}{\beta_0}\frac{d}{\sqrt{k}}\sin\sqrt{k}L \\ 0 & 0 & 1 & L & 0 & 0 \\ 0 & 0 & 0 & 1 & 0 & 0 \\ -\frac{1}{\beta_0}\frac{d}{\sqrt{k}}\sin\sqrt{k}L & -\frac{1}{\beta_0}\frac{d}{k}(1-\cos\sqrt{k}L) & 0 & 0 & 1 & -\frac{1}{\beta_0^2}\frac{d^2}{k}\left(L-\frac{1}{\sqrt{k}}\sin\sqrt{k}L\right)+\frac{L}{\beta_0^2\gamma_0^2} \\ 0 & 0 & 0 & 0 & 0 & 1 \end{pmatrix} \tag{4-32}$$

4.6.2 Lattice parameters of dispersion-free mode

First, the stable region of the betatron oscillation is calculated. For the dispersion-free condition, the stable region is shown in Fig. 4-6. The field gradient of QM1 and QM2 (k_1 and k_2) in Fig. 2-2 are used as the parameters. The field gradient k_1 and k_2 are normalized by the magnetic rigidity of the 35 keV $^{24}Mg^+$ beam; $k = B_1 / B_0\rho_0$. The stable region of betatron oscillation is drawn by selecting a region which satisfies the condition that the absolute value of the trace of the transverse transfer matrix of one super period is less than 2.

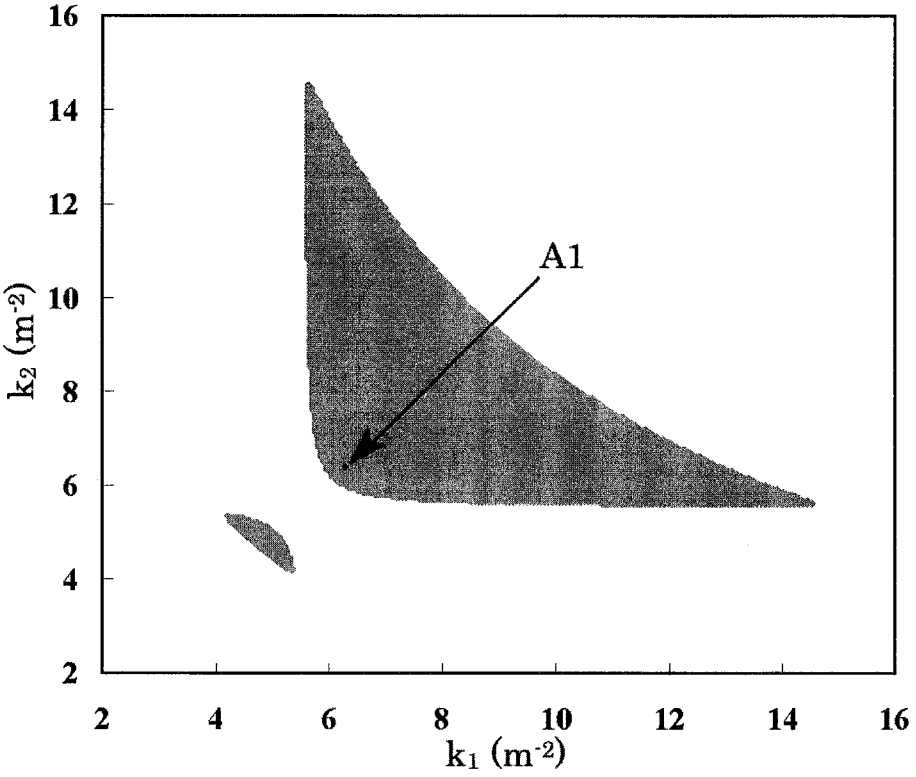

Fig. 4-6. The stable region of the betatron oscillation. The stable region is plotted on the focusing or defocusing quadrupole plane. The beta-functions of the operating point A1 are given in Fig. 4-8.

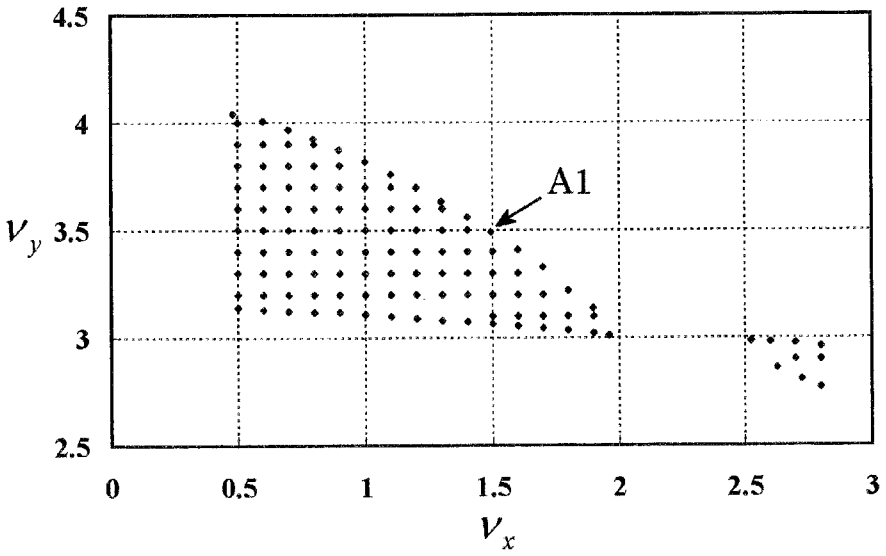

Fig. 4-7. The tune values corresponding the operating points of Fig 4-6

At the operating point A1 of Fig. 4-6, the betatron tunes become (1.49, 3.49), and the value of the beta functions becomes minimum in the stable region. The beta-functions of this operating point are shown in Fig. 4-8 as the functions of the position s along the reference orbit. The lattice parameters of the operating point A1 are compared to that of using only magnetic field. In the case of only magnetic field, the horizontal and vertical tunes are selected to (1.44, 1.44). In this case, beta functions become as shown in Fig. 4-9.

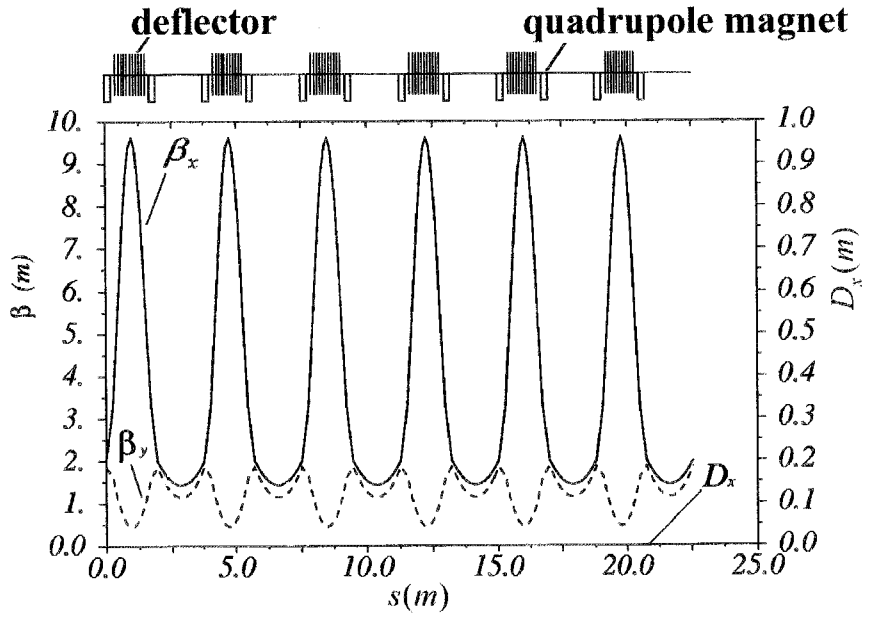

Fig. 4-8. Beta-functions of the operating point A1 of Fig. 4-6. The tune values are (1.49, 3.49). The beta-functions are drawn as a function of the position s. The position of the deflectors and quadrupole magnets are shown in the above diagram. D_x is the horizontal dispersion function.

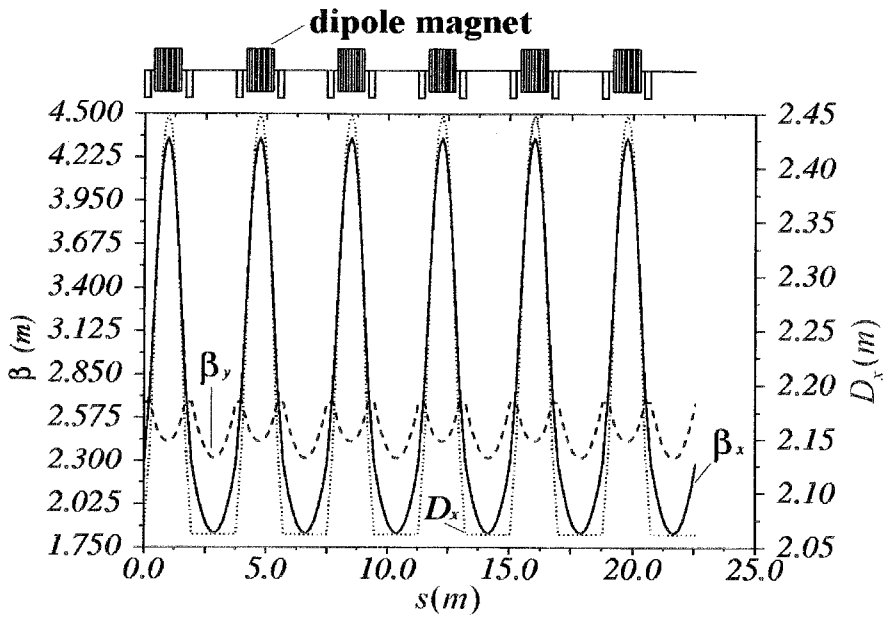

Fig. 4-9. Beta-functions as a function of the position s. In this case deflection elements are used as conventional dipole magnets. The betatron-tune are (1.44, 1.44).

We have found that at almost all the usable operation point, the dispersion-free case has a larger β_x than in the magnetic case and the vertical tune is enhanced. The reason for this can be found from Eqs. (4-6) and (4-10). One finds that the radial focusing of the dispersion-suppressor can be controllable without changing the bending radius by changing the ratio of the two bending field, and at the dispersion-free condition, the radial focusing has twice the strength of that of the dipole magnet. In S-LSR, the radial focusing of the deflection element is utilized for the horizontal focusing. Thus, the betatron motion of the beam is greatly affected by the radial focusing strength of the deflection element. In the horizontal direction, the strength of the defocusing of the quadrupole magnet has to be increased, in order to compensate the increase of the radial focusing. Naturally, in connection with it, the focusing strength of the quadrupole magnet in the vertical direction becomes large. Because of such reasons, the betatron tune, especially the vertical tune of the dispersion-free mode is increased. Thus, as shown in Fig 4-7, the tune value satisfying the second maintenance condition doesn't exist in the stable operating point of S-LSR

The lattice design of S-LSR had been designed to satisfy the two maintenance conditions for the crystalline structure, in the magnetic mode [4-19]. The dispersion-free mode of S-LSR has advantage in the cancellation of the shear heating mechanism, although the second maintenance condition for crystal beams is not satisfied. Therefore, in order to achieve a crystal beam, a different form of electric field is required (in order to suppress the vertical tune in S-LSR). In fact such a form can be found, as will be described in the next chapter.

4.7 The field error

A dispersion-free storage ring has never been constructed. Thus, we have to investigate the influence of the field error of the dispersion-suppressor. In the case of S-LSR, the construction errors of the electrostatic deflectors will cause the larger field errors than that of the bending magnet because of its structure, i.e. the gap of the electrostatic deflector is smaller than that of the bending magnet, thus the error of the gap size

causes the larger error of the field strength, and the existence of the intermediate electrodes complicates the situation. Closed orbit distortion (COD) is considered as an influence of the field error. The COD of the dispersion-free mode of S-LSR should be estimated exactly, because the horizontal aperture of the deflectors is only 30 mm. The coefficient V_0 in Hamiltonian (4-9) represents the strength of the bending electric field. Thus, the error of V_0 will generate the closed orbit distortion. Similarly, the error of the strength of the dipole magnetic field will generate the COD. We suppose that the field error exists uniformly in the dispersion-suppresser. Then the field errors can be included to the Hamiltonian by the formula

$$\phi + \Delta\phi = -(V_0 + \Delta V_0)\cdot \ln\left(1+\frac{x}{\rho_0}\right) \tag{4-33}$$

$$\vec{A} + \Delta\vec{A} = \left(0,\ 0,\ -\frac{B_y + \Delta B_y}{2}(\rho_0 + x)\right) \tag{4-34}$$

Since now the closed orbit distortion of the reference particle is needed, a condition $(\Delta E = 0)$ is supposed. For the dispersion free state, the horizontal equation of motion of the reference particle is given by

$$\frac{d^2x}{ds^2} \approx -\frac{1+\gamma_0^2}{\rho^2}\cdot x + \frac{\gamma_0^2}{\rho}\frac{\Delta V_0}{V_0} - \frac{1+\gamma_0^2}{\rho}\frac{\Delta B_y}{B_y} \tag{4-35}$$

Then, the horizontal phase space coordinates of the reference particle before and after the field error region are given by the extended transfer matrix. [4-20]

$$\begin{pmatrix} x_1 \\ \tilde{p}_{x1} \\ 1 \end{pmatrix} = \begin{pmatrix} \cos\sqrt{k}l & \frac{1}{\sqrt{k}}\sin\sqrt{k}l & \frac{1}{k}\left(1-\cos\sqrt{k}l\right)\Delta f \\ -\sqrt{k}\sin\sqrt{k}l & \cos\sqrt{k}l & \frac{1}{\sqrt{k}}\sin\sqrt{k}l\cdot\Delta f \\ 0 & 0 & 1 \end{pmatrix} \begin{pmatrix} x_0 \\ \tilde{p}_{x0} \\ 1 \end{pmatrix} \tag{4-36}$$

where l is the length of the field error area of the deflector and the following notations has been introduced

$$k = \frac{1+\gamma_0^2}{\rho^2} \qquad \Delta f = \frac{\gamma_0^2}{\rho}\frac{\Delta V_0}{V_0} - \frac{1+\gamma_0^2}{\rho}\frac{\Delta B_y}{B_y}. \tag{4-37}$$

The extended transfer matrix (4-36) can be divided to the part of the orbit distortion induced by the field error and the part of the deflection element

$$M(s_1 \mid s_0) = M_{error}(s_1 \mid s_0) M_{deflector}(s_1 \mid s_0) \tag{4-38}$$

$$= \begin{pmatrix} 1 & 0 & \frac{1}{k}\left(1-\cos\sqrt{k}l\right)\Delta f \\ 0 & 1 & \frac{1}{\sqrt{k}}\sin\sqrt{k}l\cdot\Delta f \\ 0 & 0 & 1 \end{pmatrix} \begin{pmatrix} \cos\sqrt{k}l & \frac{1}{\sqrt{k}}\sin\sqrt{k}l & 0 \\ -\sqrt{k}\sin\sqrt{k}l & \cos\sqrt{k}l & 0 \\ 0 & 0 & 1 \end{pmatrix}$$

If the length l is enough small so that the element can approximate by thin lens, the first part of the transfer matrix Eq. (4-38) can be written as

$$M_{kick}(s_2 \mid s_1) = \begin{pmatrix} 1 & 0 & 0 \\ 0 & 1 & \theta_E - \theta_B \\ 0 & 0 & 1 \end{pmatrix} \tag{4-39}$$

where θ_E and θ_B are the kick angles induced by the field errors

$$\theta_E = \frac{\gamma_0^2}{\rho}\frac{\Delta V_0}{V_0}\cdot l \qquad \theta_B = \frac{1+\gamma_0^2}{\rho}\frac{\Delta B_y}{B_y}\cdot l \tag{4-40}$$

By using the transfer matrix formula (4-38), the COD is estimated.

From the field measurement of the bending magnet, we have found that the field errors of the dipole magnets are far small compared with that of the electric field and the individual difference of each magnetic field strength can be corrected by adjusting the excitation current with a bypath circuit. The six electrostatic deflectors have not yet been completed. However the error of the electric field can be estimated. The main cause of the error of the bending electric field is gap size error of the electrostatic deflector. But, it is difficult to reduce the gap size error less than 0.1 mm from the circumstances on manufacture. When the gap error of the electrostatic deflector is 0.1 mm, the error of the field strength becomes to $\Delta V_0 / V_0 \approx 3.3\times10^{-3}$. When such field error exists, the closed orbit distortion becomes order of 10 mm. This is the same order of the gap of the electrostatic deflector. To cope with such situation, careful adjustment of applied voltage to the main electrodes is planned taking the real measured gap size into account. In order to realize such adjustment, every main electrode in the 6 deflection elements is required to be powered by an individual high voltage supply. With the condition that $\Delta V_0 / V_0$ is suppressed to be less than $1.6\text{x}10^{-4}$, the COD is expected to be less than $\pm$1mm, which is thought to be tolerable size for beam circulation.

4.8 Consideration of the nonlinear effect

In this section, the higher-order Hamiltonian of the dispersion-suppressor is derived, and the effect of the nonlinear term is considered. Here, the Hamiltonian is expanded up to the third-order terms. When the Hamiltonian (4-4) is expanded, it becomes

$$H = -\left(1+\frac{x}{\rho_0}\right)qA_s - \left(1+\frac{x}{\rho_0}\right)p + \frac{p_x^2+p_y^2}{2p} + \frac{p_x^2+p_y^2}{2p}\frac{x}{\rho_0}. \tag{4-41}$$

When the condition of the equilibrium orbit (4-6) is substituted and the terms up to the third-order of x/ρ_0, $\tilde{p}_x$, $\tilde{p}_y$ and $\Delta p/p$ are remained, the expanded Hamiltonian becomes

$$\tilde{H} = \frac{qV_0}{\beta_0^2 E_0}\frac{x}{\rho_0} + \frac{1}{2}\left(1+\frac{qV_0}{\beta_0^2 E_0}\right)\left(\frac{x}{\rho_0}\right)^2 - \left(1+\frac{x}{\rho_0}\right)\frac{\Delta p}{p_0} + \frac{\tilde{p}_x^2+\tilde{p}_y^2}{2} - \frac{\tilde{p}_x^2+\tilde{p}_y^2}{2}\frac{\Delta p}{p_0} + \frac{\tilde{p}_x^2+\tilde{p}_y^2}{2}\frac{x}{\rho_0}. \tag{4-42}$$

The momentum $p = m\beta\gamma c = \sqrt{(p_t + q\phi_D)^2/c^2 - m^2c^2}$ is expanded up to the power of $(\Delta E - q\phi_D)^3$, then, the momentum deviation can be written as

$$\Delta p \approx \frac{\Delta E - q\phi_D}{\beta_0 c} - \frac{1}{2p_0}\left(\frac{\Delta E - q\phi_D}{\beta_0 c\gamma_0}\right)^2 + \frac{1}{2p_0^2\gamma_0^2}\left(\frac{\Delta E - q\phi_D}{\beta_0 c}\right)^3 \tag{4-43}$$

When the momentum deviation Eq. (4-43) is inserted into (4-42), the Hamiltonian becomes as

$$\tilde{H} = \tilde{H}_1 + \tilde{H}_2 \tag{4-44}$$

where $\tilde{H}_1$ is the Hamiltonian up to the second-order terms and $\tilde{H}_2$ is the third-order terms.

$$\tilde{H}_1 = -\frac{\Delta E}{\beta_0^2 E_0} + \frac{1}{2\gamma_0^2}\left(\frac{\Delta E}{\beta_0^2 E_0}\right)^2 + \frac{\tilde{p}_x^2 + \tilde{p}_y^2}{2} - \frac{\Delta E}{\beta_0^2 E_0}\frac{x}{\rho_0}\left(1 - \frac{qV_0}{\gamma_0^2\beta_0^2 E_0}\right) + \frac{1}{2}\left[1 + \frac{1}{\gamma_0^2}\left(\frac{qV_0}{\beta_0^2 E_0}\right)^2\right]\frac{x^2}{\rho_0^2} \tag{4-45}$$

$$\begin{aligned}\tilde{H}_2 = &-\frac{1}{2\gamma_0^2}\left(\frac{\Delta E}{\beta_0^2 E_0}\right)^3 - \frac{\tilde{p}_x^2 + \tilde{p}_y^2}{2}\left(\frac{\Delta E}{\beta_0^2 E_0}\right) + \frac{\tilde{p}_x^2 + \tilde{p}_y^2}{2}\left(1 - \frac{qV_0}{\beta_0^2 E_0}\right)\frac{x}{\rho_0} + \frac{1}{2\gamma_0^2}\left(\frac{\Delta E}{\beta_0^2 E_0}\right)^2\frac{x}{\rho_0}\left(1 - 3\cdot\frac{qV_0}{\beta_0^2 E_0}\right) \\ &+ \frac{1}{2\gamma_0^2}\left(\frac{\Delta E}{\beta_0^2 E_0}\right)\frac{x^2}{\rho_0^2}\frac{qV_0}{\beta_0^2 E_0}\left(1 - 3\cdot\frac{qV_0}{\beta_0^2 E_0}\right) - \frac{1}{2\gamma_0^2}\frac{x^3}{\rho_0^3}\left(\frac{qV_0}{\beta_0^2 E_0}\right)^2\left(1 + \frac{qV_0}{\beta_0^2 E_0}\right) - \frac{1}{3}\frac{x^3}{\rho_0^3}\left(\frac{qV_0}{\beta_0^2 E_0}\right)\end{aligned} \tag{4-46}$$

From this Hamiltonian of the dispersion-suppressor, the Hamiltonian of the flat pole bending magnet is easily derived by setting the electric field V_0 to zero. If the higher-order Hamiltonian of the dispersion-suppressor compared to that of the dipole magnet one finds the dispersion-suppressor inevitably includes nonlinear terms which are thought to be generated by nonlinear field. The reason is simple, the electric field has radial position dependence (Eq. (4-2)), thus, it includes nonlinear components inevitably. It is expected that the larger nonlinear component of the dispersion-suppressor limits the dynamic aperture and causes some resonances. The effect of such nonlinear components is evaluated from the experimental result of KEK electrostatic storage ring [4-21]. The Hamiltonian of the electrostatic deflector of the electrostatic storage ring is also easily given, if the polarity of the scalar potential is reversed and the vector potential of the magnetic field is eliminated from Hamiltonian (4-44) and the equilibrium condition (4-6). Then, one will find the nonlinear component of the electrostatic deflector has the same formula as that of the dispersion-free deflector.

In KEK electrostatic storage ring, the measured 1/e-lifetimes of stored ions are from 12–20 s. The lifetime is limited by interactions with the residual gas, rather than the nonlinear field effect. This result means that the reduction of the dynamic aperture due to the nonlinear effects and the higher-order resonances induced by nonlinear field components doesn't give so large effect to the beam dynamics, if the tune value of the operating point is selected suitably.

For the case of S-LSR, the similar result is expected. The bending radius of S-LSR (1.05m) is larger than that of the KEK electrostatic storage ring (0.25m). According to the higher-order Hamiltonian $\tilde{H}_2$, the higher-order terms induced by the nonlinear component of the bending electric field are in proportion to $1/\rho_0^2$ or $1/\rho_0^3$. Therefore, if the bending radius ρ_0 is increased, the total effect of the nonlinear fields per one turn becomes smaller. Furthermore, real aperture and beam emittance of S-LSR are small originally, thus, the nonlinear effects may not become the problem. It is known generally that the nonlinear effects become weak, as the beam size and emittance is reduced. Therefore, once a crystalline beam (which is ultimate low emittance beam) is formed, the nonlinear effects become still smaller, although, the nonlinear effects may influence the formation process of the crystal.

4.9 Summary of this chapter

The dispersion-free storage ring might be useful for the stabilization of a 3D crystal beam, because the shear heating mechanism is canceled, and the dynamics of the beam becomes equivalent to that of the linear ion trap. MD simulations based on the Hamiltonian without the shear term was already performed in Ref. [4-22], and it showed the generation of 3D crystalline beam, although, the beam focusing force of this MD simulation was time-independent. A MD simulation including the time-dependent alternating focusing force and higher-order nonlinear effects will be the scope of our further investigation.

This scheme is introduced to the ion cooler ring S-LSR, which is now under construction. In S-LSR, the dispersion-suppressor is realized by inserting a cylindrical electrostatic deflector into the small gap of the dipole magnet. The calculation of the beam dynamics has been performed based on the parameters of the deflectors. From the result of the theoretical investigations, we have found that the dispersion-free mode of S-LSR is a stable circulating mode of the beam free from the shear heating mechanism, and provides a lot of capability for beam dynamics study, although, the dispersion-free mode of S-LSR has such a restriction as not satisfying the second maintenance condition for beam crystallization. However, this problem can be solved by introducing a different type of electrostatic field. The details of the new type of electric field are described in the next chapter.

References

[4-1] T. Kamei, M. Kihara "*Accelerator Science*" (Maruzen, Tokyo, 1993) [in Japanese]

[4-2] W. Henneberg: Annalen der Physik. **19**, 335 (1934) [in German]

[4-3] W. E. Millet: Phys. Rev. **74**, 1058 (1948)

[4-4] S. Y. Lee, *Accelerator Physics*, World Scientific (Singapore) p30 (1999);

[4-5] H. Okamoto, S. Machida, Nucl. Instrum. Methods. A **482** (2002) 65.

[4-6] J. Wei, X.-P. Li, and A. M. Sessler, Phys. Rev. Lett. **73**, 3089 (1994).

[4-7] R. W. Hasse and J. P. Shiffer, Annals of Phys. **203**, 419 (1990).

[4-8] H. Okamoto, J. Wei, Phys. Rev. E. **58**, 3817 (1998)

[4-9] The term *ground state* is used to describe the periodic lowest energy state of the beam in Ref [4-6].

[4-10] The shear term of the storage ring constructed with dispersion-suppressers coincides with that of the magnetic storage ring, if the bending electric field is set to zero.

[4-11] M. Block, A Drakoudis, H. Leuthner, P. Seibert and G. Werth, J. Phys. B: At Mol. Opt. Phys. **33** L375-L382 (2000)

[4-12] T. Suzuki, Part. Accel. **12**, 237 (1982)

[4-13] T. Kihara, H. Okamoto, Y. Iwashita, K. Oide, G. Lamanna, J. Wei, Phys. Rev. E, **59**, 3594 (1999)

[4-14] H. Okamoto, Phys. Rev. E. **50**, 4982 (1994)

[4-15] H. Okamoto, A. M. Sessler, D. Möhl, Phys. Rev. Lett. **72**, 3977 (1994)

[4-16] H. N. Slingeriand, J. Vac. Sci. Technol. B7(1) 83 (1988)

[4-17] S. Y. Lee, *Accelerator Physics*, World Scientific (Singapore) p227 (1999)

[4-18] The transfer matrix calculation was performed by using the code, MAD8. The notation of the phase space vector agrees with MAD formalism by easy scaling of the components of the vector. We newly defined the transfer matrix of the dispersion-suppressor in MAD. Refer to following about the calculation method;

H. Grote, F. C. Iselin, The Mad program User's reference manual, CERN/SL/90-13;
F. C. Iselin, The Mad program Physical method manual, CERN/SL/92

[4-19] T. Shirai, H. Fadil, M. Ikegami, A. Morita, H. Tongu, A. Yamazaki, Y. Iwashita, A. Noda, K. Okabe, Y. Yuri, H. Okamoto, M. Grieser, in Proceedings of EPAC 2002, 623 (2002).

[4-20] S. Y. Lee, *Accelerator Physics*, World Scientific (Singapore) (1999)

[4-21] T. Tanabe, K. Chida, K. Noda, I. Watanabe, Nucl. Instrum. Methods. A **482**, 595 (2002);
T. Tanabe and K. Noda, Nucl. Instrum. Methods. A **496**, 233 (2003)

[4-22] A. Rahman, and J. P. Schiffer, Phys, Rev. Lett. **57**, 1133 (1986)

[4-23] M. Tanabe, "*Beam test with electrostatic deflector for dispersion-free storage ring*" Master's thesis; Department of physics, Faculty of Science, Kyoto-University (2005)

Chapter 5. Optimum dispersion-free deflector for S-LSR

5.1 Search of the optimum dispersion-free deflector

As shown in the previous chapter, the dispersion-free deflector is realized by the combination of a flat pole dipole magnet and a cylindrical electrostatic deflector. However, this dispersion-free deflector is not suitable for a small size ion storage ring, because the radial focusing becomes too strong and this effect greatly affects the beam dynamics. In the case of S-LSR, horizontal beta function and the vertical betatron tune value are extremely enhanced. This violates the maintenance condition $\nu_T < N/2\sqrt{2}$. It is necessary to search a dispersion-free deflector which has the weaker radial focusing effect. It is expected that the strength of the radial focusing is changed by changing the radial field distribution in the electrostatic deflector. In this chapter, possible electric field distribution satisfying Maxwell equation is investigated and the structure of the electrostatic deflector is also investigated. Next, the beam dynamics in the electrostatic deflector and the dispersion free deflector is formulated. Finally, the beam dynamics and lattice parameters of S-LSR are investigated, when the suitable dispersion-free deflector is applied to S-LSR.

5.2 Possible solutions of Maxwell equation

5.2.1 Coordinate system

Maxwell equation is solved in a cylindrical coordinate system. The relations between rectangular coordinates and cylindrical coordinates are given by

$$r = \sqrt{x^2 + y^2} \qquad \varphi = \tan^{-1}\frac{y}{x} \qquad z = z$$

In the cylindrical coordinate system, the differential operators are given by the following formulas.

$$(grad\phi)_r = \frac{\partial}{\partial r}\phi \qquad (grad\phi)_\varphi = \frac{1}{r}\frac{\partial}{\partial \varphi}\phi \qquad (grad\phi)_z = \frac{\partial}{\partial z}\phi$$

$$\Delta\phi = \frac{\partial^2}{\partial r^2}\phi + \frac{1}{r}\frac{\partial}{\partial r}\phi + \frac{1}{r^2}\frac{\partial^2}{\partial \varphi^2}\phi + \frac{\partial^2}{\partial z^2}\phi$$

5.2.2 Solutions of Laplace's equation

In the space between the deflection electrodes, the scalar potential of the electrostatic field ϕ has to be the solutions of Laplace's equation.

$$\Delta\phi = 0$$

We assume the solution of the form

$$\phi(r,\varphi,z) = F(r,z)S(\varphi), \tag{5-1}$$

in order to separate the variables. Then, the Laplace's equation can be separated as

$$\frac{\partial^2}{\partial r^2}F(r,z)+\frac{1}{r}\frac{\partial}{\partial r}F(r,z)+\frac{\partial^2}{\partial z^2}F(r,z)-\frac{C}{r^2}F(r,z)=0 \tag{5-2-a}$$

$$\frac{\partial^2}{\partial \varphi^2}S(\varphi)+CS(\varphi)=0 \tag{5-2-b}$$

where C is optional constant. In order to realize the usable electrostatic potential as electrostatic deflectors, the scalar potential ϕ must not have φ dependence. Therefore, $S(\varphi)$ must be constant, and thus C must be 0. Then, Eq. (5-2-a) becomes

$$\frac{\partial^2}{\partial r^2}F(r,z)+\frac{1}{r}\frac{\partial}{\partial r}F(r,z)+\frac{\partial^2}{\partial z^2}F(r,z)=0 \tag{5-3}$$

The solutions satisfying this differential equation becomes the usable electrostatic potential. Namely,

$$\phi(r,\varphi,z)=aF(r,z)$$

where, a is constant.

5.2.3 Possible electrostatic potential

There are the following three easy solutions.

(1) Spherical electrostatic deflector.

$$\phi(r,\varphi,z)=\frac{a}{\sqrt{r^2+z^2}}+const \tag{5-4}$$

The shape of the electrode to realize such the electrostatic potential is decided from the shape of the equal potential surface. In this case, the shape of the electrode becomes a spherical surface.

(2) Cylindrical electrostatic deflector

$$\phi(r,\varphi,z)=a\cdot\ln(r)+const \tag{5-5}$$

The shape of the electrode is decided form the equation

$$\ln(r)=const. \tag{5-6}$$

This solution is $r=const$. In the cylindrical coordinate system such a curved surface becomes cylinder.

(3) Hyperbolic electrostatic deflector

$$\phi(r,\varphi,z)=a(r^2-2z^2)+const \tag{5-7}$$

The shape of electrode is decided form the equation

$$r^2+2z^2=const \tag{5-8}$$

The solution is a hyperbola. Therefore, the cross section form of the electrostatic deflector becomes hyperbolic curve.

The linear combinations of these three solutions are also the solutions of Laplace's equation. For example, we consider the linear combination of the solution (2) and (3)

$$\phi(r,\varphi,z)=a\left(\ln(r)+n(r^2+2z^2)\right)+C, \tag{5-9}$$

where n and C are constants

The cross section shape of the electrode to realize this electrostatic potential is shown in Fig. 5-1.

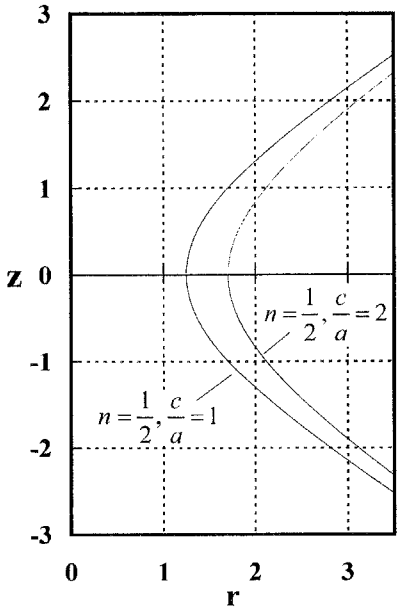

Fig. 5-1. Cross section shape of the deflector

The cross section shape is similar to a hyperbola, but not the hyperbola. Thus, we call such a electrostatic deflector semi-hyperbolic electrostatic deflector. The semi-hyperbolic electrostatic deflector will bear important role in the dispersion-free deflector.

In addition to the solutions (1)-(3), a toroidal electrostatic deflector exists [5-1]. However, the toroidal electrostatic deflector is not needed for our purpose. Thus the details of the toroidal electrostatic deflector are not described here.

5.3 Beam dynamics in the electrostatic deflectors

The beam dynamics in a spherical [5-2], a cylindrical [4-21] and a toroidal [5-1] electrostatic deflector has been investigated and formulated by forerunner's work. In this section, we newly formulate the beam dynamics in the hyperbolic electrostatic deflector and the linear combination of the electrostatic potentials shown in section 5.2. The formalism of the electrostatic deflectors and the dispersion-free deflectors has many common features. In accelerator physics, Frenet-Serret coordinate system is usually used [4-4]. If a circle of the radius ρ_0 in the cylindrical coordinate system is selected as the reference orbit of the Frenet-Serret coordinate system, the relations between the cylindrical coordinates and the Frenet-Serret coordinates are given by

$$\rho_0 + x = r \qquad s = \rho_0\varphi \qquad y = z.$$

In the Frenet-Serret coordinate system, the differential operators are given by the following formulas.

$$(grad\phi)_x = \frac{\partial}{\partial x}\phi \qquad (grad\phi)_s = \frac{1}{h}\frac{\partial}{\partial s}\phi \qquad (grad\ \phi)_y = \frac{\partial}{\partial y}\phi$$

$$\Delta\phi = \frac{1}{h}\left[\frac{\partial}{\partial x}h\frac{\partial\phi}{\partial x} + \frac{\partial}{\partial s}\frac{1}{h}\frac{\partial\phi}{\partial s} + \frac{\partial}{\partial y}h\frac{\partial\phi}{\partial y}\right]$$

where $h = 1 + x/\rho_0$.

5.3.1 Beam dynamics in the hyperbolic electrostatic deflector

In the Frenet-Serret coordinate system, the electrostatic potential of the hyperbolic electrostatic deflector is given by

$$\phi(x,y,s) = \frac{V_0}{2}\left[\left(1+\frac{x}{\rho_0}\right)^2 - 2\left(\frac{y}{\rho_0}\right)^2 - 1\right]. \tag{5-10}$$

where the constants of Eq. (5-7) are selected so that the electrostatic deflector has a zero potential and the bending field strength V_0/ρ_0 along the reference orbit. If the vector potential of the bending magnetic field is eliminated from the Hamiltonian (4-13), we obtain the relativistic Hamiltonian which governs the motion of a charged particle in a bending electrostatic deflector

$$H = -\left(1+\frac{x}{\rho_0}\right)\sqrt{\left(\frac{p_t + q\phi_D}{c}\right)^2 - m^2c^2 - p_x^2 - p_y^2}\,, \tag{5-11}$$

where m and q are the rest mass and charge state of particles, c is the speed of light, ϕ_D is the scalar potential in the electrostatic deflector, p_t is the longitudinal canonical momentum conjugate to time t. By expanding the square root and leaving only low-order terms, Eq. (5-11) becomes

$$H = -\left(1+\frac{x}{\rho}\right)p + \frac{p_x^2 + p_y^2}{2p}, \tag{5-12}$$

where $p = m\beta\gamma c = \sqrt{(p_t + q\phi)^2/c^2 - m^2c^2}$. Since the electric field strength is V_0/ρ along the design orbit, equilibrium kinetic momentum becomes

$$p_0 = \frac{qV_0}{\beta_0 c}. \tag{5-13}$$

The momentum deviation from the design momentum $p_0 = m\beta_0\gamma_0 c = \sqrt{p_t^2/c^2 - m^2c^2}$ can approximately be written as

$$\Delta p \equiv p - p_0 \approx \frac{\Delta E - q\phi_D}{\beta_0 c} - \frac{1}{2p_0}\left(\frac{\Delta E - q\phi_D}{\beta_0 c\gamma_0}\right)^2. \tag{5-14}$$

ΔE is the energy deviation from the design value $-\Delta E = m\gamma_0 c^2 - (-p_t)$. Inserting Eq. (5-13) and $p = p_0 + \Delta p$ into Eq. (5-12) and neglecting nonlinear terms, one finds

$$\tilde{H} = -\left(1+\frac{x}{\rho_0}\right) - \left(1+\frac{x}{\rho_0}\right)\frac{\Delta p}{p_0} + \frac{\tilde{p}_x^2 + \tilde{p}_y^2}{2}, \tag{5-15}$$

where the transverse momenta have been scaled to be dimensionless; namely, $\tilde{p}_{x(y)} = p_{x(y)}/p_0$. Substitution of Eq. (5-14) together with Eq. (5-13) into Eq. (5-15) yields the approximate Hamiltonian

$$\tilde{H}=\frac{\tilde{p}_x^2+\tilde{p}_y^2}{2}-\frac{\Delta E}{\beta_0^2E_0}+\frac{1}{2\gamma_0^2}\left(\frac{\Delta E}{\beta_0^2E_0}\right)-\left(1+\frac{1}{\gamma_0^2}\right)\frac{\Delta E}{\beta_0^2E_0}\frac{x}{\rho_0}+\frac{1}{2}\left(3+\frac{1}{\gamma_0^2}\right)\left(\frac{x}{\rho_0}\right)^2-\left(\frac{y}{\rho_0}\right)^2 \tag{5-16}$$

From this Hamiltonian, the equations of motion in the hyperbolic electrostatic deflector are obtained.

$$\frac{d^2x}{ds^2}=-\left(3+\frac{1}{\gamma_0^2}\right)\frac{x}{\rho_0^2}+\frac{1}{\rho_0}\left(1+\frac{1}{\gamma_0^2}\right)\frac{\Delta E}{\beta_0^2E_0} \tag{5-17-a}$$

$$\frac{d^2y}{ds^2}=\frac{2}{\rho_0^2}y \tag{5-17-b}$$

In non-relativistic limit $\gamma_0\to 1$, the hyperbolic electrostatic deflector has a horizontal focusing of the strength $4/\rho_0^2$ and a vertical defocusing of the strength $2/\rho_0^2$.

5.3.2 Beam dynamics in the other electrostatic deflectors

The beam dynamics in two kinds of linear combinations of the electrostatic potentials such as Eq. (5-9) is investigated. First, the beam dynamics in the semi-hyperbolic electrostatic deflector is investigated. As shown in Eq. (5-9), electrostatic potential of the semi-hyperbolic electrostatic deflector can be expressed by the linear combination of the cylindrical electrostatic potential and the hyperbolic electrostatic potential. The ratio of the linear combination is supposed to be

$$\begin{aligned}\phi(x,y,s)&=\frac{V_0}{2}\left\{(2-C)\ln\left(1+\frac{x}{\rho_0}\right)+C\left[\frac{1}{2}\left(1+\frac{x}{\rho_0}\right)^2-\left(\frac{y}{\rho_0}\right)^2-\frac{1}{2}\right]\right\}\\&\approx\frac{V_0}{2}\left[2\frac{x}{\rho_0}+(C-1)\left(\frac{x}{\rho_0}\right)^2-C\left(\frac{y}{\rho_0}\right)^2+\ldots\right]\end{aligned} \tag{5-18}$$

where C decides the ratio of the linear combination. In this case, the condition of the equilibrium kinetic momentum is same as Eq. (5-13), and the Hamiltonian becomes

$$\tilde{H}=\frac{\tilde{p}_x^2+\tilde{p}_y^2}{2}-\frac{\Delta E}{\beta_0^2E_0}+\frac{1}{2\gamma_0^2}\left(\frac{\Delta E}{\beta_0^2E_0}\right)-\left(1+\frac{1}{\gamma_0^2}\right)\frac{\Delta E}{\beta_0^2E_0}\frac{x}{\rho_0}+\frac{1}{2}\left(C+1+\frac{1}{\gamma_0^2}\right)\left(\frac{x}{\rho_0}\right)^2-\frac{C}{2}\left(\frac{y}{\rho_0}\right)^2 \tag{5-19}$$

Then, the equations of motion are

$$\frac{d^2x}{ds^2}=-\left(C+1+\frac{1}{\gamma_0^2}\right)\frac{x}{\rho_0^2}+\frac{1}{\rho_0}\left(1+\frac{1}{\gamma_0^2}\right)\frac{\Delta E}{\beta_0^2E_0} \tag{5-20-a}$$

$$\frac{d^2y}{ds^2}=\frac{C}{\rho_0^2}y \tag{5-20-b}$$

In non-relativistic limit $\gamma_0\to 1$, the semi-hyperbolic electrostatic deflector has a horizontal focusing of the strength $(C-2)/\rho_0^2$ and a vertical defocusing of the strength C/ρ_0^2.

We also consider the following linear combination of the spherical electrostatic potential and cylindrical electrostatic potential.

$$\begin{aligned}\phi(x,y,s)&=V_0\left\{(1-C)\ln\left(1+\frac{x}{\rho_0}\right)-C\left[\frac{\rho_0}{\sqrt{(\rho_0+x)^2+y^2}}-1\right]\right\}\\&\approx V_0\left[\frac{x}{\rho_0}-\frac{1}{2}(1+C)\left(\frac{x}{\rho_0}\right)^2+\frac{C}{2}\left(\frac{y}{\rho_0}\right)^2+\ldots\right]\end{aligned} \tag{5-21}$$

In the followings, we call an electrostatic deflector generating this electrostatic potential as a semi-spherical electrostatic deflector. In this case, the condition of the equilibrium kinetic momentum is also same as Eq (5-13), and the Hamiltonian becomes

$$\tilde{H}=\frac{\tilde{p}_x^2+\tilde{p}_y^2}{2}-\frac{\Delta E}{\beta_0^2 E_0}+\frac{1}{2\gamma_0^2}\left(\frac{\Delta E}{\beta_0^2 E_0}\right)-\left(1+\frac{1}{\gamma_0^2}\right)\frac{\Delta E}{\beta_0^2 E_0}\frac{x}{\rho_0}+\frac{1}{2}\left(1+\frac{1}{\gamma_0^2}-C\right)\left(\frac{x}{\rho_0}\right)^2+\frac{C}{2}\left(\frac{y}{\rho_0}\right)^2 \tag{5-22}$$

Then the equations of motion are

$$\frac{d^2x}{ds^2}=-\left(1+\frac{1}{\gamma_0^2}-C\right)\frac{x}{\rho_0^2}+\frac{1}{\rho_0}\left(1+\frac{1}{\gamma_0^2}\right)\frac{\Delta E}{\beta_0^2 E_0} \tag{5-23-a}$$

$$\frac{d^2y}{ds^2}=-\frac{C}{\rho_0^2}y \tag{5-23-b}$$

In non-relativistic state, the equation of motion of a charged particle in electrostatic deflectors described above can be summarized as follows.

$$\frac{d^2x}{ds^2}=-(2-n)\frac{x}{\rho_0^2}+\frac{1}{\rho_0}\frac{\Delta E}{E_0} \tag{5-24-a}$$

$$\frac{d^2y}{ds^2}=-\frac{n}{\rho_0^2}y \tag{5-24-b}$$

The value of n corresponds to the following structure of deflectors.

Table 5-1. Field index (n) of electrostatic deflectors.

Structure of electrostatic deflector	Spherical	Semi-spherical	Cylindrical	Semi-hyperbolic	Hyperbolic
value of n	1	$1>n>0$	0	$0>n>-2$	-2

From Eq. (5-20), it is found that the semi-hyperbolic electrostatic deflector can create the focusing strength as same as the semi-spherical deflector, in the first order. Furthermore, the other combination, for example, linear combination of Spherical and Hyperbolic electrostatic potential also realizes the same equation of motion of the semi-hyperbolic or semi-spherical electrostatic deflector, in the first order. But, if the higher-order effect is considered, one finds the linear combinations listed in Table 5-1 can realize a bending field which includes the smaller nonlinear component.

5.4 Beam dynamics in dispersion-free deflectors

5.4.1 Beam dynamics

In the previous chapter, the dispersion-free deflector has been constructed by the combination of a flat pole dipole magnet and a cylindrical electrostatic deflector. Now, we have formulas of the other type of electrostatic deflector. The other combination of a dipole magnet and an electrostatic deflector can be investigated by using these formulas, and it can create new dispersion-free deflection element. In the following, the equations of motion of a charged particle in deflectors which are constructed with flat pole dipole magnets and various electrostatic deflectors are investigated.

First, the combination of a dipole magnet and a semi-hyperbolic electrostatic deflector is supposed. In the followings, we call this deflector as a semi-hyperbolic dispersion-suppresser. Then, the Hamiltonian is given by Eq (4-4), the scalar potential is given by Eq. (5-18) the vector potential is given by Eq. (4-1). By the same

way of the previous subsection, Hamiltonian (4-4) is expanded, and the momentum deviation Δp (eq. (4-7)) and the equilibrium condition eq. (4-6) are substituted. Finally, neglecting the higher-order terms, the Hamiltonian becomes

$$\begin{aligned}\tilde{H} = &-\frac{\Delta E}{\beta_0^2 E_0}+\frac{1}{2\gamma_0^2}\left(\frac{\Delta E}{\beta_0^2 E_0}\right)^2+\frac{\tilde{p}_x^2+\tilde{p}_y^2}{2}-\frac{\Delta E}{\beta_0^2 E_0}\frac{x}{\rho_0}\left(1-\frac{qV_0}{\gamma_0^2\beta_0^2 E_0}\right)\\ &+\frac{1}{2}\left[1-C\frac{qV_0}{\beta_0^2 E_0}+\frac{1}{\gamma_0^2}\left(\frac{qV_0}{\beta_0^2 E_0}\right)^2\right]\left(\frac{x}{\rho_0}\right)^2+\frac{C}{2}\frac{qV_0}{\beta_0^2 E_0}\left(\frac{y}{\rho_0}\right)^2\end{aligned} \tag{5-25}$$

Then the equations of motion are

$$\frac{d^2x}{ds^2} = -\frac{1}{\rho_0^2}\left[1-C\frac{qV_0}{\beta_0^2 E_0}+\frac{1}{\gamma_0^2}\left(\frac{qV_0}{\beta_0^2 E_0}\right)^2\right]x+\frac{1}{\rho_0}\left(1-\frac{qV_0}{\gamma_0^2\beta_0^2 E_0}\right)\frac{\Delta E}{\beta_0^2 E_0} \tag{5-26-a}$$

$$\frac{d^2y}{ds^2} = -\frac{C}{\rho_0^2}\frac{qV_0}{\beta_0^2 E_0}y \tag{5-26-b}$$

The last term of eq. (5-26-a) is cause of the linear dispersion. Therefore, if the relation $qV_0/\gamma_0^2\beta_0^2 E_0 = 1$ is satisfied, the linear dispersion is canceled out. This relation and the condition of the equilibrium orbit Eq. (4-6) also leads the relation $(1+1/\gamma_0^2)E(\rho_0) = \beta_0 cB_y$, where $E(\rho_0)$ is the strength of the bending electric field on the reference orbit; $E(\rho_0) = V_0/\rho_0$. This condition is complete same as the dispersion free condition shown in section 4.1 and 4.2.2 . When non-relativistic limit $\gamma_0 \to 1$ and the dispersion-free condition $qV_0/\gamma_0^2\beta_0^2 E_0 = 1$ are imposed, the strength of the horizontal focusing and the vertical focusing become $(2-C)/\rho_0^2$ and C/ρ_0^2, respectively.

The case of the combination of a dipole magnet and a semi-spherical electrostatic deflector is also investigated. In the followings, we call this deflector as a semi-spherical dispersion-suppresser. Then, the scalar potential is given by Eq. (5-21), and the Hamiltonian becomes

$$\begin{aligned}\tilde{H} = &-\frac{\Delta E}{\beta_0^2 E_0}+\frac{1}{2\gamma_0^2}\left(\frac{\Delta E}{\beta_0^2 E_0}\right)^2+\frac{\tilde{p}_x^2+\tilde{p}_y^2}{2}-\frac{\Delta E}{\beta_0^2 E_0}\frac{x}{\rho_0}\left(1-\frac{qV_0}{\gamma_0^2\beta_0^2 E_0}\right)\\ &+\frac{1}{2}\left[1+C\frac{qV_0}{\beta_0^2 E_0}+\frac{1}{\gamma_0^2}\left(\frac{qV_0}{\beta_0^2 E_0}\right)^2\right]\left(\frac{x}{\rho_0}\right)^2-\frac{C}{2}\frac{qV_0}{\beta_0^2 E_0}\left(\frac{y}{\rho_0}\right)^2\end{aligned} \tag{5-27}$$

From this Hamiltonian, one can find that the linear dispersion is canceled out in the same condition of the case of Hamiltonian (5-25). In the non-relativistic and the dispersion-free condition, the semi-spherical dispersion-suppresser has the horizontal focusing of the strength $(2+C)/\rho_0^2$ and the vertical defocusing of the strength C/ρ_0^2.

From the above results, it is found that the dispersion-free deflectors described above have similar rule about the focusing strength to the electrostatic deflectors. In non-relativistic limit, the equations of motion of a charged particle in dispersion-free deflectors can be summarized as

$$\frac{d^2x}{ds^2} = -(2+n)\frac{x}{\rho_0^2} \tag{5-28-a}$$

$$\frac{d^2y}{ds^2} = \frac{n}{\rho_0^2}y \tag{5-28-b}$$

Table 5-2. Field index (n) of dispersion-free deflectors.

Structure of electrostatic deflector	Spherical	Semi-spherical	Cylindrical	Semi-hyperbolic	Hyperbolic
value of n	1	$1>n>0$	0	$0>n>-2$	-2

5.4.2 Optimum dispersion-free deflector

Only the dispersion-free deflector with the combination of a flat pole dipole magnet and a cylindrical electrostatic deflector has been proposed so far. Such dispersion-free deflector has the focusing effect only in the horizontal (radial) direction. On the other hand, the semi-hyperbolic dispersion-free deflector has the focusing effect in the both direction (see Table 5-2 and Eq. (5-28)). Especially, if the coefficient of the linear combination C of the scalar potential Eq. (5-18) is selected to be $C=1$ (this corresponds to the field index $n=-1$ in Table 5-2), this semi-hyperbolic electrostatic deflector has approximately radially uniform electrostatic field near the reference orbit and it has the same focusing strength in the both directions. Thus, the particles of the same charge state and mass can be bent and focused at the same focal point despite the different kinetic energy. Therefore, if such deflector is used, the beam transport system can be constructed without quadrupole magnets for the beam focusing, in addition to the dispersinless bend. It may become powerful tool of mass analyzes. For relativistic particles, from Hamiltonian (5-25), the following equations of motion of a charged particle in the semi-hyperbolic dispersion-free deflector are obtained

$$\frac{d^2x}{ds^2} = -\frac{x}{\rho_0^2} \tag{5-29-a}$$

$$\frac{d^2y}{ds^2} = -\gamma_0^2\frac{y}{\rho_0^2}. \tag{5-29-b}$$

5.5 Easing of the shearing force

Our main purpose of using the dispersion-free deflector is to cancel the shearing force. As shown in section 4.3, it is essential that the energy transfer between the kinetic energy and the potential energy at the entrance of the dispersion-free deflector. It is afraid that the dispersion-free deflectors except for cylindrical dispersion-free deflector induce the different acceleration or deceleration of the particles deviated from the reference orbit vertically, because they have the vertical component of the electric field. Thus, we have to investigate the effect of the vertical component of the dispersion-free deflectors.

When the relative time $\Delta t = t - s/\beta_0 c$ is introduced, from the Hamiltonian (5-24), (5-26), the same longitudinal equations of motion as Eq. (4-16) are obtained. Therefore, for crystal beams ($\Delta E = 0$), the difference of the revolution time of each particle doesn't depend on its radial position x in the dispersion-free condition. These are the same result as the dispersion-free deflector constructed with a cylindrical electrostatic deflector. The difference arises in the second-order. The momentum spread is approximately given from Eq. (5-14). For crystal beams ($\Delta E = 0$), the momentum deviation in the dispersion free deflector can be written as

$$\frac{\Delta p}{p_0} \approx -\frac{q\phi_D}{\beta_0^2 E_0} - \frac{1}{2\gamma_0^2}\left(\frac{q\phi_D}{\beta_0^2 E_0}\right)^2 \tag{5-30}$$

For the case of the cylindrical dispersion-free deflector, Eq. (5-30) gives the relation

$$\frac{\Delta p}{p_0} \approx \gamma_0^2 \frac{x}{\rho_0} - \gamma_0^2 \left(\frac{x}{\rho_0} \right)^2 \tag{5-31}$$

The first-order term cancel the shearing force, but the second order term cannot cancel the shearing force. However, in general, the extent of the beam (x, y) of crystal beams is far small compared to the bending radius ρ_0. Therefore, even if the crystal structure is distorted by the higher-order effect, the amount is very small, and the distortion could be enough recovered at the cooling section and the bunching rf cavity. In this case, the equilibrium temperature of the crystalline beam discussed in section 4.3.4 is determined by the higher-order shear heating. Thus, the equilibrium temperature is very low, compared with the case in which the linear dispersion remains. In the same way, the momentum spread in the semi-hyperbolic dispersion-free deflector is given by the equation

$$\frac{\Delta p}{p_0} \approx \gamma_0^2 \frac{x}{\rho_0} - \frac{\gamma_0^2}{2} \left(\frac{x}{\rho_0} \right)^2 - \frac{\gamma_0^2}{2} \left(\frac{y}{\rho_0} \right)^2 \tag{5-32}$$

The last term is thought to cause a shear in vertical direction in the second order. This term arise because of the vertical component of the electric field. But this term is second-order. Thus, this term doesn't become problem. The other dispersion-free deflectors also have difference only in the higher order.

5.6 Application to the lattice of S-LSR

5.6.1 Transfer matrix calculation

The beam dynamics in S-LSR is investigated when the semi-hyperbolic electrostatic deflector is introduced instead of the cylindrical electrostatic deflector. The lattice parameters are obtained by the transfer matrix calculations. The linear transfer matrix of the semi-hyperbolic dispersion-free deflector becomes as

$$M = \begin{pmatrix} \cos\sqrt{k_x}L & \frac{1}{\sqrt{k_x}}\sin\sqrt{k_x}L & 0 & 0 & 0 & 0 \\ -\sqrt{k_x}\sin\sqrt{k_x}L & \cos\sqrt{k_x}L & 0 & 0 & 0 & 0 \\ 0 & 0 & \cos\sqrt{k_y}L & \frac{1}{\sqrt{k_y}}\sin\sqrt{k_y}L & 0 & 0 \\ 0 & 0 & -\sqrt{k_y}L\sin\sqrt{k_y}L & \cos\sqrt{k_y}L & 0 & 0 \\ 0 & 0 & 0 & 0 & 1 & \frac{L}{\beta_0^2\gamma_0^2} \\ 0 & 0 & 0 & 0 & 0 & 1 \end{pmatrix} \tag{5-33}$$

where the following notations have been introduced.

$$k_x = \frac{1}{\rho_0^2} \qquad k_y = \gamma_0^2 \frac{1}{\rho_0^2}$$

For the case of the storage of 35 keV $^{24}Mg^+$ beam, non-relativistic approximation $\gamma_0 = 1$ is good approximation. From the linear transfer matrix, the stable region of the betatron oscillation and the lattice parameters of S-LSR can be calculated. The stable region of the betatron oscillation is shown in Fig. 5-2.

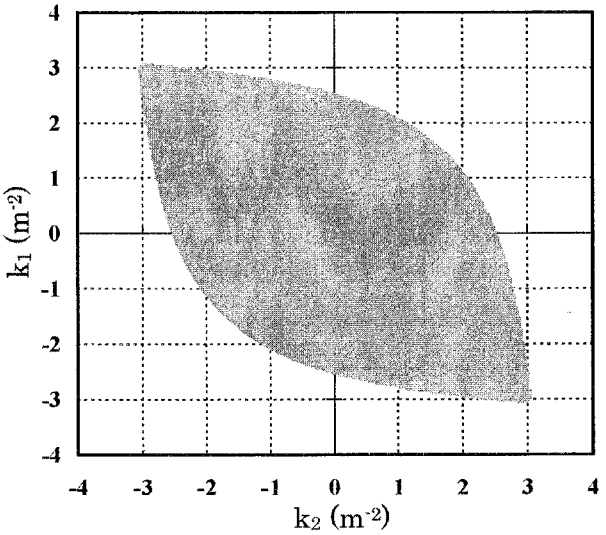

Fig. 5-2. Stable region of the betatron oscillation. The field gradient of two quadrupole magnets k_1 and k_2 are selected as the parameter. The minus sign of the field gradient means defocus in the horizontal direction.

The characteristic of this stable region is that the ring can operate without quadrupole magnet. This is the result from that the deflection element has the focusing effect in both directions. The tune values at the operating point k_1, k_2=0 are (2.1109, 2.1109). At this operating point, the horizontal and vertical beta functions have a completely same shape because the dynamics of the both direction becomes same (Fig. 5-3). It is found that this operating point satisfies the second maintenance condition at S-LSR.

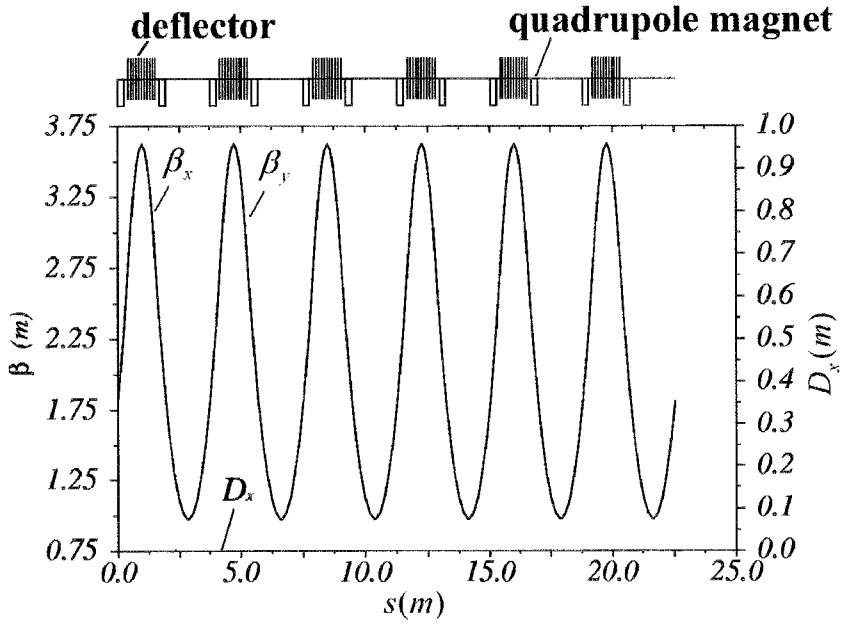

Fig. 5-3 Beta-functions at the operating point (2.1109, 2.1109)

In Fig. 5-2, the operating points except for (2.1109, 2.1109) have different horizontal tune value and vertical tune value, because the quadrupole magnets break the balance between the horizontal and the vertical motions. In real operation, it thought to be better that the tune values are slightly changed by imposing the quadrupole magnet, in order to avoid the strong coupling resonance between horizontal motion and vertical motion.

5.6.2 Fringing field effect

As shown in ref. [5-3], the fringe field of the dipole magnet induces a weak defocus effect in the vertical direction, even if the magnet has no edge angle. We have found that the edge of the dispersion-free deflector of S-LSR also has the defocus effect in the vertical direction. The fringing field of the electrostatic deflector falls to zero faster than that of the bending magnet (Fig. 5-4). Thus, the fringing field of the electrostatic field can be approximated with a sharp edge and the magnetic field is approximated with a linear fringing field. (Fig 5-5)

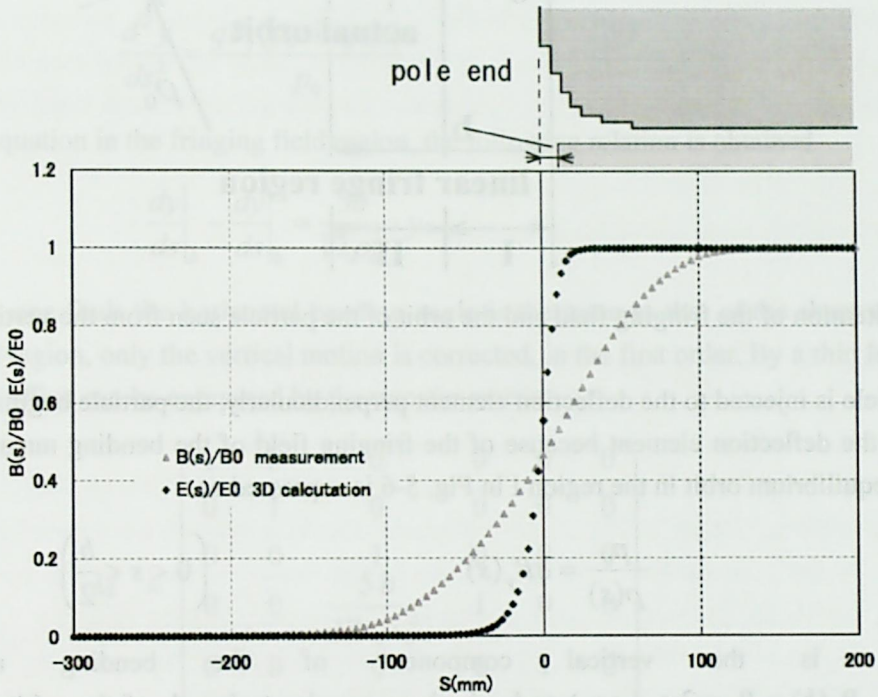

Fig. 5-4 Real fringing field of the deflection element of S-LSR

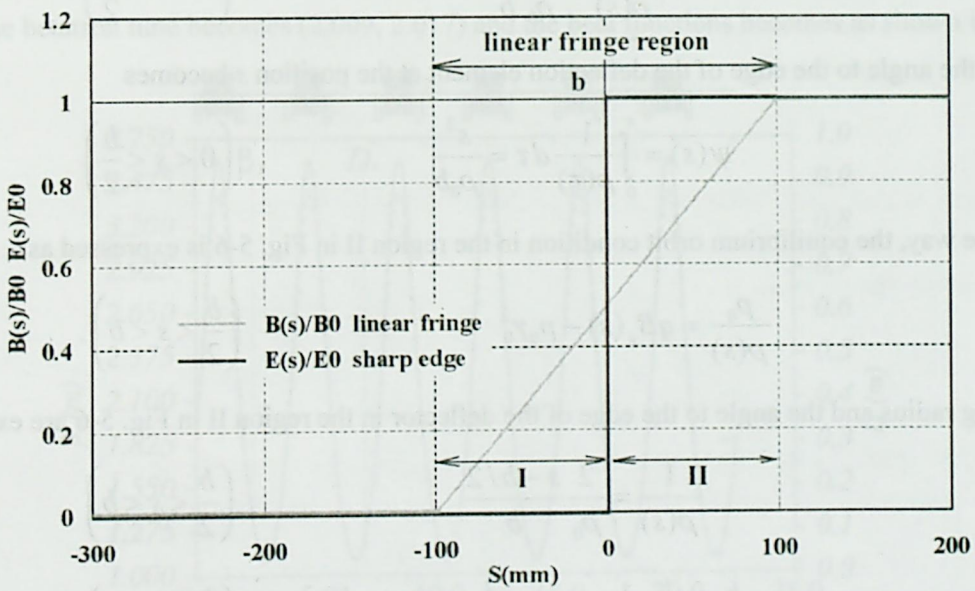

Fig. 5-5 Approximate shape of the fringing field

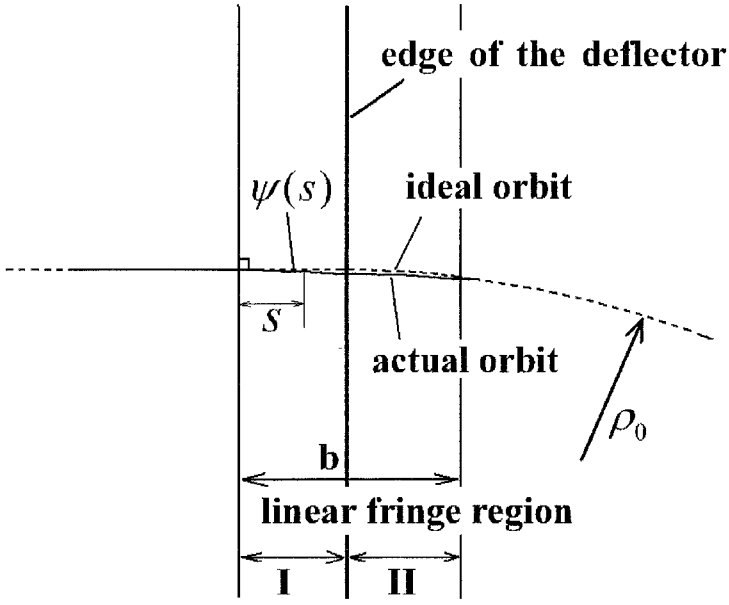

Fig. 5-6 The situation of the fringing field and the orbit of the particle seen from the vertical direction

If a charged particle is injected to the deflection element perpendicularly, the particle begins to be bent before the real edge of the deflection element because of the fringing field of the bending magnet (Fig 5-6). The condition of the equilibrium orbit in the region I in Fig. 5-6 is expressed as

$$\frac{p_0}{\rho(s)} = qB_y(s) \qquad \left(0 < s < \frac{b}{2}\right) \tag{5-34}$$

where $B_y(s)$ is the vertical component of the bending magnetic field ($B_y(s) = B_0 s/b$, $B_y(b) = B_0 = 2p_0/q\rho_0$) and s is the approximate length of the orbit from the starting point of the bending. Then the bending radius becomes

$$\frac{1}{\rho(s)} = \frac{2}{\rho_0}\frac{s}{b}. \qquad \left(0 < s < \frac{b}{2}\right) \tag{5-35}$$

Therefore, the angle to the edge of the deflection element at the position s becomes

$$\psi(s) = \int_0^s \frac{1}{\rho(\tau)} d\tau = \frac{s^2}{\rho_0 b} \qquad \left(0 < s < \frac{b}{2}\right) \tag{5-36}$$

By the same way, the equilibrium orbit condition in the region II in Fig. 5-6 is expressed as

$$\frac{p_0}{\rho(s)} = qB_y(s) - p_0\gamma_0^2 \qquad \left(\frac{b}{2} < s < b\right). \tag{5-37}$$

The bending radius and the angle to the edge of the deflector in the region II in Fig. 5-6 are expressed as

$$\frac{1}{\rho(s)} = \frac{2}{\rho_0}\frac{s - b/2}{b} \qquad \left(\frac{b}{2} < s < b\right) \tag{5-38}$$

$$\psi(s) = \frac{b}{4\rho_0} + \int_{\frac{b}{2}}^{s} \frac{1}{\rho(\tau)} d\tau = \frac{s^2}{\rho_0 b} - \frac{s}{\rho_0} + \frac{b}{2\rho_0} \qquad \left(\frac{b}{2} < s < b\right) \tag{5-39}$$

When the dipole magnet has the linear fringing field, the magnetic field has the longitudinal component in the fringing region [5-3]. The strength of the longitudinal component of the magnetic field is expressed by

$$B_s(y) = \frac{B_0}{b} y \tag{5-40}$$

where B_0 denotes the strength of the vertical component in the gap of the bending magnet. When the charged particle passes through the linear fringing region, it receives a vertical force depending on the angle $\psi(s)$ from the longitudinal component of the magnetic field [5-3]. The equation of the vertical motion is written by

$$\frac{d^2y}{ds^2} = \frac{qB_s(y)\sin\psi(s)}{p_0} \tag{5-41}$$

Integrating this equation in the fringing field region, the following relation is obtained

$$\left.\frac{dy}{ds}\right|_b - \left.\frac{dy}{ds}\right|_0 \approx \frac{5b}{12\rho_0^2} \cdot y \tag{5-42}$$

From Eq. (5-39), one finds the horizontal bending angle is the same as that of the sharp edge. Therefore in the fringing field region, only the vertical motion is corrected, in the first order. By a thin lens approximation, the fringing field effect can be expressed by the transfer matrix

$$M = \begin{pmatrix} 1 & 0 & 0 & 0 & 0 & 0 \\ 0 & 1 & 0 & 0 & 0 & 0 \\ 0 & 0 & 1 & 0 & 0 & 0 \\ 0 & 0 & \frac{5b}{12\rho_0^2} & 1 & 0 & 0 \\ 0 & 0 & 0 & 0 & 1 & 0 \\ 0 & 0 & 0 & 0 & 0 & 1 \end{pmatrix} \tag{5-43}$$

When this effect is taken into account, the betatron tune value falls a little and the balance of the horizontal and the vertical betatron motion is broken at the operating point k_1, k_2=0. For example, at the operating point k_1, k_2=-0.21, the betatron tune becomes (2.009, 2.017) and the beta functions becomes as shown in Fig 5-7.

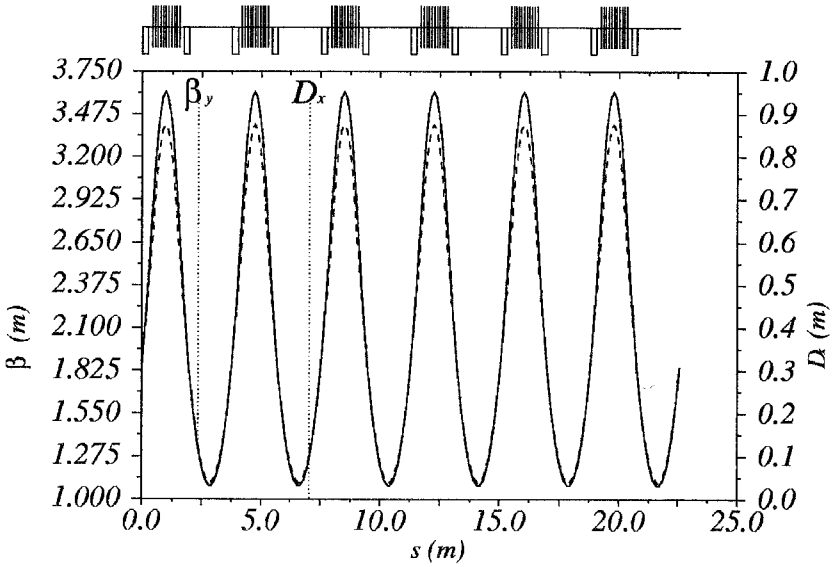

Fig. 5-7 Beta-functions at the operating point (2.009, 2.017)

5.7 Effect to the beam cooling

5.7.1 Maintenance condition

From the consideration in section 4.3.4, it is found the first maintenance condition ($\gamma < \gamma_t$) is satisfied in any type of dispersion-free rings. On the other hand, the second maintenance condition $N > 2\sqrt{2}\nu_T$ has not been satisfied unless the storage ring which has enough large bending radius and super period is provided. Especially, when the cylindrical dispersion-free deflector has been used, it has been impossible to satisfy the second maintenance condition in the lattice structure of S-LSR. As shown in previous section, when the semi-hyperbolic dispersion-free deflector is used, it is possible to satisfy the second maintenance condition in the lattice structure of S-LSR safely. Then, all obstacles to reach the 3D crystal beam at S-LSR might be removed.

5.7.2 3D laser cooling by a coupling rf cavity

The problem of the maintenance condition has been resolved. Thus, a 3D beam crystallization might be achieved in S-LSR, if an enough strong 3D cooling force is provided. Since there is no dispersion in the ring, a 3D laser cooling method using the coupling induced by a normal rf cavity through the dispersion is impossible. It has been shown that a coupling rf cavity can generate the direct coupling between the longitudinal motion and the horizontal motion without dispersion [5-5]. The coupling rf cavity scheme greatly succeeded in the lattice of TARN II [5-4], however, this scheme is not necessarily successful in the lattice of S-LSR. In the case of TARN II, in addition to the coupling effect of the coupling cavity, the coupling effect at the bunching cavity induced by the dispersion also has been effective. On the other hand, in the case of S-LSR, the effect of the bunching cavity cannot be expected, because there is small dispersion or no dispersion. Only the effect of the coupling cavity is the reliance at the first stage of the laser cooling. However, it is possible to obtain an enough coupling effect by a properly designed coupling cavity with realistic parameters [5-4]. We consider the case that the coupling cavity is introduced in addition to the bunching cavity which was described in section 4.3.4. The vector potential of the TM_{210} mode of the coupling rf cavity is given by the formula [5-5]

$$\vec{A} = \left[0,\quad 0,\quad \frac{V_c}{\omega_c}\sin\left(\frac{\pi x}{a}\right)\cos\left(\frac{\pi y}{2b}\right)\sin(\omega_c t + \phi_c)\right] \tag{5-44}$$

where a cavity which has a width of 2a and the height of 2b is supposed. When the extent of the beam is enough small compared to the width of the cavity ($x/a << 1$, $y/b << 1$), the Hamiltonian of the coupling rf cavity is given by the formula

$$\tilde{H} = \frac{\tilde{p}_x^2 + \tilde{p}_y^2}{2} - \frac{\Delta E}{\beta_0^2 E_0} + \frac{1}{2\gamma_0^2}\left(\frac{\Delta E}{\beta_0^2 E_0}\right) - \frac{\pi q V_c}{p_0 \omega_c}\frac{x}{a}\sin(\omega_c t + \phi_c)\delta_p(s - s_c) \tag{5-45}$$

ϕ_c denotes the initial phase of the coupling cavity. If the relative time $\Delta t = t - s/\beta_0 c$ is introduced, the phase of the coupling cavity can be written as

$$\sin(\omega_c t + \phi_c)\delta_p(s - s_c) = \sin(\omega_c \Delta t + \psi_c)\delta_p(s - s_c) \tag{5-46}$$

ψ_c is chosen to be zero, in order to obtain the maximum coupling effect. Namely, if the bunching rf cavity and the coupling cavity is synchronized so that the center of the bunch pass through the coupling cavity at

the phase $\psi_c = 0$, the maximum coupling effect can be obtained. For a particle near the bottom of the rf bucket ($\omega_c \Delta t << 1$), the Sin function of Hamiltonian (5-45) can be expanded. Then, a direct coupling term between longitudinal coordinate and horizontal coordinate arises without dispersion. From the canonical equation, the following relations are derived

$$\frac{\partial(\Delta E)}{\partial s} = \frac{\pi q V_c}{p_0} \frac{x}{a} \delta_p(s - s_b) \tag{5-47-a}$$

$$\frac{\partial \widetilde{p}_x}{\partial s} = \frac{\pi q V_c}{p_0} \frac{\Delta t}{a} \delta_p(s - s_b) \tag{5-47-b}$$

By using these relations, the linear transfer matrix of the coupling rf cavity is obtained.

$$M = \begin{pmatrix} 1 & 0 & 0 & 0 & 0 & 0 \\ 0 & 1 & 0 & 0 & -\frac{\pi q V_c}{\beta_0 E_0 a} & 0 \\ 0 & 0 & 1 & 0 & 0 & 0 \\ 0 & 0 & 0 & 1 & 0 & 0 \\ 0 & 0 & 0 & 0 & 1 & 0 \\ \frac{\pi q V_c}{p_0 \beta_0 E_0 a} & 0 & 0 & 0 & 0 & 1 \end{pmatrix} \tag{5-48}$$

The lattice parameter of the ring can be obtained from this matrix. However, this transfer matrix is not symplectic. Therefore this matrix is not suitable for multi-turn particle tracking [1-17]. For the multi-turn particle tracking, different type of approximation is needed in the derivation of the transfer matrix.

5.8 Realization of the electric field

The cross section view of the electrostatic deflector of S-LSR is shown in Fig. 5-10. The intermediate electrodes of the electrostatic deflector are introduced in order to maintain the field strength at the center of the aperture. But, we have found these intermediate electrodes create a new possibility which realizes various

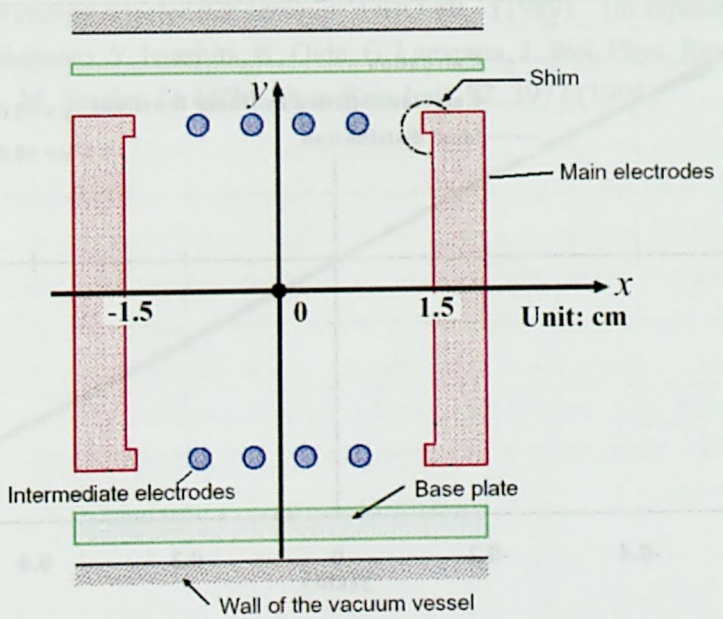

Fig. 5-10. Coordinate system in the electrostatic deflector.

structures of bending electric field in the electrostatic deflector. The voltage applied to the intermediate electrodes strongly dominates the distribution of the electric field distribution in the electrostatic deflector. From the result of the field calculation code POISSON, it is found that the both of the ideal field distribution of the cylindrical electrostatic deflector and semi-hyperbolic electrostatic deflector can be generated near the reference orbit. From the electrostatic potential of the semi-hyperbolic electrostatic deflector (Eq. (5-18)), ideal field distribution near the reference orbit are obtained as

$$E_x(x) \approx \frac{V_0}{\rho_0} \qquad E_y(y) \approx -\frac{V_0}{\rho_0^2} \cdot y \tag{5-49}$$

The field distribution along the x axis and the y axis in the electrostatic deflector (Fig. 5-10) is shown in Figs. 5-11 and 5-12.

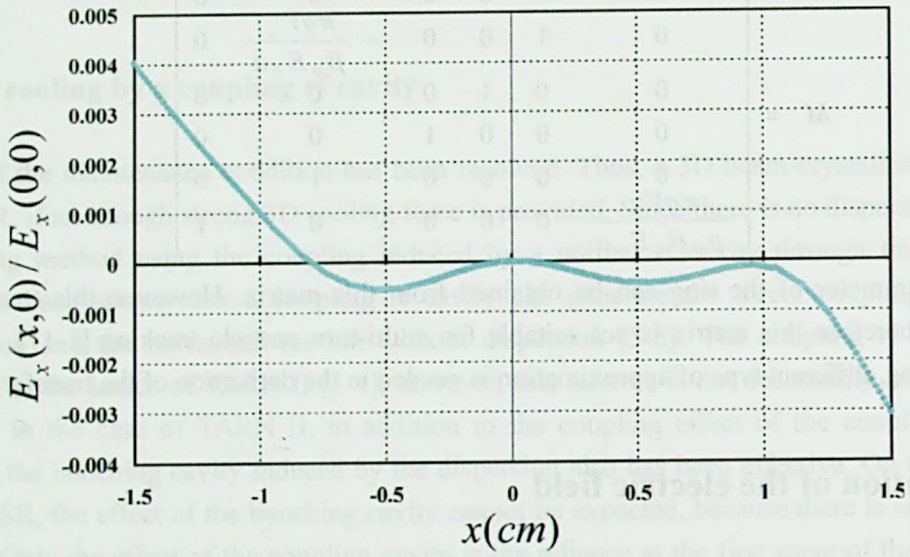

Fig. 5-11. Radial field distribution of the E_x component along the horizontal axis.

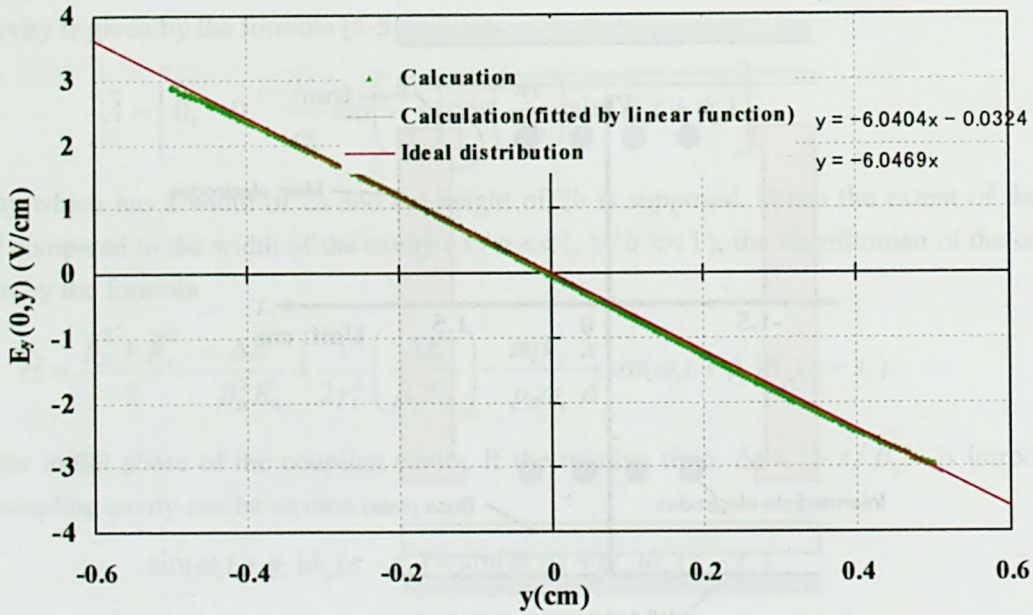

Fig. 5-12. Vertical field distribution of the E_y component along the vertical axis.

From Fig. 5-11, the deviation of the radial field distribution from the ideal distribution is almost less than $\pm 1\times10^{-3}$ in the region $-1\le x\le 1\,(cm)$. The field gradient of the E_y component on the vertical axis is obtained by fitting the field distribution within the region $-0.5\le y\le 0.5\,(cm)$ by a linear function. The obtained field gradient is -6.0404 V/cm^2. The deviation of this value from the ideal field gradient calculated from Eq. (5-49) (-6.0496 V/cm^2) is 1.5×10^{-3}. Therefore, the ideal field distribution (Eq. 5-49) are realized near the reference orbit. However, the deviation of the field distribution becomes large if it separates from the x and y axis. The dispersion free mode of S-LSR will be utilized for the purpose of experimental research of a 3D crystal beam. Thus, the circulation of a high current and large emittnce beam is not required. It might be enough that if the usable aperture is secured in the small region around the reference orbit.

5.8 Summary of this chapter

Various types of bending electric field structure have been investigated. It has been found that the radial focusing and the vertical focusing in electrostatic deflectors or dispersion-free deflectors can be controlled under conserving the total value of the focusing force (the field index). Among the various possible dispersion-free deflectors, the semi-hyperbolic deflector has optimal focusing force as the deflector for S-LSR. When the semi-hyperbolic type electric field is introduced for dispersion compensation, S-LSR can operate satisfying the second maintenance condition. Such electric field can be realized by the use of existing electrostatic deflector, only changing the voltage of the intermediate electrodes. The Hamiltonian of a coupling rf cavity has been shown. The coupling cavity can generate a direct coupling between horizontal motion and the longitudinal motion in the dispersion free storage ring.

References

[5-1] *Focusing of charged particles*, edited by A. Septier (Academic Press, New York , 1967)

[5-2] S. P. Møller, U. V. Pedersen: Proceedings of the 7th European particle accelerator conference, EPAC2000, Vienna, 2000, p794

[5-3] A. Noda, "*High energy accelerator seminar*" OHO'89 (1989) [in Japanese]

[5-4] T. Kihara, H. Okamoto, Y. Iwashita, K. Oide, G. Lamanna, J. Wei, Phys. Rev. E, **59**, 3594 (1999)

[5-5] H. Okamoto, A. M. Sessler, D. Möhl, Phys. Rev. Lett, **72**, 3977 (1994)

Conclusion

An ion storage and cooler ring S-LSR, now under construction at ICR Kyoto University, is to be utilized for the investigation about the realization of a crystal beam. The bending magnets for S-LSR were designed by using a high precision three-dimensional magnetic field simulation code TOSCA. The bending magnet was designed to have the maximum field strength 0.95 T, the bending radius 1.05 m, bending angle 60° and the gap height 70 mm. In the design of the magnet, the structure to suppress the change of the field distribution due to the saturation was applied; the radial pole end was cut with a circle, the longitudinal pole end was cut off with the shape of the Rogowsli's curve. The last two steps of the Rogowski's cut were deformed for the purpose suppressing the sextupole component. The field clamp plates were attached to the beam entrance and the exit of the magnet to suppress the tail of the fringing field. Based on the field measurements, the assignment of the magnet position was determined taking the difference of the effective lengths into account, in order to suppress the closed orbit distortion of the circulating beam. The closed orbit distortion has been suppressed less than ± 1 mm.

The use of the dispersion-free deflection element was proposed to solve the problem due to the bending shear. It was shown analytically that the shearing force is removed when the linear dispersion is canceled all around of the bending section. The dispersion-free system can compensate the difference of the revolution time of each particle of a crystal beam all around the ring. This system might be able to stabilize the crystal beam by the conventional laser cooling force. In order to obtain an enough strong three-dimensional cooling force by a normal rf cavity, it is essential that the storage ring has finite dispersion. For the case of dispersion-free mode of S-LSR a coupling cavity scheme is to be used. The coupling rf cavity can generate a coupling effect between the horizontal and the longitudinal motion without dispersion. For the case of S-LSR, the dispersion-free deflector has been constructed with a combination of a flat pole bending magnet and a cylindrical electrostatic deflector. The dispersion-free operating mode is to be applied for the laser cooling experiment of a 35 keV Mg^+ beam. In this case, the required strength of the bending magnetic field and the electric field are 0.252 T and 6.67×10^4 V/m, respectively, which are well attainable range. The effective length of the electrostatic deflector was designed to be as close as possible to the value of the magnetic field, and such difference has been suppressed within 0.5 mm. The cylindrical electrostatic deflector for S-LSR has intermediate electrodes, in order to attain the needed field homogeneity under the influence of the inner wall of the vacuum vessel. The intermediate electrodes also create a new possibility of the electrostatic deflector, they can control the field structure in the electrostatic deflector by the adjustment of the potentials applied to them. The dispersion-free mode of S-LSR using the combination of the flat dipole magnetic field and a cylindrical bending electric field which has radial position dependence as $E_x(x) \propto (\rho_0 + x)^{-1}$, extremely enhances the betatron tune of the vertical direction, and dose not satisfy the second maintenance condition of crystal beams. When a radially uniform electric field is introduced, the vertical betatron tune of S-LSR is reduced. A semi-hyperbolic electrostatic deflector can realize such bending electric field theoretically, and then S-LSR becomes to have operating points satisfying the second maintenance condition. The electrostatic deflector for S-LSR can realize this radially uniform electric field near the reference orbit by adjusting the voltage of the intermediate electrodes, it is considered to contribute to the creation of a stable three-dimensional crystal beam.

Acknowledgements

The work presented here is supported by all members of S-LSR project. I am grateful to all the members of S-LSR project both in ICR, Kyoto University and National Institute of Radiological Sciences.

Firstly, I would like to express my gratitude to my supervisor Professor. A. Noda, about fruitful suggestions of the dispersion-free system and the design and performance assessment of dispersion-free deflector.

My thanks are also to fruitful discussions with Associate Professor Y. Iwashita on the requirement for the design of the bending magnets and electrostatic deflector for S-LSR.

I am grateful to Assistant Professor T. Shirai for his assistance for the numerical calculations of lattice parameters of S-LSR.

I am grateful to Associate Professor H. Okamoto of Hiroshima University for the construction of Hamiltonian formalism of the dispersion-free deflector and the instruction of how to write a paper.

I would like to thank Dr. K. Noda for his support and suggestions throughout all of this work.

I am grateful to Dr. M. Grieser for the suggestion of the introduction of intermediate electrodes for the electrostatic deflector.

I would like to present my thanks to Dr. A. M. Sessler for many fruitful discussions.

I also would like to present my thanks to Dr. J. Wei for his useful theoretical discussions about crystal beams.

I am grateful to Technical Staff, H. Tongu and Dr T. Takeuchi for his assistance for the field measurement of the bending magnet, alignment of the magnets, design of the vacuum chamber, the supply of figures used in this thesis. I am grateful to Mr. H. Fadil for his assistance for the numerical calculations and the field measurement of the bending magnet. I am also grateful to Mr. Y. Yuri of Hiroshima University for his remark about the intensity limitation of the 3D crystal beam in a conventional storage ring. I am grateful to Mr. M. Tanabe for his assistance for the electrostatic field simulation of the dispersion-free deflector. I am grateful to Mr. H. Souda for his assistance for the calculation of the closed orbit distortion of S-LSR.

Last but not least, I would like thank to the members of S-LSR project of NIRS; Dr. S. Shibuya, Dr. H. Ogawa, Mr. T. Fujimoto.

Appendix Beam focusing element without chromatic aberration

A.1 Introduction

A quadrupole magnet or electrostatic quadrupole is often used in beam transport line. Such focusing elements inevitably cause a chromatic aberration. For example, the focusing strength of a quadrupole magnet depends on the particle energy, it is characterized by the magnetic rigidity of the focused particle; $1/f = qB_1L/\chi_B$ where f is approximated focal length, B_1 is field gradient of the quadrupole magnet, L is the length of the magnet, χ_B is magnetic rigidity ($\chi_B = p/q$), q is charge state of the focused particle. For the electrostatic quadrupole, a similar relation exists; $1/f = qV_1L/\chi_E$ where V_1 is field gradient of the electrostatic quadrupole, L is the length of the element, χ_E is electrostatic rigidity ($\chi_E = pv/q = q\chi_B^2/m$). If such chromatic aberrations can be eliminated, the precision of the mass analysis is thought to be greatly improved. From above formalisms, one finds that the response to the focusing strength differs for the same momentum deviation, because of the difference form of the field rigidity. Thus, by combining such elements, it is thought to be possible to suppress the influence of the chromatic aberration. As shown in previous chapters, in the case of beam bending, it is possible to eliminate the linear dispersion by combining the electrostatic deflector and bending magnet. On the analogy of the dispersion-less bend, we investigate the beam dynamics in the focusing element using quadrupole magnetic field and quadrupole electric field simultaneously.

A.2 Hamiltonian formalism

A Hamiltonian governing the motion of a charged particle around a focusing element where not only a quadrupole magnetic field but also a quadrupole electric field is present is derived. Choosing the path length of a design particle s as the independent variable, the relativistic Hamiltonian is given by the following form [A-1] [A-2],

$$H = -\sqrt{\left(\frac{p_t + q\phi}{c}\right)^2 - m^2c^2 - p_x^2 - p_y^2} - qA_s, \tag{A-1}$$

where m and q are the rest mass and charge state of the particle, c is the speed of light, ϕ is the scalar potential of the electrostatic quadrupole, p_t is the canonical variable conjugate to time t, x, y, p_x, p_y are horizontal and vertical coordinate and momentum, respectively, and we have assumed that the vector potential $\mathbf{A}$ only has the longitudinal component, i.e. $\mathbf{A} = (0, 0, A_s)$. The design particle passes through in the center of the quadrupoles and its momentum is p_0. p_0 is constant, because there are no electric and magnetic fields on the orbit of the design particle. In this appendix, Hamiltonian is expanded by the different method to the previous chapters, for the purpose showing the justice of the expanded formula.

The relative energy error is represented by the deviation from the energy of the design particle $E_0 = \sqrt{c^2 p_0^2 + m^2 c^4}$,

$$\frac{\Delta E}{p_0 c} = \frac{E}{p_0 c} - \frac{1}{\beta_0}. \tag{A-2}$$

where β_0 is normalized velocity of the design particle; $1/\beta_0 = E_0/p_0c$ and E is energy of the particle; $E = \sqrt{c^2p^2 + m^2c^4} + q\phi = -p_t$. The Hamiltonian Eq. (A-1) is normalized by the design momentum p_0, then, the transverse momentum is scaled dimensionless; $\tilde{p}_{x(y)} = p_{x(y)}/p_0$ and normalized Hamiltonian becomes to

$$\tilde{H} = -\sqrt{\left(\frac{E-q\phi}{p_0c}\right)^2 - \frac{1}{\beta_0^2\gamma_0^2} - \tilde{p}_x^2 - \tilde{p}_y^2} - \frac{qA_s}{p_0}, \tag{A-3}$$

Inserting Eq. (A-2) into the Hamiltonian (A-3), it becomes

$$\begin{aligned}\tilde{H} &= -\sqrt{\left(\frac{\Delta E - q\phi}{p_0c} + \frac{1}{\beta_0}\right)^2 - \frac{1}{\beta_0^2\gamma_0^2} - \tilde{p}_x^2 - \tilde{p}_y^2} - \frac{qA_s}{p_0} \\ &= -\sqrt{1 + \frac{2}{\beta_0}\left(\frac{\Delta E - q\phi}{p_0c}\right) + \left(\frac{\Delta E - q\phi}{p_0c}\right)^2 - \tilde{p}_x^2 - \tilde{p}_y^2} - \frac{qA_s}{p_0}\end{aligned} \tag{A-4}$$

The scalar potential of electrostatic quadrupole can be expressed as $\phi = V_1(x^2 - y^2)/2$, where V_1 is the gradient of the electrostatic quadrupole lens, $V_1 = V_1$ in the focusing element and $V_1 = 0$ in other region. The vector potential of a quadrupole magnet is given by $\vec{A} = (0,0,A_s)$ with $A_s = B_1(x^2 - y^2)/2$, where B_1 is the gradient of the quadrupole magnet, $B_1 = B_1$ in the focusing element and $B_1 = 0$ in other region. If the extent of the transverse motion of the particle is small, Eq. (A-4) can be expanded. If the square root is expanded and left only lower-order terms up to third order, Hamiltonian (A-4) becomes

$$\begin{aligned}\tilde{H} = &-\frac{\Delta E}{\beta_0^2E_0} + \frac{1}{2\gamma_0^2}\left(\frac{\Delta E}{\beta_0^2E_0}\right)^2 - \frac{1}{2\gamma_0^2}\left(\frac{\Delta E}{\beta_0^2E_0}\right)^3 + \frac{\tilde{p}_x^2 + \tilde{p}_y^2}{2} - \frac{\Delta E}{\beta_0^2E_0}\frac{\tilde{p}_x^2 + \tilde{p}_y^2}{2} \\ &+ \frac{qV_1}{2\beta_0^2E_0}(x^2 - y^2) - \frac{1}{2\gamma_0^2}\frac{\Delta E}{\beta_0^2E_0}\frac{qV_1}{\beta_0^2E_0}(x^2 - y^2) - \frac{qB_1}{2p_0}(x^2 - y^2),\end{aligned} \tag{A-5}$$

where the constant term is neglected. From Hamiltonian (A-5), it is found that the energy deviation ΔE is constant of motion. Thus, the transverse equations of motion are derived from Hamiltonian

$$\frac{d^2x}{ds^2} \approx -\left\{\left(\frac{qV_1}{\beta_0^2E_0} - \frac{qB_1}{p_0}\right) - \left[\left(1 + \frac{1}{\gamma_0^2}\right)\frac{qV_1}{\beta_0^2E_0} - \frac{qB_1}{p_0}\right]\frac{\Delta E}{\beta_0^2E_0}\right\}x \tag{A-6a}$$

$$\frac{d^2y}{ds^2} \approx \left\{\left(\frac{qV_1}{\beta_0^2E_0} - \frac{qB_1}{p_0}\right) - \left[\left(1 + \frac{1}{\gamma_0^2}\right)\frac{qV_1}{\beta_0^2E_0} - \frac{qB_1}{p_0}\right]\frac{\Delta E}{\beta_0^2E_0}\right\}y \tag{A-6b}$$

The second term of the each equation represents the chromatic aberration. From eq. (A-6), one finds that the first-order chromatic aberration is vanished under leaving the effect of focusing, if the relation

$$\left(1 + \frac{1}{\gamma_0^2}\right)V_1 = B_1v_0 \tag{A-7}$$

is satisfied. This relation completely coincide with the condition of dispersion-less bend using electric and magnetic field simultaneously.

A.3 Chromatic aberration-free optical system

As shown in ref. [4-16], it is possible to eliminate the dispersion at the final focal point by an electrostatic deflector and a bending magnet set at individual positions. However, it is impossible to eliminate the dispersion all around of the orbit. In order to eliminate it all around of the orbit, the use of bending electric field and bending magnetic field at the same position is essential (see chapter4). On the analogy of above fact, it is thought to be possible to eliminate the chromatic aberration at the final focal point by a quadrupole doublet constructed with a quadrupole magnet and an electrostatic quadrupole (Fig. A-1).

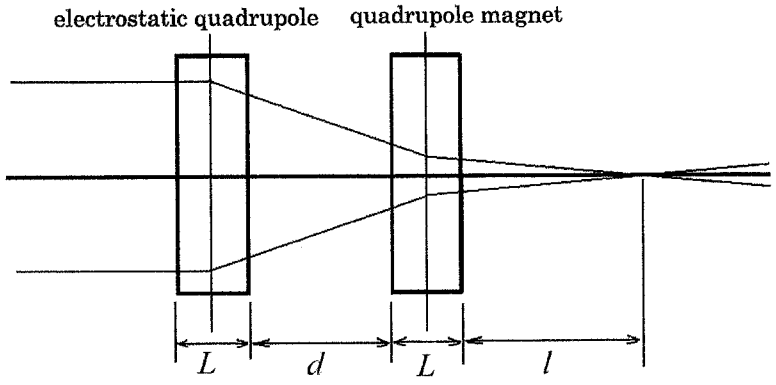

Fig. A-1 Arrangement of the elements (horizontal direction)

In thin lens approximation; $k_1 L << 1, k_2 L << 1$, the transfer matrix is given by the following forms. Here, $k_1 = qV_1 / \beta^2 E$, $k_2 = qB_1 / p$, and L represents the length of each element.

$$\begin{pmatrix} (x|x) & (x|a) \\ (a|x) & (a|a) \end{pmatrix} = \begin{pmatrix} 1 & l \\ 0 & 1 \end{pmatrix} \begin{pmatrix} 1 & L \\ k_1 L & 1 \end{pmatrix} \begin{pmatrix} 1 & d \\ 0 & 1 \end{pmatrix} \begin{pmatrix} 1 & L \\ -k_2 L & 0 \end{pmatrix} \tag{A-8a}$$

$$\begin{pmatrix} (y|y) & (y|a) \\ (a|y) & (a|a) \end{pmatrix} = \begin{pmatrix} 1 & l \\ 0 & 1 \end{pmatrix} \begin{pmatrix} 1 & L \\ -k_1 L & 1 \end{pmatrix} \begin{pmatrix} 1 & d \\ 0 & 1 \end{pmatrix} \begin{pmatrix} 1 & L \\ k_2 L & 0 \end{pmatrix} \tag{A-8b}$$

In order to focus the parallel beam at the same focal point horizontally and vertically, the condition $k_1 = k_2 = k$ should be satisfied. Then, the focal length f is indicated by $1/f = k^2 dL^2$. For a small kinetic energy deviation $E \rightarrow E(1+\delta)$, the condition that the focal length in the horizontal direction to be invariable is described as

$$\left(1 + \frac{1}{\gamma_0^2}\right) = \frac{1+kdL}{1-kdL}. \tag{A-9}$$

The values of k, d and L which satisfy Eq. (A-9) exist. However, in this case, the vertical focal length cannot be invariable, at the same time. Namely, it is impossible to eliminate the chromatic aberration in both directions. In the case of quadrupole triplet, it is difficult to eliminate the chromatic aberration in both directions. Therefore, it is essential to use the quadrupole electric field and quadrupole magnetic field in the same region, in order to eliminate the chromatic aberration in both directions simultaneously.

On the other hand, in the case of optical lenses, there is no directivity such as beam focusing element. Thus, in order to eliminate the chromatic aberration, it is sufficient only to satisfy Eq. (A-9). The size of chromatic aberration of the optical lens is depends on refractive index of the material. Therefore, magnetic rigidity and electrostatic rigidity correspond to the refractive index of the material of the optical lens.

References

[A-1]K. Oide: *Proc. First workshop.* JLC-FFIR92 12/16-18, 1992, KEK Proceedings 93-6, p195. http://www-jlc.kek.jp/subg/ir/lib/DOC/japanese/Lecture.beam.dynamics.ps

[A-2] F. C. Iselin, The Mad program Physical method manual, CERN/SL/92

[A-3] W. Z. Liu, and F. D. Becchetti, Rev. Sci. Instrum. **60** (7), 1989

[A-4] U. A. Staffan TAPPER and Bjarne Roger NIELSEN, Nucl. Instrum. Methods. B **44**, 219 (1989)